A Device for Performing Sonoporation on Adherent Cell Cultures

by

Jonathan Lawrence Kivinen

A thesis presented to Lakehead University in partial fulfillment of the requirements for the degree of

Master of Science in
Electrical and Computer Engineering

Thunder Bay, Ontario, Canada

September 19, 2014

Abstract

Sonoporation is a method for inducing a transient increase in the permeability of cell membranes to otherwise impermeable compounds using ultrasound. This technique has therapeutic potential as it allows for localized delivery of therapeutic agents in a non-invasive and non-cytotoxic manner. The discovery and testing of potential therapeutic agents that can be delivered using this technique requires performing studies on cell cultures *in vitro*. This thesis presents a prototype sonoporation device which aims to reduce the time and expertise required to perform sonoporation on adherent monolayer cell cultures.

First, a prototype sonoporation device was designed and constructed. The device consisted of an array of six ultrasound transducers affixed below a cell culture stage. The six transducers were each constructed and electrically matched to 50 Ω at an operating frequency of 1 MHz. The acoustic near-field of each transducer was characterized using hydrophone scanning and the distance from the transducer at which the plane perpendicular to the beam path was most homogeneous was determined. The mean(±s.d.) treatment distance was 15.9(±0.67) mm and the mean -3 dB width was 1.97(±0.22) mm. The electrical power required to produce 0.7 MPa on this plane was found for each transducer. The mean(±s.d.) electrical power was 101(±12.2) W.

Next, the prototype device was experimentally validated. Sonoporation was performed on cervical carcinoma-derived SiHa cells with 70-80% confluency at media temperatures of 37°C, 39.5°C, and 42°C. Pulsed ultrasound of 1 MHz, 4.8% duty cycle, 1.6 kHz pulse repetition frequency, and 0.7 MPa peak pressure was applied to induce sonoporation. Ultrasound contrast agent was added to the cell culture media (0.33% v/v) to provide cavitation nuclei during treatment. Plasmid DNA expressing green fluorescent protein (GFP) was added to the cell culture (250 μg/10 mL) to quantify successful permeabilization. While there were no significant effects due to the temperature of the media, transfection was successfully performed using the prototype device given the positive expression of GFP in the cells 24 hours following treatment. The mean(±s.d.) transfection efficiencies of the sonoporation treatment at 37°C, 39.5°C, and 42°C were 5.4(±0.92)%, 5.8(±1.3)%, and 5.3(±1.1)% respectively ($n = 3$ for each experimental group). Negative control treatments had transfection rates of $< 1.5\%$ on average and the detected levels of apoptosis among surviving cells was $< 0.5\%$ on average for all treatment groups.

These results were in good agreement with those obtained using a different sonoporation experimental set-up on the same cell line with similar experimental parameters.

Finally, the design of high-power ultrasound driving circuitry was explored in order to create an electrical device with the ability to provide independent, concurrent, and controlled excitation of the six transducers. A class DE half-bridge amplifier topology was chosen as the output power stage of this device. A design of a class DE amplifier was simulated using `LTSpice` with both a resistive 50 Ω load and a Butterworth-Van Dyke equivalent circuit model of one of the six transducers, matched to 50 Ω at 1 MHz. The amplifier was designed to deliver 150 W to a 50 Ω resistive load at an output frequency of 1 MHz using a DC supply voltage of 96 V. The simulation of the amplifier using the transducer equivalent circuit yielded an output power of 134 W, a drain efficiency of 98.8%, a power-added efficiency of 89.0%, a gate power gain of 22.6 dB, and a total harmonic distortion at the output of 27.9%.

The device presented here was shown to be effective at performing sonoporation on adherent monolayer cell cultures and will reduce the time and expertise required to perform this technique in the future.

About the Author

Jon Kivinen joined the Thunder Bay Regional Research Institute as a research assistant during his undergraduate studies in the fall of 2009. His work there involved improving performance of numerical calculations for acoustic and heat transfer simulations using general-purpose graphics processing units (GPGPUs). From April 2010 to September 2011, he was a co-op student with the institute, contributing to various projects including `MatMRI`, a software package to allow researchers additional control over the Philips 3T research MRI at the Thunder Bay Regional Health Sciences Centre. Jon graduated from Lakehead University with a degree of Bachelor of Engineering in Software Engineering (Co-op) in the spring of 2012.

Acknowledgements

My friends and family, who supported me both financially and emotionally through seven years of post-secondary education. Thank you for your love and your patience.

Ben Zaporzan, Dexter Hobson, Arturo Vargas, Sandra Diaz, Tony Sinclair, Chris Abraham, Robert Jackson, Brianne Wood, and all the other wonderful people (unlisted but not forgot) that I've had the pleasure of getting to know during my involvement with the Thunder Bay Regional Research Institute.

Greg Mulzer, Joshua Choi, and Melissa Togtema, without whose hard work and expertise the sonoporation-temperature and prototype validation study could not have been present here.

Dr. David Goertz of Sunnybrook Research Institute and the University of Toronto and Dr. Krishnamoorthy Natarajan of Lakehead University for taking the time to review this work.

Members of my committee, Dr. Carlos Christoffersen and Dr. Wely Floriano of Lakehead University, for their time and support.

The Natural Science and Engineering Research Council of Canada whose CREATE and Discovery programs made this work possible.

Last, but not least, my supervisor Dr. Samuel Pichardo and co-supervisor Dr. Laura Curiel for their mentorship as well as their tireless efforts to create opportunities for students like me.

Contents

List of Figures

List of Tables

List of Symbols

a Radius of disc source

B Susceptance

c Speed of sound

C Capacitance

C_0 Static capacitance (Butterworth-Van Dyke model)

C_a DC blocking capacitance of transformed RLC network

C_m MOSFET (switch) shunt capacitance

C_o Output capacitance of MOSFET

C_{OSS} Combination of the MOSFET gate-drain capacitance and drain-source capacitance

C_p Parallel capacitance

C_{RSS} MOSFET gate-drain capacitance

C_s Series capacitance

d Distance

η Amplifier efficiency

η_D Amplifier drain efficiency

f Frequency (Hz)

f_c Center frequency of RLC filter

f_o Operating frequency (Hz)

$f_{p,n}$ Anti-resonant frequency n (Butterworth-Van Dyke model)

$f_{s,n}$ Resonant frequency n (Butterworth-Van Dyke model)

G Conductance

Γ Reflection coefficient

i AC current

I DC current

$I_{DM(max)}$ Maximum (peak) drain current

I_m Peak output current

$\bar{\mathcal{I}}_{bg}$ Mean image intensity of background

$\bar{\mathcal{I}}_{obj}$ Mean image intensity inside an object

$\mathcal{I}_{sppa}$ Spatial-peak pulse-averaged acoustic intensity

$\mathcal{I}$ Acoustic intensity

$\mathcal{I}_{peak}$ Peak acoustic intensity

j Imaginary unit ($= \sqrt{-1}$)

k Duty cycle

L Inductance

L_a Resonant component of output inductance

L_b Non-resonant component of output inductance

M MOSFET component

$M(f)$ Hydrophone linear sensitivity

ω Angular frequency (rad/s)

Ω Ohm (unit)

ω_o Operating frequency (rad/s)

$\omega_{p,n}$ Anti-resonant angular frequency n (Butterworth-Van Dyke model)

$\omega_{s,n}$ Resonant angular frequency n (Butterworth-Van Dyke model)

P Power

p Pressure

P_D Amplifier drain power consumption

P_G Amplifier gate drive power

P_I Amplifier input (supply) power

P_o Amplifier output power

q Transformation quality factor

Q Quality factor

Q_L Loaded quality factor

R Resistance

ρ Density

R_o Output resistance

R_p Parallel resistance

R_s Series resistance

S Siemens (unit)

σ Standard deviation

t Time

v AC voltage

V Volts (unit)

$V_{DS(max)}$ Maximum (peak) drain-source voltage

V_m Peak output voltage

X Reactance

Y Admittance

z Axial distance

Z Impedance

Z_{eq} Equivalent impedance

z_{nf} Near-far field transition distance for ideal disc source

List of Abbreviations

ABS Acrylonitrile butadiene styrene

AC Alternating current

ANOVA Analysis of variance

BNC Bayonet Neill-Concelman (connector)

BvD Butterworth-Van Dyke

CA Contrast agent

CSG Constructive solid geometry

C.W. Continuous-wave

DAPI 4',6-diamidino-2-phenylindole

DC Direct current

DMEM Delbecco's modified eagle medium

FBS Fetal bovine serum

GFP Green fluorescent protein

GND Ground (common)

HIFU High-intensity focused ultrasound

HPV Human papilloma virus

HSD Honestly significant differences

MI Mechanical index

MOSFET Metal-oxide-semiconductor field effect transistor

MRI Magnetic resonanace imaging

p-p Peak-to-peak

PAE Power-added efficiency

PARP Poly (ADP-ribose) polymerase

PBS Phosphate buffered saline

pDNA Plasmid DNA

PFA Paraformaldehyde

PRF Pulse repetition frequency

RF Radio frequency

RLC Resistor-inductor-capacitor

siRNA Small interfering RNA

s.d. Standard deviation

TBRRI Thunder Bay Regional Research Institute

THD Total harmonic distortion

US Ultrasound

ZDS Zero derivative switching

ZVS Zero voltage switching

Chapter 1

Sonoporation

1.1 Introduction

Ultrasound is a mechanical wave which can easily propagate through soft tissue in the human body. At high intensities, thermal and non-thermal effects of the ultrasound mechanics become more apparent. Ultrasound waves can easily be focused to allow highly localized effects to be produced. The biological effects of focused ultrasound were described as early as [1] in 1942. In 1954, [2] developed a device which employed focused ultrasound to perform thermal ablation in brain tissue. At the time, however, there was no practical way to monitor the process. In recent decades, with the advent of magnetic resonance imaging (MRI) and MRI thermometry, real-time monitoring of non-invasive ultrasound has become possible [3–5]. Consequently, ultrasound has since gained a lot of interest as a non-invasive therapeutic tool.

Focusing ultrasound energy has many potential therapeutic applications in the body. For instance, tissue can be selectively heated using focused ultrasound in either a non-destructive manner (*e.g.* mild hyperthermia) [6–8] or a resectional manner (*e.g.* thermal ablation) [1–3, 5]. Non-invasive destruction of tumors, for example, is possible with high intensity focused ultrasound (HIFU), allowing one to destroy the tumour while potentially sparing sensitive surrounding tissue [3].

Thermal effects of ultrasound have also been used to aid in targeted drug delivery [6–8]. Thermosensitive liposomes, for example, have been used to encapsulate therapeutic agents in an biologically-inert lipid shell [9, 10]. This shell can be disrupted non-invasively using focused ultrasound by increasing the temperature of the shell beyond its gel-to-liquid phase transition temperature in the desired treatment region thereby releasing the

encapsulated therapeutic agent locally. This targeted release of the drug can potentially spare other parts of the body from the drug's effects [10].

Non-thermal effects of ultrasound, such as acoustic cavitation, have therapeutic applications as well. Ultrasound has been used to temporarily increase the permeability of biological barriers to otherwise impermeable compounds [6, 11–13]. In [13], ultrasound was used to enhance the permeability of the blood-brain barrier of rabbits in a localized and transient manner. The blood-brain barrier is impermeable to many therapeutic drugs, making the brain a difficult organ to treat [13]. With this technique, the efficacy of therapeutic drugs targeting the brain can potentially be increased, requiring less drug to be present in the bloodstream, thereby sparing other parts of the body from undesired effects. A similar phenomenon is thought to increase the permeability of cell membranes as well, a process which has been demonstrated both *in vitro* [11, 12, 14–22] and *in vivo* [6–8, 23]. Cellular uptake of large genetic molecules such as small interfering RNA (siRNA) [14, 16] and plasmid DNA (pDNA) [15, 20–22, 24, 25] has been shown to be enhanced by the presence of micron-sized stabilized gas bodies in an ultrasonic field. This ultrasound-induced permeability of cell membranes has been shown to be transient in nature, with the permeability of the cell membrane returning to normal after a short period of time [17, 19]. Delivery of genetic material into cells using ultrasound has the potential for use in cancer therapy as these kinds of materials can disrupt actors and processes responsible for cellular immortalization and proliferation [14, 21]. This process provides a non-cytotoxic alternative for large molecule delivery *in vivo* [21].

Inducing transient increases in the permeability of cell membranes for material transfer is the subject of this work. Here, a prototype device for performing large molecule delivery *in vitro* on adherent cell cultures using ultrasound is presented. *In vitro* studies are a necessary step in developing non-invasive, targeted therapies which exploit this phenomenon. This work presents a device which aims to reduce the time and expertise required to perform these types of studies.

The subsequent sections in this chapter present additional background on this phenomenon including a review of the potential physical mechanisms involved, measures of its efficacy, a review of experimental parameters and their effect on its efficacy in the literature, and a review of *in vitro* experimental set-ups used in the literature. Chapter 2 introduces the problem statement, proposes a solution, and describes the design and construction of a prototype for performing sonoporation *in vitro*; Chapter 3 details the experimental validation of the prototype; Chapter 4 explores high-power ultrasound

driving electronics to be used with the prototype; and Chapter 5 discusses future work.

1.2 Sonoporation

1.2.1 Physical Mechanisms

The process of inducing a transient increase in the permeability in biological membranes using ultrasound is referred to as "sonoporation". Ultrasound-induced membrane permeability is a phenomenon attributed to the interaction between the cavitation of gas bodies and nearby cell membranes [6,11,12]. Permeability has been shown to be enhanced by the addition of micron-sized stabilized gas bodies ("microbubbles") which lower the energy requirements for acoustic cavitation [12,15,25]. Commercially available ultrasound contrast agents (UCAs), which have historically been used to enhance contrast of blood vessels in ultrasound imaging, are commonly used as sources of cavitation nuclei for enhancing sonoporation [12, 15].

Cavitating microbubbles present a number of possible modes of interaction with nearby cell membranes which can result in pore formation [26]. At low acoustic intensities, stable cavitation (oscillation) is thought to induce shear stress on the cell membrane through the generation of rapid flow in the surrounding medium, referred to as "microstreaming" [27–29] (Fig. 1.1a). In [27], the authors captured high-speed images of oscillating microbubbles pushing and pulling on the cell membrane when in close proximity, an interaction which correlated with increased uptake of propidium iodide. At higher acoustic intensities, inertial cavitation (collapse) can occur, causing streams ("microjets") to form due to the presence of the relatively rigid cell membrane [30, 31].

These microbubble-induced stresses are thought to cause physical disruptions in the cell membrane ("pores") which can then allow impermeable compounds to passively diffuse across the cell membrane [27, 32]. There is evidence, however, that pore formation may only facilitate cellular uptake of relatively small agents and that cavitation (or pore formation) may be stimulating endocytosis for uptake of larger agents. In [32], the authors observed a significant decrease in uptake of larger dextrans (70 kDa to 500 kDa) after inhibiting endocytosis pathways, whereas smaller dextrans were still detectable. They also observed smaller dextrans having a rather homogeneous distribution within the cell whereas larger dextrans were heterogeneously distributed and encapsulated by "vesicle-like structures" consistent with endocytosis.

In addition to the delivery of agents present in the extracellular region through pas-

sive diffusion or endocytosis, "loaded" microbubbles (*i.e.,* those which have the agents attached to the microbubble shell) have also been considered a delivery mechanism by passing microbubble material (in whole or in part), along with the drug, through the cell membrane directly during disruption [33] or by radiation force [34] (Fig. 1.1c).

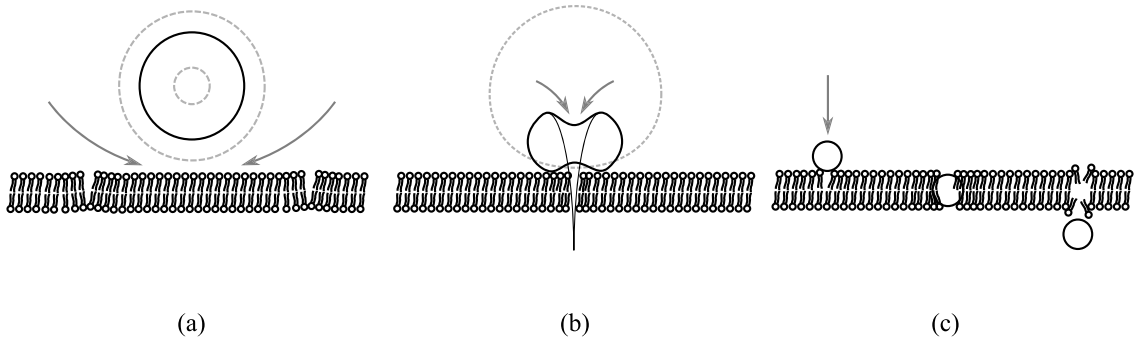

Figure 1.1: Different possible modes of interaction between microbubbles and cell membranes in an acoustic field: (a) oscillating microbubbles can cause rapid flow (microstreaming) which can potentially generate large shear forces on nearby cell membranes [27–29]; (b) asymmetric microbubble collapse at the cell membrane may result in a membrane-piecing jet to form (microjetting) [30, 31]; and (c) radiation force may cause oscillating microbubble to transit the cell membrane directly (translation) [34].

1.2.2 Sonoporation Efficacy

Sonoporation efficacy can be quantified by many measures, most notably transfection efficiency and cell viability. Transfection efficiency is quantified as the percentage of viable (surviving) cells which exhibit an increase in permeability after treatment. Cell viability is measured as the fraction of cells which do not exhibit necrosis or apoptosis remaining after treatment. These two measures are often observed as being inversely dependent [15,18,25], hence, they may be combined to provide an overall rating of efficacy referred to as the "therapeutic ratio", defined as the ratio between the number of transfected cells and the number of non-viable cells [18]. It is important to many studying sonoporation to find the optimum set of experimental parameters which maximize the transfection efficiency and minimize the cell death [18].

1.2.3 Parameters Affecting Sonoporation

Optimal conditions for sonoporation depend on a number of different parameters and is the subject of much study [15, 18, 22, 25]. Ultrasound excitation can be performed as

continuous wave (C.W.) or pulsed excitation, where pulsed modes are specified by duty cycle (or pulse length) and pulse repetition frequency (PRF). Sonoporation is typically performed using ultrasound frequencies ranging from a few hundred kHz to a few MHz and pressures ranging from a few hundred kPa to a few MPa. Pulsed excitation has been performed with duty cycles ranging from a few percent to a couple tens of percent and PRFs of a few tens of Hz to a few kHz. A summary of acoustic conditions in a selection of *in vitro* studies is available in Table 1.1.

In examining the effect of acoustic parameters on permeability and cell viability, these acoustic parameters are often examined in the context of microbubble activity [11, 12, 15, 18]. It has been noted that there exists an acoustic threshold below which permeabilization and cell death do not occur, dependent on pressure, frequency and pulse repetition frequency [11, 15, 18, 35]. This threshold has been associated with inertial cavitation [11, 35] as the pressure required to surpass this threshold has been seen to increase with frequency [11, 35]. In [15], low pressure amplitudes were unable to induce permeabilization, even at long pulse durations. Beyond this threshold, microbubble disruption (*i.e.,* inertial cavitation) is believed to occur within only a few cycles [12, 15], hence, longer pulse durations and insonation times are considered to contribute less of an effect to permeabilization [15, 16]. In [18], nearly all (99%) of the microbubbles were disrupted when exceeding this threshold. However, as the authors point out, microbubble disruption may not be a sufficient indicator of successful permeabilization [18]. Permeabilization due to microbubble concentration has been seen to plateau at low concentrations (*e.g.* 2%) [11, 15, 16]. Increasing microbubble concentration further has been seen to only lower cell viability [15, 16, 25].

Permeabilization and cell death have been noted to be inter-dependent [11, 15, 18, 25]. That is, parameters which increase permeabilization tend to increase cell death as well. For instance, cell permeabilization tends to increase with decreasing acoustic frequency, as does the rate of cell death [18]. Longer pulse durations tend to increase cell permeability but also decrease viability [18]. Increasing acoustic pressure has also been observed to have a negative impact on cell viability while increasing permeability [11, 15, 18]. In [18], the authors recommended that, for applications where cell survival is important, sonoporation should be performed at high frequency, low pressure, and low duty cycle; and in applications where viability is not important, permeabilization may be improved by using low frequency, high pressure, and high duty cycle.

In vitro sonoporation can also be affected by experimental set-up. For example, stand-

Ref.	p_- (MPa)	Center Freq. (MHz)	Duty (%)	PRF (kHz)	Insonation time (s)	Notes
[11]	0.05-0.8	2.25	C.W.	-	n.s.	
[35]	0.025∼0.4	1.0 - 7.15	C.W.	-	60	
[16]	0 - 4 (W cm^{-2})	1.706	C.W.	-	15 - 120	Reported “acoustic power”
[36]	0.2 - 0.6	2.25	C.W.	-	60	
[29]	0.05 - 0.3	1.0	C.W.	-	20	
	0.1	1.0	C.W.	-	0 - 60	
[14]	0 - 11 (W)	1.653	C.W.	-	10	Reported “acoustic power”
	0 - 11 (W)	1.653	10	0.002	100	Reported “acoustic power”
[12]	0.23∼0.9	3.5	2.2	1.08 - 14.8	4 - 960	Doppler mode
	0.39∼1.9	3.5	0.0032	3.4	60	2D imaging mode
[37]	0.25 - 3 (W cm^{-2})	1.0	20	0.1	0-60	Reported $\mathcal{I}_{sppa}$
[24]	0.402	1.15	20	0.1	10	
	0.570	2.25	20	0.1	10	
[15]	0.13 - 0.5	1.0	10 - 80 (cycles)	1.0	40	Examined pulse length
	0.5	1.0	40 (cycles)	0.5 - 2.5	40	Fixed pulse length
[18]	0 - 0.57	0.5	9.6	3.0	120	
	0 - 2.32	2.0	9.6	3.0	120	
	0 - 3.5	5.0	9.6	3.0	120	
	0.125 - 0.57	0.5	1.2 - 9.6	3.0	120	
	0.125 - 0.57	0.5	16 (cycles)	0.01 - 3	120	Fixed pulse length
	0.125 - 0.57	0.5	9.6	3	0 - 120	
[25]	0.13 - 0.48	1.0	25	0.1	180 (∼35/cell)	Transducer translated across cell culture during exposure
[20]	0 - 1	0.930	4.8	1.5	30	
[21]	1.0	0.930	4.8	1.5	30	
[22]	1.0	1.0	4.8	1.6	30	
[19]	0.88 (p-p)	1.5	20	1.0	30	Reported peak-to-peak pressure (p-p)
[38]	0.88 (p-p)	1.5	20	1.0	30	Reported peak-to-peak pressure (p-p)
[39]	0.62 - 1.25 (p-p)	1.5	20	1.0	30	Reported peak-to-peak pressure (p-p)
[40]	0.88 (p-p)	1.5	20	1.0	30	Reported peak-to-peak pressure (p-p)
[41]	1.2 MI	1.3	n.s.	n.s.	30-60	Reported mechanical index (MI)

n.s. - not specified

Table 1.1: A summary of a selection of *in vitro* sonoporation experiments and their acoustic parameters.

ing wave formation has been shown to have a large effect on sonoporation efficacy [16]. The presence of standing waves in sonoporation studies can be problematic for reporting the acoustic conditions under which sonoporation was performed as it is difficult to know for certain what the conditions were [16]. In [16], the effects of standing wave formation on sonoporation was explored *in vitro* and the authors found that the presence of standing waves significantly increased transfection efficiency and decreased cell viability.

Other experimental parameters have been seen to have an effect on sonoporation efficacy as well. For instance, treating cells in suspension or in monolayer may have different effects. In [16], C166 endothelial cells treated in monolayer experienced higher viability than those treated in suspension despite experiencing similar levels of permeability. While some cells can be grown and survive in suspension, other cell types are inherently adherent. It is likely the case that the viability of adherent cells may suffer during detachment due to cellular processes such as anoikis.

Sonoporation efficacy tends to also be dependent on cell line [22, 42] and cellular phase [22,43]. In [22], three different HPV-positive, cervical cancer-derived cell lines were examined and it was observed that the average permeabilization of CaSki cells was significantly lower than that of HeLa and SiHa cells under the same experimental conditions.

Cell membrane fluidity has also been seen to contribute to transfection efficiency. In [44], a 15-fold increase in transfection efficiency of prostate cancer PC-3 cells was observed at cell temperatures of 42°C over temperatures of 37°C, an increase the authors attributed to increased cell membrane fluidity due to thermal treatment. The increase the authors observed was similar in effect to that of a lidocaine treatment, a substance known to increase cell membrane fluidity.

1.2.4 Experimental Set-ups

The exposure of a cell culture to an acoustic field necessarily requires a cell culture and an ultrasound source. In the literature, sonoporation has been performed using a number of different experimental set-ups (Fig. 1.2, Table 1.2) and a number of different experimental conditions (Table 1.1). The variety in physical conditions across the literature makes comparing results from different studies problematic [15, 16, 18, 45].

Ultrasound generation is often performed using general laboratory equipment [15, 17, 18,20–22]. An electrical signal is generated by an arbitrary waveform generator, amplified by a radio-frequency (RF) amplifier, and converted to a mechanical wave using an ultrasound transducer. Commercial ultrasound systems have been used in some instances to

produce the ultrasound [12, 14, 16] but these systems often offer less control over acoustic parameters [15].

There are commercially available sonoporation systems as well which aim to make performing sonoporation studies easier. For example, the Sonidel SP100 (Sonidel Ltd., Dublin, Ireland) is a sonoporator which is commercially available. This device consists of a free ultrasound transducer, driving electronics, and easy-to-use interface. While, this device been used in a number of sonoporation studies, it often appears to be used with "modification" [25, 46]. The acoustic conditions at the cells is not necessarily ensured in its stock configuration due to the use of a hand-held ultrasound transducer. That is, this sonoporator requires an additional experimental apparatus to ensure consistent ultrasound exposure between experiments.

There are several ways in which target cell cultures can be situated in the acoustic field. In some instances, well plates or Petri dishes were used [14, 16, 37, 41, 46]. Using well plates or Petri dishes placed at the surface of the ultrasound bath is problematic since acoustic reflections at the water-air interface make it difficult to know the physical conditions under which the cells are being treated (Fig. 1.2c) [15, 16]. In [14], the authors go through great effort to avoid reflections and standing wave formation with well plates by using a complicated set-up consisting of a second water tank placed above the well plate, in the acoustic far-field (Fig. 1.2d).

The Opticell cell culture system (Nunc Thermo Scientific) has become a popular exposure chamber for performing sonoporation on adherent monolayer cell cultures [15, 19–22, 25, 38–40]. An Opticell cell culture chamber consists of two thin gas-permeable membranes (one of which is treated to allow cell cultures to adhere) and two rubber ports which allow for material to be added and removed via needle and syringe. In [15], the thin membranes of the Opticell presented $<1\%$ loss in acoustic intensity, demonstrating that the Opticell is suitable for sonoporation applications. Opticell chambers are fully submersible, eliminating the highly reflective liquid-air interface created when using alternatives such as well-plates at the bath's surface. Additionally, fully submersible cell culture chambers allow for an acoustic absorber to be placed in the acoustic far-field, mitigating reflection and standing wave formation further (Figs. 1.2e and 1.2f).

Cell cultures have been treated either as a suspension in cell culture media or as an adherent monolayer. Suspended cell cultures are thought to reflect *in vivo* conditions more accurately [16]. Suspended cells are often sonoporated in a test tube which may be mechanically stirred or rotated (Figs. 1.2a and 1.2b) [11, 17, 24, 35, 36, 45]. Stirring or

rotating the test tube is thought to provide the cell culture with a homogeneous ultrasound exposure [45], however, in [35], no significant improvement in transfection efficiency was observed using a rotating tube.

Adherent cell cultures in monolayer tend to receive multiple isolated sonoporation treatments across their area [19–22, 25, 39, 40]. An Opticell chamber, for example, has an area of 50 cm^2. In order to perform multiple treatments with a single transducer, a positioning system is often employed [19–22, 25, 39, 40]. For accurate reporting of the acoustic conditions at the cells, the cell culture needs to be perfectly aligned with the positioning system or the positioning system needs to be pre-configured (in the case of a computerized positioning system) to correct for misalignment.

A summary of experimental set-ups for a selection of *in vitro* sonoporation studies is available in Table 1.2.

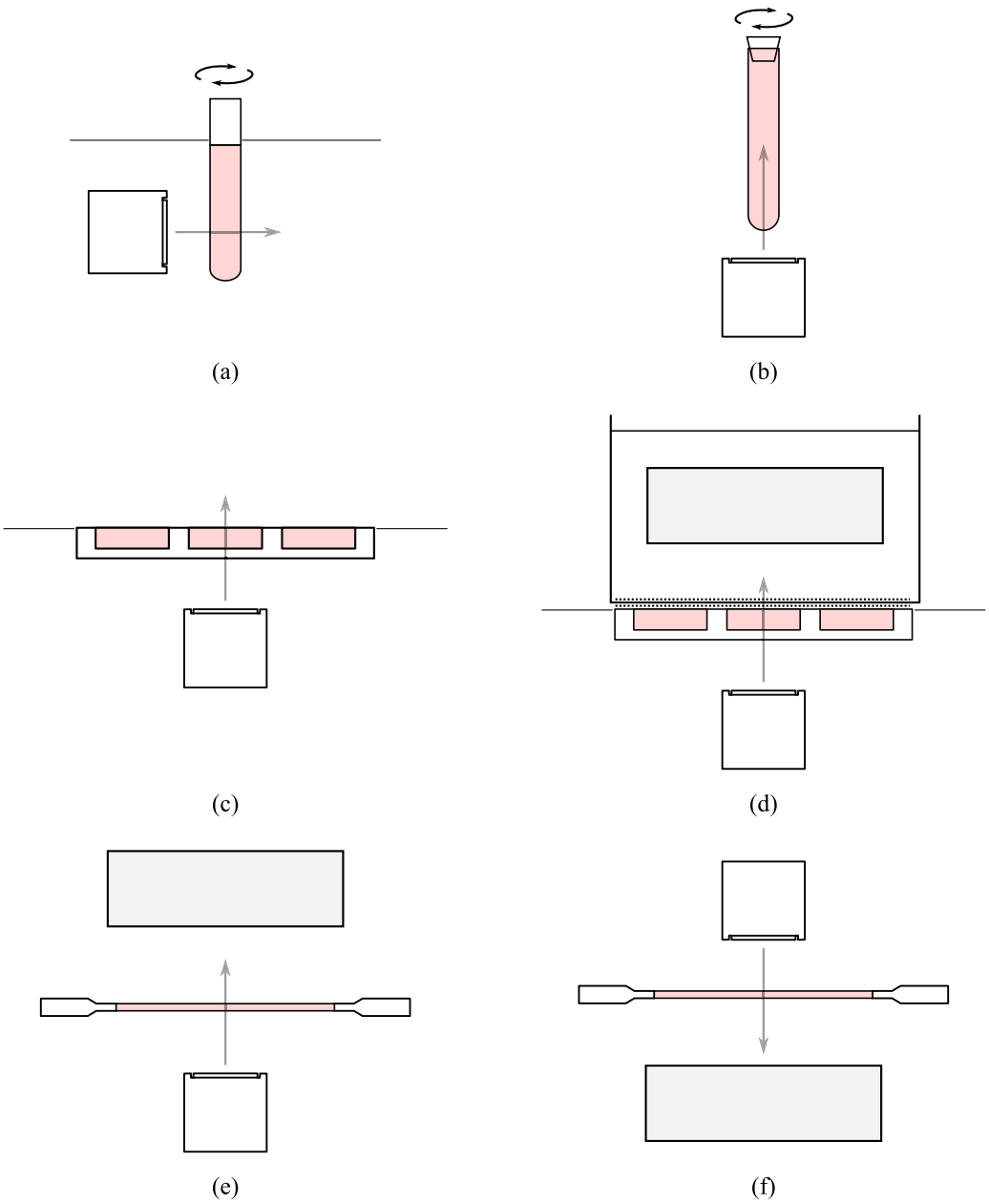

Figure 1.2: A summary of common experimental set-ups from the literature: (a) (rotating) tube (horizontal) [11, 24, 35, 36]; (b) (rotating) tube bottom-up [29]; (c) well plate [37, 41]; (d) well plate with a secondary water tank and ultrasound absorber above, coupled with thin plastic sheets (dotted) [14, 16]; (e) Opticell chamber (bottom-up) with absorber in the far-field [20–22, 25, 38]; and (f) Opticell chamber (top-down) with absorber in the far-field [19, 39, 40].

Ref.	Suspension/ Monolayer	Stirred/ Rotated	Chamber	Orientation	Positioning	Standing Wave Mitigation	US Generation
[29]	Suspension		Test tube	Bottom-up	Fixed	Rubber stopper	General
[11]	Suspension	Rotating	Test tube	Horizontal	Fixed	n.s.	n.s.
[35]	Suspension	Rotating	Test tube	Horizontal	Fixed	n.s.	n.s.
[24]	Suspension	Rotating	Test tube	Horizontal	Fixed	n.s.	n.s.
[36]	Suspension	Rotating	Test tube	Horizontal	Fixed	n.s.	n.s.
[18]	Suspension	Stirred	Custom	Horizontal	Motorized	No mitigation	General
[14]	Suspension		Well plate	Bottom-up	Manual	Absorber	US driver
[16]	Both		Well plate	Bottom-up	Manual	(Under study)	US driver
[37]	Monolayer	-	Well plate	Bottom-up	n.s.	Moving source	US machine
[41]	Monolayer	-	Well plate	Bottom-up	n.s.	No mitigation	US machine
[12]	Monolayer	-	Custom	Bottom-up	Fixed	n.s.	Imaging system
[31]	Monolayer	-	Petri dish	Bottom/Angled	Fixed	Angled	n.s.
[19]	Monolayer	-	Opticell	Top-down	n.s.	n.s.	n.s.
[39]	Monolayer	-	Opticell	Top-down	n.s.	n.s.	n.s.
[40]	Monolayer	-	Opticell	Top-down	n.s.	n.s.	n.s.
[15]	Monolayer	-	Opticell	Top-down	Fixed	Absorber	General
[25]	Monolayer	-	Opticell	Bottom-up	Manual	n.s.	Sonoporation system
[38]	Monolayer	-	Opticell	Bottom-up	n.s.	n.s.	General
[20]	Monolayer	-	Opticell	Bottom-up	Motorized	Absorber	General
[21]	Monolayer	-	Opticell	Bottom-up	Motorized	Absorber	General
[22]	Monolayer	-	Opticell	Bottom-up	Motorized	Absorber	General

n.s. - not specified

Table 1.2: A summary of a selection of sonoporation experimental set-ups.

Chapter 2

Sonoporation Platform

2.1 Design Overview

2.1.1 Previous Sonoporation System

At the Thunder Bay Regional Research Institute (TBRRI), sonoporation experiments have been performed using general-purpose laboratory equipment. The experimental set-up for these experiments used a 3-axis, computer-controlled micropositioning system (UMS2; Precision Acoustics, Dorsetshire, UK) to move a single-element focused ultrasound transducer to various positions across the area of an Opticell cell culture chamber (Fig. 2.1). Electrical generation was performed using general lab equipment including waveform generators and radio-frequency (RF) amplifiers. While this system has been used to perform sonoporation in a number of studies at the TBRRI [20–22], it has a number of drawbacks which impedes its routine use.

First, the water bath takes a considerable amount of time to set-up, treat, and tear-down due to its size. The water tank measures approximately $97 \times 46 \times 46$ cm internally, requiring approximately 160 L of water per experiment day. A large part of the day is spent filling the tank with deionized water, degassing the water, heating the water to a biologically relevant temperature (*e.g.* 37°C), and emptying the tank. Typical times were 4 to 6 hours to set-up and about 30 minutes to tear-down.

Second, setting up the ultrasound exposure conditions is difficult without proper training and experience. The position and orientation of the cell culture needs to be determined with respect to the 3-axis micropositioning system on a day-to-day basis before experiments in order to ensure the ultrasound exposure is performed consistently at different

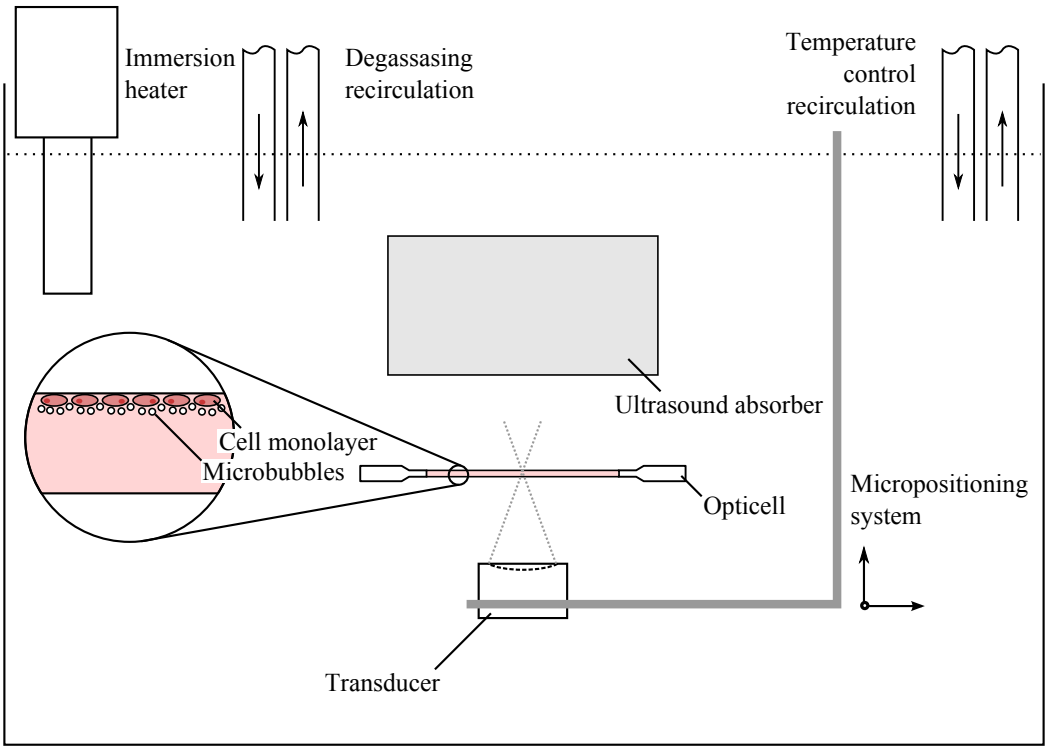

Figure 2.1: The previous sonoporation experimental set-up which used a large water bath (∼160 L), a single-element focused transducer, a micropositioning system, an Opticell chamber, an immersion heater, a circulating heater, and a circulating degasser.

target locations across the cell culture. This involves first levelling the cell culture mounting apparatus and then localizing three holes on the apparatus, quasi-manually (*i.e.,* with the aid of software), using pulse-echo and scanning techniques.

Third, sonicating the cell culture takes considerable time as well due to the system design. The system uses one single-element focused ultrasound transducer to perform multiple acoustic exposures across the target cell culture. The process of sonicating each target is automated using custom `MATLAB` software which controls the micropositioning system and waveform generator. Due to the need to move and treat each zone sequentially, the total treatment time was on the order of 25 minutes per cell culture.

Many of these issues stem from the use of general-purpose equipment to perform a specific task. A person wishing to use or build such a system must have sufficient knowledge in each of the system's constituent components (*e.g.* knowledge in software engineering, electrical engineering, and acoustics) or the aid of people who do. Fortunately, these issues can be addressed by designing a device for the specific application, minimizing the

required technical expertise of the operator.

2.1.2 Proposed System

In this work, a sonoporation system is proposed which aims to reduce the time and expertise required to perform sonoporation on cell cultures in adherent monolayer. The design consists of an array of ultrasound transducers (*i.e.,* multiple independent acoustic sources) affixed beneath an Opticell mounting stage (Figs. 2.2 and 2.3).

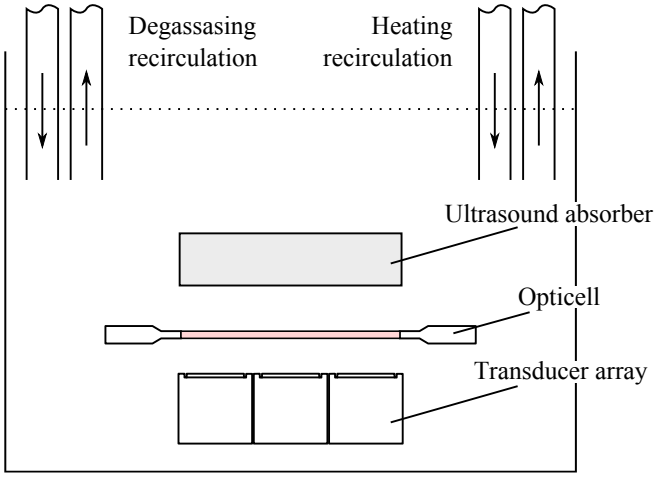

Figure 2.2: The proposed sonoporation experimental set-up with a much smaller bath (∼20 L), multiple fixed transducers, and simpler heating system.

The features of the proposed design address all of the issues with the previous system. First, the compact size of the device reduces the required size of the ultrasound bath which in-turn reduces the required bath set-up, treatment, and tear-down times. Second, the distances between the transducers and the cell culture are set once and do not change between experiment days, reducing the time and complexity of the set-up of the exposure conditions. Lastly, multiple transducers can insonate multiple areas of the cell culture either concurrently, reducing the treatment time to that of a single exposure (*e.g.* 30 seconds), or sequentially, eliminating the movement times associated with the use of a micropositioning system. The design, construction, and calibration of the proposed system are outlined in the following sections of this chapter.

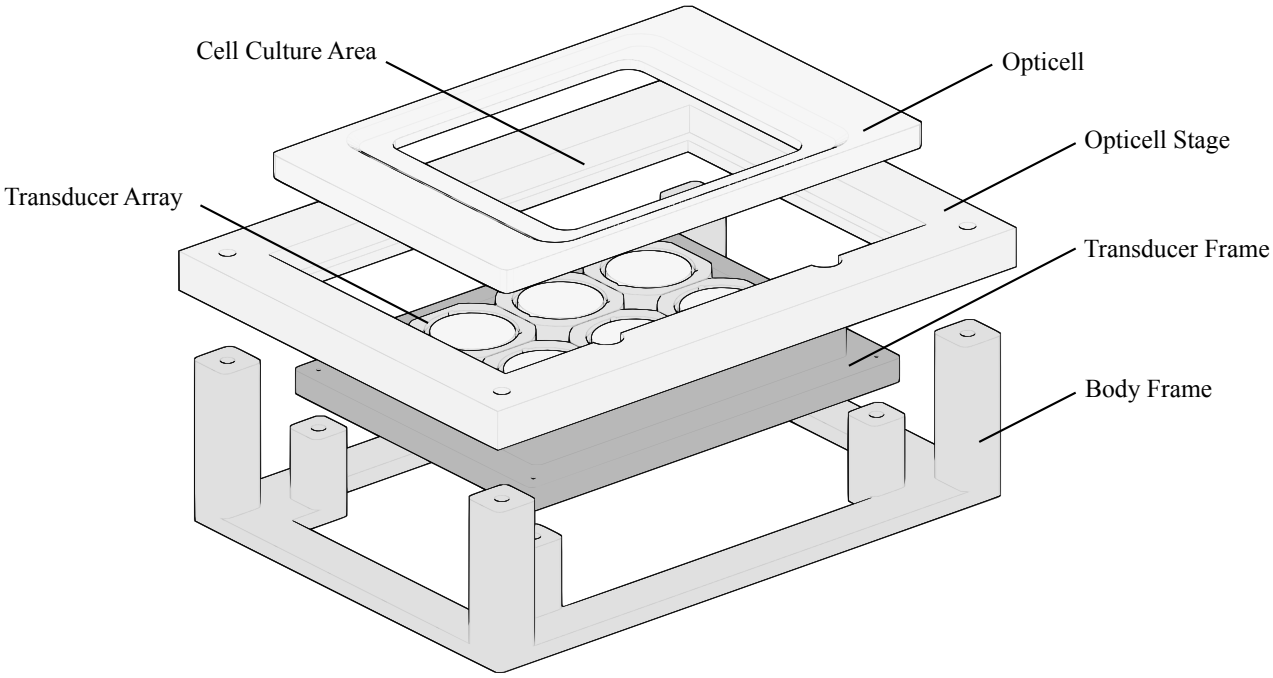

Figure 2.3: A rendering of the device (exploded) showing its transducer array, transducer frame, body, Opticell stage, and Opticell.

2.2 Transducer Design

The general construction of the type of transducer used here is shown in Fig. 2.4. This transducer consists of a piezoelectric element (responsible for converting energy between electrical and mechanical forms) positioned between two other material layers: a matching (front) material and a backing material. The front matching material is used to match the acoustic impedance of the piezoelectric material to the acoustic impedance of the surrounding medium (*e.g.* the ultrasound bath water) [47, 48]. The backing material is used to aid in the physical damping of the piezoelectric element as well as to reflect (or absorb) acoustic energy [47, 48]. A housing is used to hold together the piezoelectric element, the backing and matching materials, and the electrical circuitry.

The acoustic parameters chosen for the design of the proposed system were adopted from those used with the previous system in a number of sonoporation studies [20–22]: 0.7 MPa peak-negative pressure, 1 MHz, 4.8% duty cycle, 1.6 kHz pulse repetition frequency. These parameters were chosen in order to compare the effectiveness of the proposed system with the previous system.

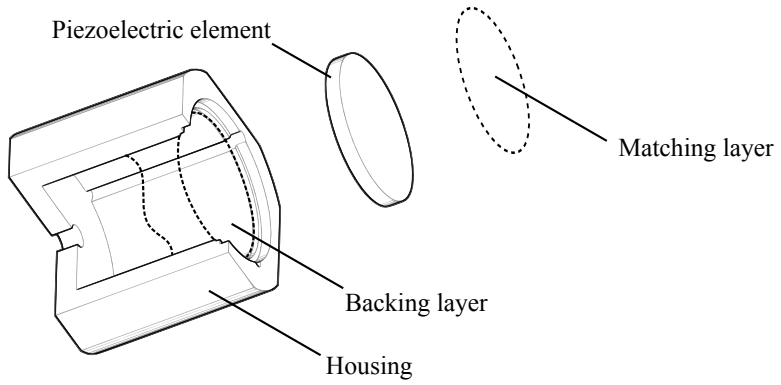

Figure 2.4: A rendering of a transducer (exploded) showing its housing (cut-away), its backing layer (dotted outline), its piezoelectric element, and its matching layer (dotted outline).

The design of the transducers began with the choice of the piezoelectric elements. In order to reduce the complexity of the device while providing a large exposure area, a large number of small transducers was desired. After consultation with the manufacturer, the suggested piezoelectric elements which would fulfill the design requirements were 20 mm (nominally) in diameter (DL-47; DelPiezo Specialties LLC, West Palm Beach, FL, USA). The dimensions of the Opticell allowed for an array of six (3×2) of these piezoelectric elements to fit comfortably within the cell culture area (Fig. 2.5).

The transducers were designed to be air-backed. Air has a much lower acoustic impedance than the piezoelectric crystal material (∼410 Rayl v. ∼26 MRayl). Therefore, this backing layer will be highly reflective of acoustic energy being transmitted out of the back of the crystal [47]. The water in front of the transducer has an acoustic impedance much closer to the crystal material than air, though still an order of magnitude less (∼1.5 MRayl v. ∼26 MRayl). Although the maximum transfer of energy occurs when acoustic impedances are equal, no front material was used to match the acoustic impedance between the crystal and the water bath.

Important physical features of the transducer housing are shown in Fig. 2.6. The transducer housing has openings at both ends. The wide opening at the top of the housing is designed to accept a circular piezoelectric element and a small "lip" was designed into this opening for the piezoelectric element to rest (Fig. 2.6:2). The opening widens near the top of the housing to allow for epoxy (EPO-TEK 301; Epoxy Technology, Billerica, MA, USA) to be set between the housing and the piezoelectric element (Fig. 2.6:1). This

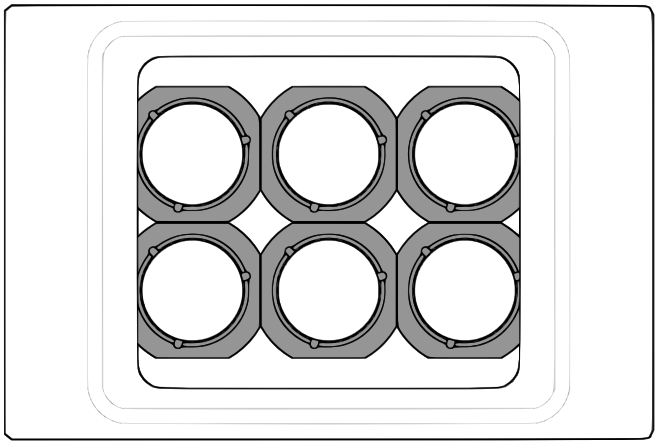

Figure 2.5: An orthographic projection showing the placement of the six transducer elements with respect the Opticell cell culture area.

epoxy both holds the piezoelectric element in place and provides waterproofing for the transducer air-backing. The opening at the bottom of the housing allows for the electrical signal cable to be inserted (Fig. 2.6:4) (also sealed with epoxy). Three vertical channels are evenly spaced around the inside of the housing which allow ground (GND) wires to be connected from the signal cable termination inside the housing to the external face of the piezoelectric element (Fig. 2.6:3).

2.3 Modelling and CAD

The device components were modelled using `OpenSCAD` (2013.02.28) [49], a tool which provides a language-based interface for modelling 3D objects using constructive solid geometry (CSG). Models created in `OpenSCAD` were exported to stereolithography format (`.stl`) and prepared for printing using `ReplicatorG` (0037) [50] with `skeinforge` (50) [51]. The 3D objects were then printed using a Makerbot Replicator desktop 3D printer (Makerbot Industries, New York, NY, USA) using ABS plastic. ABS plastic was chosen after a sample piece underwent a soak test and its wet mass was not largely different from its dry mass, signifying that it did not absorb a significant amount of water.

`ReplicatorG` and `skeinforge` provide options for adjusting the density of the objects being printed. This is done by using a solid wall for all external surfaces of the object and using a supporting structure of lesser density, such as a honeycomb, internally. The remainder of the internal volume of the object is occupied by air. The printed pattern

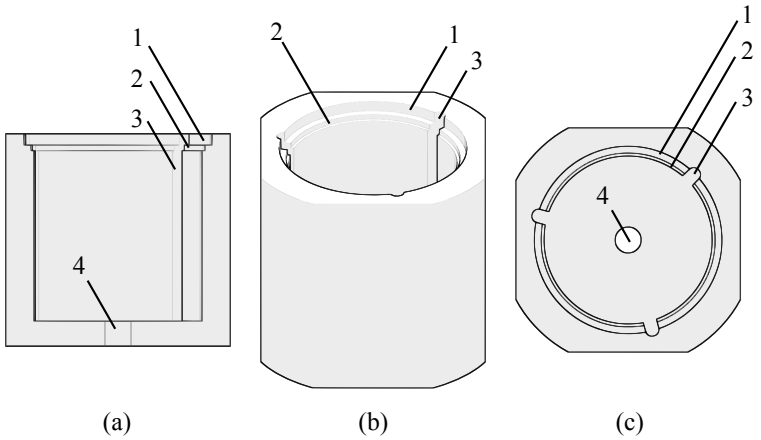

Figure 2.6: Physical features of the transducer housing design: (1) a gap between the transducer and the housing for epoxy to be placed; (2) a small lip for the transducer to rest on; (3) channels for ground (GND) wires to be run from the inside of the housing to the outside; and (4) the hole for the coaxial cable. These parts can be seen (a) from the side (cutaway), (b) from an angled perspective, and (c) from above.

for the internal structure can be adjusted for density, affecting the time and material requirements for printing. Since it is necessary for the device presented here to be fully submerged in a water bath, these options were adjusted to achieve maximum fill density for every part of the device in order to minimize the internal air gaps, to minimize leaking and absorption, and to allow for the tapping of holes for fixing screws.

2.4 Transducer Construction

The exterior of each transducer housing was treated in a shallow acetone bath for 1 to 2 seconds per side. The acetone treatment was performed to smooth and help fill the rough exterior in order to minimize the possibility of leaking.

Coaxial cable (RG-174 type, 24.5 AWG; Belden, St. Louis, MO, USA) was used to connect to the piezoelectric element to the driving circuitry. The end of the coaxial cable was fed through the bottom hole before connecting to the piezoelectric element. Six electrical connections were made between the coaxial cable and the piezoelectric element (Fig. 2.7) using 26 $\sim$ 30 AWG stranded wire. Three connections to ground (GND) were evenly spaced around the outside edge of the exterior-facing side of the crystal and three signal connections were made on the interior-facing side of the crystal. The signal connections were staggered evenly with respect to the positions of the ground connections

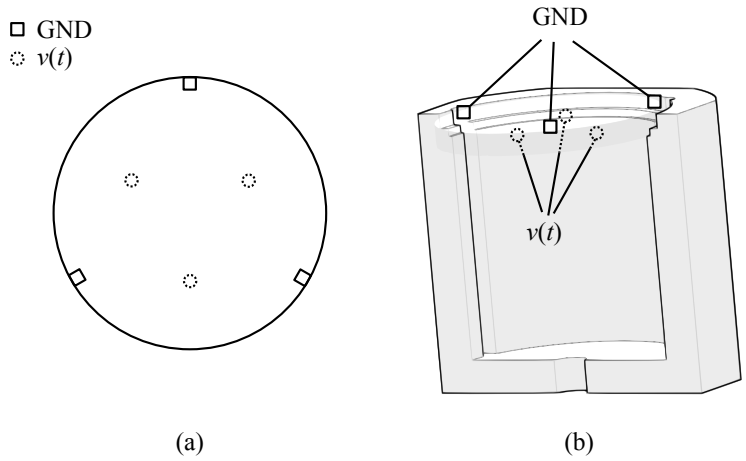

Figure 2.7: (a) Locations of solder points for the signal $v(t)$ (circles) and ground (GND) connections (squares). (b) A cut-away of the housing showing the internal and external connections to the (translucent) piezoelectric element. Ground connections are made on the outer-facing side of the element and the signal is applied to the inside-facing side of the element.

and made half-way between the center of the element and its edge (Fig. 2.7a).

2.5 Transducer Electrical Matching

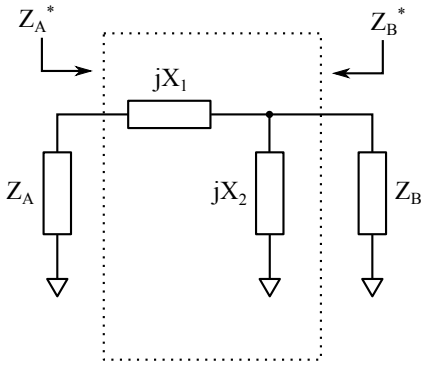

Figure 2.8: L-type (two-element) matching network where $\mathbb{R}e\{Z_B\} > \mathbb{R}e\{Z_A\}$.

The electrical impedance of each transducer was matched to 50 Ω at 1 MHz using an L-type (two-element) matching network (Fig. 2.8). The goal of the matching network is

to ensure that maximum power is transferred between Z_A and Z_B [52]. While the quality factor of this type of network cannot be controlled, it is normally low [52].

L-type matching networks come in low-pass and high-pass varieties. In the low-pass L-type matching network, the series reactance, X_1, is an inductor, and the parallel reactance, X_2, is a capacitor. For the high-pass case, the opposite is true. In both cases, the parallel reactance X_2 is in parallel with the component with the larger $\mathbb{R}\mathrm{e}\{\mathrm{Z}\}$. Thus, there need not be any differentiation between which is the source and which is the load when performing the analysis [52].

Matching is performed for a single frequency by satisfying the following equality:

$$Z_A^* = Z_1 + Z_2 \| Z_B \tag{2.1}$$

$$R_A - jX_A = jX_1 + \left(jB_2 + \frac{1}{R_B + jX_B} \right)^{-1} \tag{2.2}$$

where X_1 and B_2 are the reactance of the series matching component and the susceptance of the parallel matching component respectively. If $X = X_1 + X_A$ then the solution to the matching circuit can be found by equating the real and imaginary parts and solving for X and B_2:

$$B_2 = \frac{X_B}{|Z_B|^2} \pm \sqrt{\frac{R_B}{R_A}} \frac{\sqrt{|Z_B|^2 - R_A R_B}}{|Z_B|^2} \tag{2.3}$$

$$X = X_1 + X_A = \frac{1}{B_2} + \frac{R_A}{R_B} \left(X_B - \frac{1}{B_2} \right) \ . \tag{2.4}$$

Due to the compact size of the transducer housings, matching networks were installed in small boxes placed between the 50 Ω source and the terminated end of the coaxial cable of each transducer (Fig. 2.9). Hence, the impedance matching involved the impedance of both the piezoelectric element and the coaxial cable.

Matching was performed with the aid of an RF network analyser (8127ES; Hewlett Packard, Palo Alto, CA, USA) calibrated to using a 85032E Type N calibration kit (Hewlett Packard, Palo Alto, CA, USA). The matching network was manually tuned from initial values by adjusting the inductance by the number of turns on the inductor and the capacitance by adding or removing parallel capacitors with the aid of a Smith chart [52]. The results of the matching procedure are listed in Table 2.1.

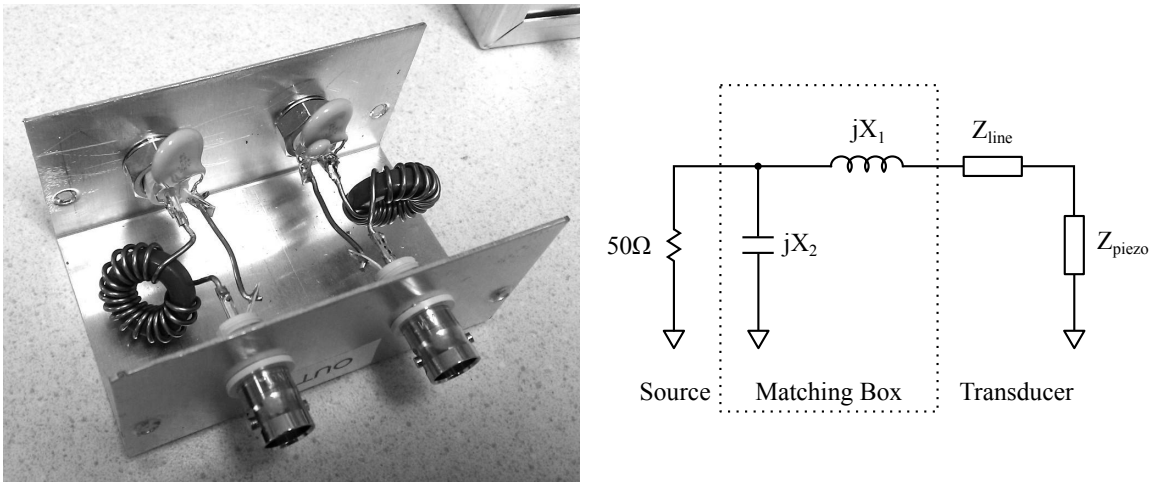

(a) (b)

Figure 2.9: (a) The inside of a matching box with two L-type low-pass matching circuits and external male BNC connectors featuring hand-wound iron-powder-core (Material #1; Amidon Inc., Costa Mesa, CA, USA) toroid inductors and high-voltage ceramic capacitors. (b) A schematic showing the matching circuit in place. The matching network input calibrated to 50 Ω and the load impedance includes both line and piezo-element impedances. While the matching network shown assumes $\mathbb{R}\mathrm{e}\{\mathrm{Z}_{\mathrm{line}} + \mathrm{Z}_{\mathrm{piezo}}\} < 50\ \Omega$, this may not be true, in which case X_2 would be in parallel with $Z_{line} + Z_{piezo}$ instead.

Device	Unmatched Z (Ω)	L (μH)	C (nF)	Matched Z (Ω)	Matched $\lvert\Gamma\rvert$
A	$45.78 + j7.028$	1.09	0.966	$50.85 + j1.402$	0.01626
B	$50.76 - j8.435$	1.65	0.127	$50.98 + j2.029$	0.02231
C	$30.36 - j6.428$	4.91	2.56	$48.21 - j1.603$	0.02446
D	$44.13 - j4.374$	3.26	1.16	$50.15 - j0.739$	0.007529
E	$47.34 - j8.224$	3.09	0.755	$48.57 - j1.585$	0.02165
F	$46.97 - j2.415$	2.28	0.808	$52.71 - j0.439$	0.02673

Table 2.1: The unmatched and matched impedances ($Z = R + jX$) at 1 MHz for each transducer, the (theoretical) component values to match to 50 Ω at 1 MHz, and the reflection coefficient magnitude $\lvert\Gamma\rvert$ after matching.

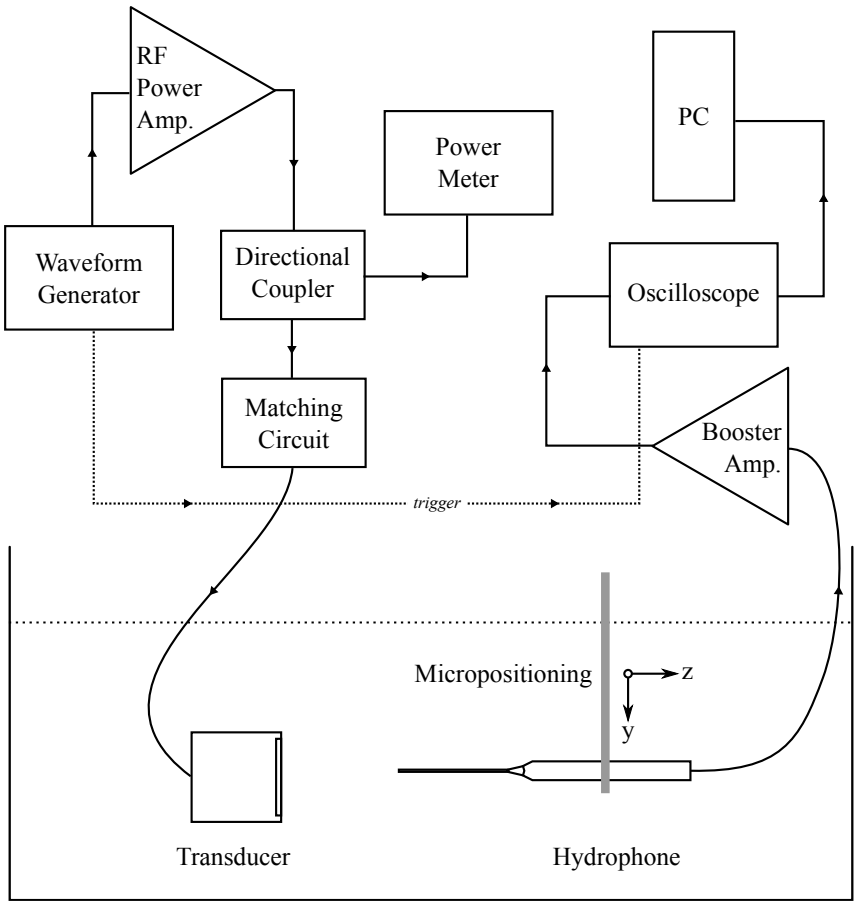

Figure 2.10: Hydrophone scanning acquisition set-up. The output of a waveform generator (1 MHz, 30 cycles, 10 Hz PRF) is first amplified by an RF power amplifier. The electrical output power is measured using a directional coupler and power meter. The amplified signal is sent to the matching circuit and transducer. The acoustic pressure generated by the transducer is converted to a voltage using a hydrophone. The hydrophone is attached to the arm of a 3-axis micropositioning system. The hydrophone signal is (optionally) boosted by a booster amplifier before being captured by an oscilloscope. A PC reads the captured hydrophone voltage waveform from the oscilloscope for processing.

2.6 Transducer Field Characterization

2.6.1 Acquisition Set-up

Hydrophone scanning was employed to obtain a detailed map of the acoustic profile of each transducer. Measurements were conducted using a previously calibrated needle hydrophone using a 0.2 mm tip (SN1426; Precision Acoustics, Dorsetshire, UK). An ultrasound pulse was generated using an arbitrary waveform generator (33522; Agilent Technologies Canada Inc., Mississauga, ON, Canada) and amplified using a linear RF amplifier (A250; E&I, Rochester, NY, USA). This pulse was defined as a 1 MHz pulse of 30 cycles, generated every 100 ms (10 Hz). The hydrophone was placed at various positions within the acoustic beam of the transducer under test using a 3-axis motorized micropositioning system (UMS2; Precision Acoustics, Dorsetshire, UK). Automatic positioning and waveform acquisition was performed using a custom `MATLAB` programme. A schematic for the acquisition setup is shown in Fig. 2.10.

The acoustic field was reconstructed automatically using a custom `MATLAB` programme. At each point the hydrophone visited, the software obtained the hydrophone voltage waveform and computed its root-mean-square (RMS) value. The RMS value was calculated from the beginning of the pulsed waveform to the end of the pulsed waveform, which may be offset in time from the moment of excitation based on the distance of the hydrophone from the transducer and the speed of sound of the water bath. The acoustic field pulse-average intensity ($\mathcal{I}_{sppa}$) for the given point in space will be proportional to the square of the computed RMS hydrophone voltage [18]:

$$\mathcal{I}_{sppa} = \frac{(p_{rms})^2}{\rho c} = \frac{\left(V_{rms}/M(f)\right)^2}{\rho c} \tag{2.5}$$

where c and ρ are the speeds of sound and density of the propagation medium, and p_{rms} is the pulse-averaged pressure which is proporational to the calculated RMS hydrophone voltage by the linear response of the hydrophone $M(f)$ at operating frequency f [53].

The custom `MATLAB` acquisition programme is only capable of performing scans along the axes of the positioning system. This limitation required the transducer beam axis to be physically aligned with one of the three micropositioning system axes. Additional recommendations for performing hydrophone measurements, including alignment, were available from the manufacturer [53].

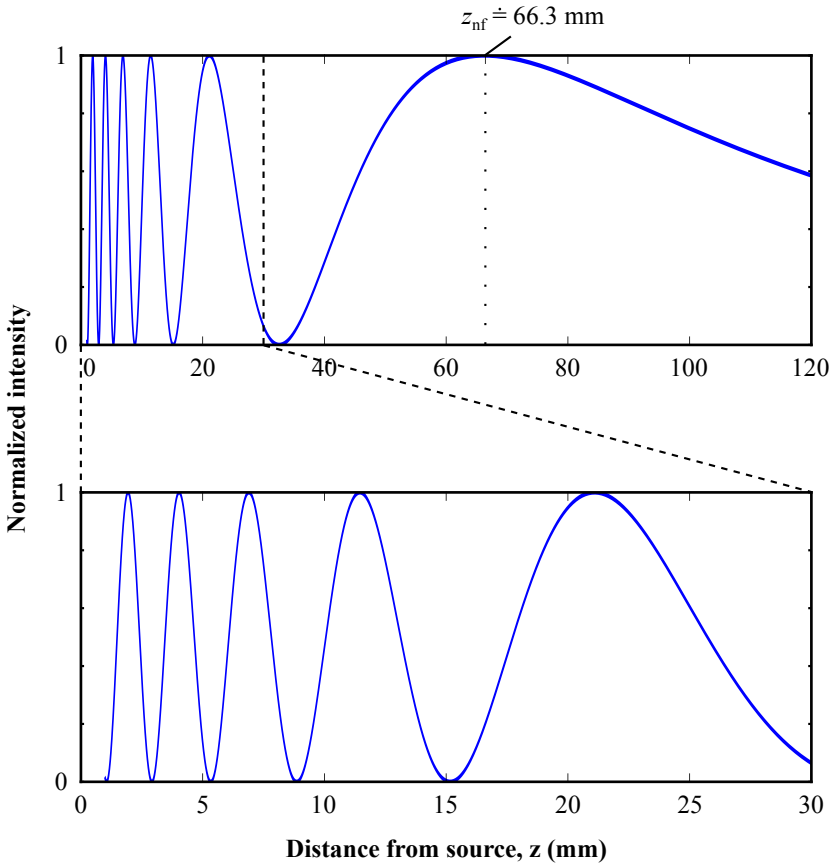

Figure 2.11: Normalized intensity along the acoustic axis for an ideal disc source 20 mm in diameter, operating at 1 MHz in water ($c = 1500$ m/s).

2.6.2 Optimal Treatment Plane

Unlike curved (focused) transducers, planar transducers do not have a geometric focus. However, they do have what is considered a "natural focus", a distance where the acoustic field transitions from the near- to the far-field (z_{nf}) [48]. The acoustic field in the near-field ($z < z_{nf}$) is highly heterogeneous due to the constructive and destructive interference of waves contributed by different points on the transducer's surface. At a given point near the source, the distance between each point on the surface of the source and this point in space varies greatly across the surface, leading to large changes in phase contributions. However, in the far-field ($z > z_{nf}$), the distances between points on the surface of the transducer and a given point in space become more similar and the acoustic field becomes more homogeneous.

The normalized intensity $\mathcal{I}/\mathcal{I}_{peak}$ along the propagation axis for an ideal disc source is

given by

$$\frac{\mathcal{I}}{\mathcal{I}_{peak}} = \sin^2\left\{\frac{a^2}{\lambda}\left(\sqrt{a^2+z^2}-z\right)^2\right\} \tag{2.6}$$

where a is the radius of the disc source, λ is the wave length of the medium, and z is the distance along the propagation axis [48]. The distance at which the near-far field transition (*i.e.,* the natural focus) occurs for an ideal disc source is given by

$$z_{nf} = \frac{4a^2-\lambda^2}{4\lambda} \tag{2.7}$$

where a is the radius of the disc source and λ is the wave length of the medium [48]. At this distance, the intensity along the propagation axis, given by (2.6), peaks for a final time before decaying [48].

The solution to (2.6) for a disc source 20 mm in diameter, operating at 1 MHz in water ($c = 1500$ m/s) is plotted in Fig. 2.11. For this source the near-far field transition distance is approximately 66.3 mm.

In order to develop a compact device, it may be necessary to work within the near-field region. In [15], sonoporation is performed in the near-field with minimal spacing between the transducer and cell culture as the authors consider the treatment plane homogeneous at this distance. It is possible, however, to find an optimal treatment plane in the near-field which exhibits a resonable level of homogeneity.

To determine the optimal near-field treatment plane, planar scans of the acoustic field were performed in the near-field region. The planes were 10.5×10.5 mm in size at a resolution of 0.7 mm ($< {}^1\!/_2\lambda$). These planes were obtained between 10 mm and 20 mm from the transducer surface. This range was chosen as it encompasses the region between the last two intensity peaks before z_{nf} (Fig. 2.11).

A circular region, 10.5 mm in diameter, was sampled to encompass the symmetry of the field while computing the homogeneity of the field on the plane (Fig. 2.12b). The homogeneity was quantified as the standard deviation from the mean intensity within this circular region. The optimal plane was the plane where the standard deviation was minimum (*i.e.,* minimum variation in acoustic intensity from the mean) and the axial distance at which this plane occurred became the "optimal treatment distance" (Fig. 2.13). The optimal treatment distance for each transducer is summarized in Table 2.2.

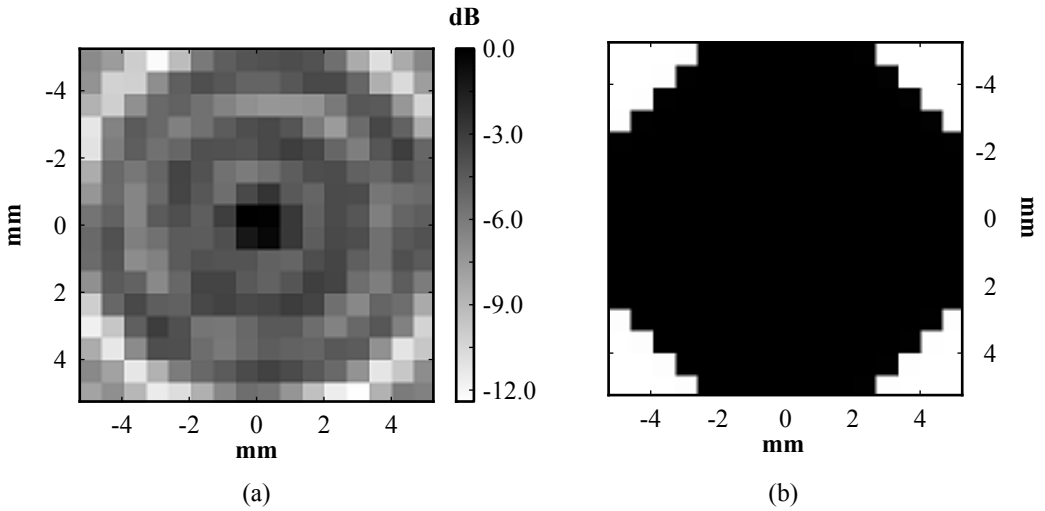

Figure 2.12: (a) A planar acquisition ($\Delta_x = \Delta_y = 0.7$ mm) showing relative acoustic intensity at z=16 mm; (b) A binary mask used to sample acoustic field intensity (where black) for homogeneity.

2.6.3 Electrical Power Required to Produce Peak Pressure

Once the optimal plane was identified for a given transducer, the electrical power required to produce the desired acoustic pressure (*i.e.,* 0.7 MPa peak-negative) on this plane was determined. The booster amplifier was removed and the hydrophone signal was measured directly by the oscilloscope. A dual-directional coupler (C5685-10; Werlatone Inc.) and power meter (2× N8482H sensors and N1914A meter; Agilent Technologies Canada Inc., Mississauga, ON, Canada) were used to measure the total forward electrical power. The hydrophone was positioned at a point on the optimal treatment plane which had approximately 90% of the peak intensity and the waveform generator's output voltage was slowly adjusted up from 0 $\mathrm{mV_{pp}}$ until the oscilloscope measured the desired peak-negative voltage. This peak voltage was determined by the hydrophone's linear sensitivity, $M(f)$, provided by the manufacturer:

$$p(\mathbf{r}, t) = \frac{V(\mathbf{r}, t)}{M(f)} \tag{2.8}$$

where $p(\mathbf{r}, t)$ and $V(\mathbf{r}, t)$ are the pressure and corresponding hydrophone voltage at spatial point $\mathbf{r}$ and time t [53]. The results of the acoustic field characterizations are summarized in Table 2.2.

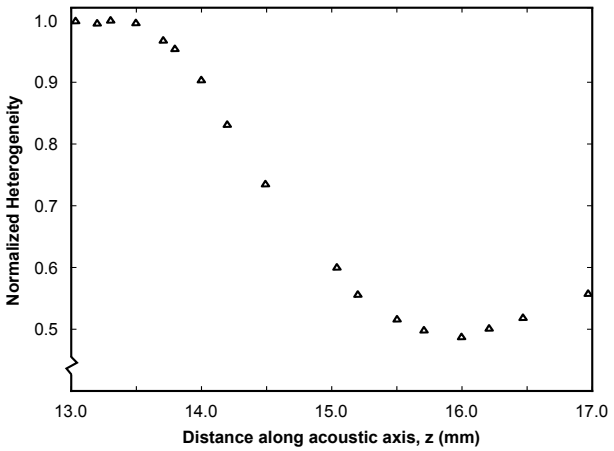

Figure 2.13: The heterogeneity (s.d.) of the acoustic intensity over a centered, circular region on each plane along the acoustic axis of a transducer. The minimum relative heterogeneity is seen at $z = 16$mm represents the most homogeneous plane. This distance ($z = 16$mm) is chosen as the optimal treatment distance for the transducer.

2.6.4 Cross-talk

Each transducer in the array is approximately 6 mm apart at their closest point. In order to determine the risk of cross-talk between adjacent transducers, the acoustic field for one of the transducers was acquired over a wider plane, 40×40 mm in size, at the transducer's treatment distance (Fig. 2.14). The widths where the relative acoustic intensity is -3 dB, -6 dB and -12 dB are approximately 2.18 mm, 10.5 mm, and 18.9 mm respectively. Peaks of approximately -18 dB appear in adjacent zones.

2.7 Transducer Array Configuration

The final step in the construction of the sonoporation platform was configuring the transducer array. The transducer positions were adjusted such that the distance between the each transducer face and the target Opticell membrane were as close as possible to the optimal treatment distances obtained from the acoustic characterization.

In order to accurately measure the distance between a transducer and the Opticell membrane, a secondary (imaging) transducer was used to generate a pulse and measure the resultant echoes (Fig. 2.15). One of the two membranes of a dummy Opticell was removed to prevent its unwanted echo. The transducer array was fixed and levelled in the ultrasound bath and the imaging transducer was aimed at the transducer being adjusted.

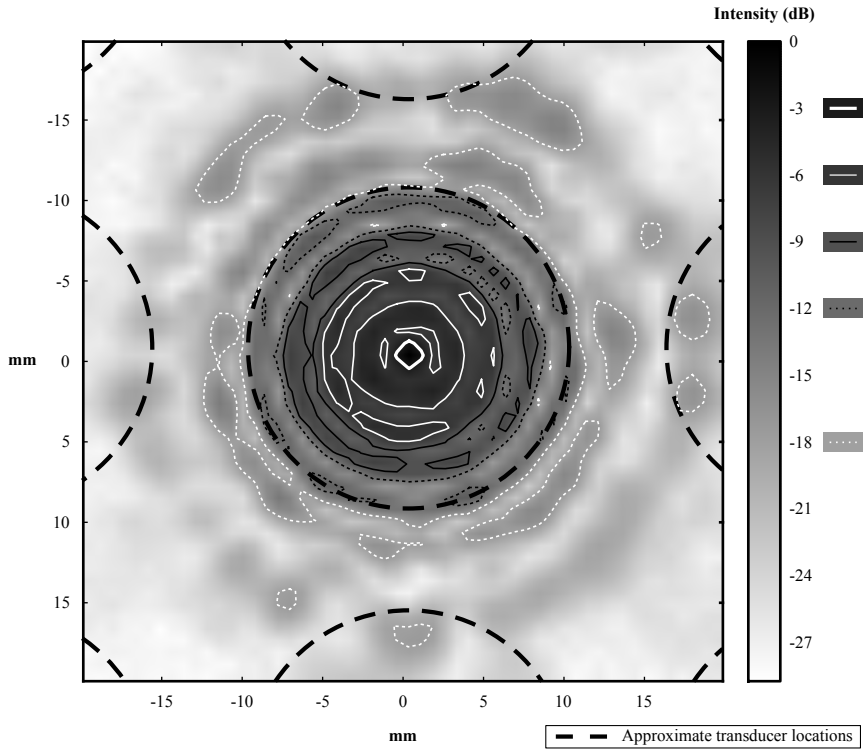

Figure 2.14: The planar acoustic profile of a transducer over a wide area at its optimal treatment distance. Orthographic projections of 20 mm circular transducers are overlaid (black, thick-dashed) to represent adjacent zones. Peaks of approximately -18 dB appear in neighbouring zones.

The echo from the Opticell membrane arrived first at time t_1 and the echo from the transducer surface arrived second at time t_2. The difference in time between the echoes is directly proportional (by the speed of sound in the bath) to the relative distance between the transducer face and the Opticell membrane:

$$\Delta d = \frac{c\Delta t}{2} \tag{2.9}$$

where Δd is the relative distance between the transducer face and Opticell membrane, Δt is the difference in time between the echoes, and c is the speed of sound in the propagation medium (*i.e.,* water).

The transducer array was held in place with five set screws, one for each "row" and "column" of the array. The transducers were held in each row and column by frictional force produced by the set screw position. A single transducer was able to be adjusted (or

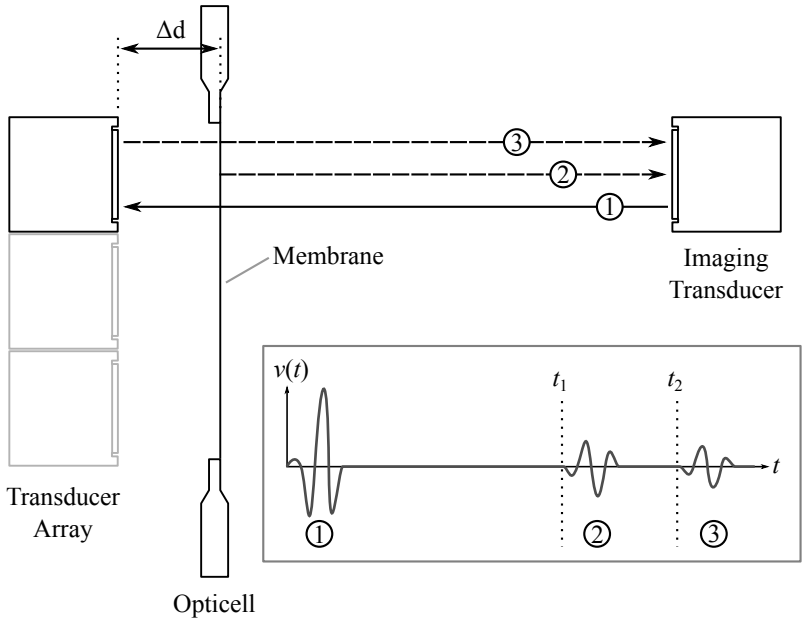

Figure 2.15: Setting the distances between the transducers and the Opticell membrane. A short pulse (1) is sent from an imaging transducer. After time t_1, the echo from the Opticell membrane (2) returns to the imaging transducer. Shortly after, at time t_2, the echo from the transducer face (3) returns to the imaging transducer. The transducer distance can be adjusted such that the time between echoes corresponds to the optimal treatment distance.

later replaced) by loosening both set screws for the row and column it belongs to. The other transducers in the same row remained in place by the force of the set screw in their columns and the other transducers in the same column remained in place by the force of the set screw in its row. When a transducer was adjusted to the desired position, the set screws for its row and column were tightened, fixing it in place. Once the transducer distances were set, the platform was ready for use (Fig. 2.16).

Device	Treatment distance (mm)	-3 dB width (mm)	Nominal source amplitude (mV_{pp})	Electrical power for 0.7 MPa (W)
A	17.0	2.33	410	106
B	16.0	2.18	380	94
C	14.7	1.68	370	94
D	16.0	1.78	360	85
E	15.8	1.96	430	123
F	15.9	1.89	390	106
Mean(±s.d.)	15.9(±0.67)	1.97(±0.22)	390(±23.8)	101(±12.2)

Table 2.2: Summary of transducer characterization

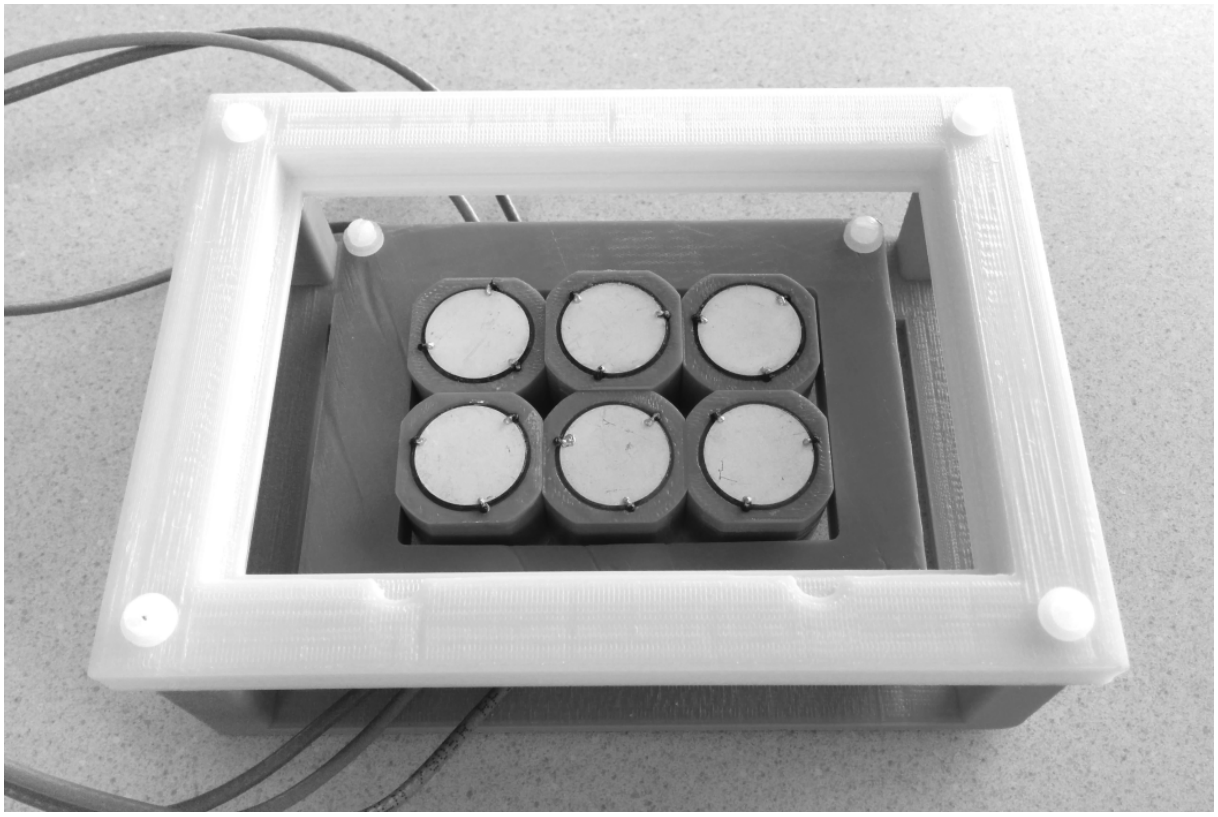

Figure 2.16: The platform constructed and ready for use.

Chapter 3

Platform Validation

3.1 Purpose

A sonoporation study was carried out using the prototype sonoporation platform. The purpose of this study was two-fold. First, the study aimed to examine the effect of cell temperature on sonoporation efficacy. Second, the study allowed for the design of the device to be experimentally validated.

Pore formation during sonoporation is mainly attributed to non-thermal mechanisms. There is evidence, however, that both cell membranes and microbubbles — two non-thermal actors associated with pore formation — have temperature-dependent qualities including cell membrane fluidity [44, 54] and microbubble population size [55–57] which may affect transfection efficiency and cell viability. In [44], increasing the temperature of the cells to 42°C gave a 15-fold improvement of transfection efficiency of prostate cancer PC-3 cells over the same treatment at 37°C.

Sonoporation is of particular interest to those in the field of cancer research as it promises to provide a non-viral means for targeted drug delivery and gene therapy. High-risk human papillomavirus (HPV) infection is strongly associated with the development of cervical cancer, the second most common cancer affecting women world-wide [58]. Currently, standard treatment of cervical cancer includes radiation therapy and surgery, each having their own undesirable side-effects. Ultrasound-mediated delivery of therapeutic macromolecules which target the oncoproteins encoded by the HPV DNA (e.g. plasmid DNA [15, 24] and small interfering RNA [14, 21]) may provide a minimally-invasive alternative to current treatment options.

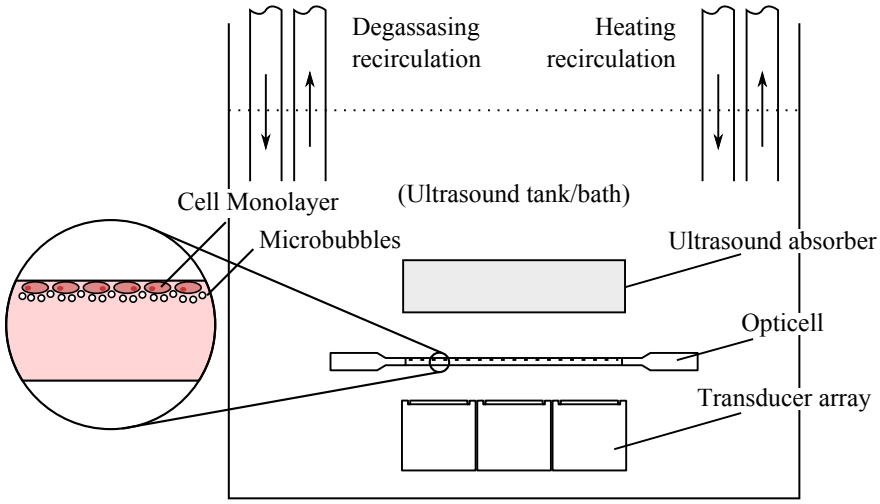

Figure 3.1: Sonoporation set-up featuring a transducer array below an Opticell chamber. Beyond the cell culture is an ultrasound-absorbent material (Aptiflex; Precision Acoustics, Dorsetshire, UK) intended to reduce reflection and standing wave formation.

3.2 Materials and Methods

3.2.1 Experimental Groups

Experiments were divided into nine groups consisting of three different treatments and three different temperatures. Cells either underwent a sonoporation treatment (US+UCA) which exposed the cells to high-intensity ultrasound with UCA present, an ultrasound treatment (US) which exposed the cells to high-intensity ultrasound without UCA present, or a sham ultrasound treatment (UCA) which used zero acoustic power (amplifier turned off) with UCA present. Each of these three treatments was performed at 37°C, 39.5°C, and 42°C with plasmid DNA present. All nine experimental groups were repeated three times.

3.2.2 Ultrasound Exposure

The ultrasound generation parameters used in the experimental validation were adopted from previous studies by our group [21, 22] in order to compare its relative performance with our previous system. These parameters were originally chosen based on preliminary work by our own group [20]. Pulsed ultrasound at 1 MHz delivered at a peak-negative pressure of 0.7 MPa to the cell culture in bursts of 30 cycles every 625 μs (4.8% duty

cycle; 1.6 kHz pulse repetition frequency) for a total time of 30 seconds.

The ultrasound signal for performing both characterization and sonoporation was generated using a waveform generator (33522; Agilent Technologies Canada Inc., Mississauga, ON, Canada) and amplified using a linear, radio-frequency power amplifier (A150; E&I, Rochester, NY, USA). The power during sonication was monitored using an in-line directional coupler (C5685-10; Werlatone Inc., Patterson, NY, USA) and power meter (2×N8482H sensors and N1914A meter; Agilent Technologies Canada Inc.) This setup allowed for the excitation of one transducer at a time during experiments. Hence, each treatment area of the cell culture chamber was treated sequentially in random order. An additional period of 30 seconds after each exposure was added to allow the operator to switch to the next transducer in the array.

3.2.3 Cell Culture and Plasmid DNA

Cervical cancer-derived SiHa cells (ATCC HTB-35, Manassas, VA, USA) were used in this study. Such cells contain 1-2 genome copies of HPV type 16 per cell [59]. The cells were maintained in 75 cm^2 flasks containing Dulbecco's Modified Eagle Medium (DMEM; Sigma-Aldrich, Oakville, ON, Canada) supplemented with 10% heat-inactivated fetal bovine serum (FBS; Hyclone Laboratories Inc., Logan, UT, USA), 100 U of penicillin, 100 μg of streptomycin, and 0.25 μg amphotericin B per mL (antibiotic/antimycotic; Gibco, Grand Island, NY, USA) at 37°C and 5% CO_2. The cells were passaged to maintain 70–80% confluency. Twenty-four hours before treatment, the cells were seeded (0.6×10^6) into an Opticell chamber to allow the cells to adhere to the inside membrane.

Plasmid DNA (pDNA) expressing green fluorescent protein (GFP) was used to quantify successful transfection. The GFP plasmid cannot passively cross the cell membrane, hence, green fluorescence will only be visible in successfully permeabilized cells. To produce the plasmid, chemically competent NEB 5-αF'I^q *Escherichia coli* bacteria (New England Bio Labs Inc., Ipswich, MA, USA) were transformed with 6.3-kb Omicslink pReciverM03 plasmid containing the GFP gene (Genecopia Inc., Rockville, MD, USA). Plasmid DNA was extracted and purified with EndoFree Plasmid Maxi Purification kits (Qiagen Inc., Toronto, ON, Canada) to minimize bacterial endotoxin levels. Prior to treatment, the cells were washed with serum and antibiotic-free DMEM and incubated with 250 μg of GFP plasmid DNA in 10 mL of serum and antibiotic-free DMEM for 15 minutes at 37°C and 5% CO_2.

Immediately following treatment, the Opticell was removed from the ultrasound bath,

wiped with 70% ethanol, and returned to the incubator where the cells were incubated at 37°C. The cells were given 2 hours of incubation time to stabilize after treatment. At this time, 1.1 mL of serum free media was removed from the Opticell and the remaining media was supplemented with 1 mL of FBS and 100 μL of antibiotic/antimycotic, returning the cells to their original media composition. The cells were then incubated for an additional 24 hours to allow for the development of GFP in the cells.

3.2.4 Ultrasound contrast agent

Definity ultrasound contrast agent (Lantheus Medical Imaging, North Billerica, MA, USA), consisting of bubbles of a perflutren gas core and lipid shell, was used to introduce cavitation nuclei during the sonoporation process. The contrast agent was activated according to the manufacturer's recommended procedures (Vialmix, Lantheus medical Imaging, North Billerica, MA, USA). For those experimental groups which included contrast agent, 33 μL of activated contrast agent was added to the 10 mL media in the Opticell chamber 1 minute before transferring to the water bath, giving a final volume concentration of 0.33%. Nominally, activated Definity contains 1.2×10^{10} microbubbles per mL corresponding to a microbubble-cell ratio of 660:1. However, in [18], the authors reported that many of the microbubbles in Definity UCA are small (<1 μm) and observed those on the range 1∼8 μm at ∼33 microbubbles per mL. This would correspond to ∼ 1.8 microbubbles per cell. During treatment, the Opticell was placed horizontally in the cell culture stage with the cells on the upper-most membrane, allowing for the microbubbles to rise and rest against the cells during insonation.

3.2.5 Bath Conditioning and Heat Treatment

Experiments were conducted in a bath of deionized, degassed water (Fig. 3.1). The bath water was initially circulated through a degassing system until the detectable level of dissolved oxygen was <1.0 ppm (407510A; Extech Instruments Corporation, Nashua, NH, USA). The water was also circulated through an in-line water heater (Model 210; PolyScience, Niles, IL, USA) to raise it to the desired temperature. The heater continued to circulate water throughout the duration of the experiment in order to maintain the temperature of the bath. The compact dimensions of the device allowed for experiments to be performed in a small water tank (a 26 L tote) reducing the time consumed by filling and emptying the tank as well as degassing and heating the water bath.

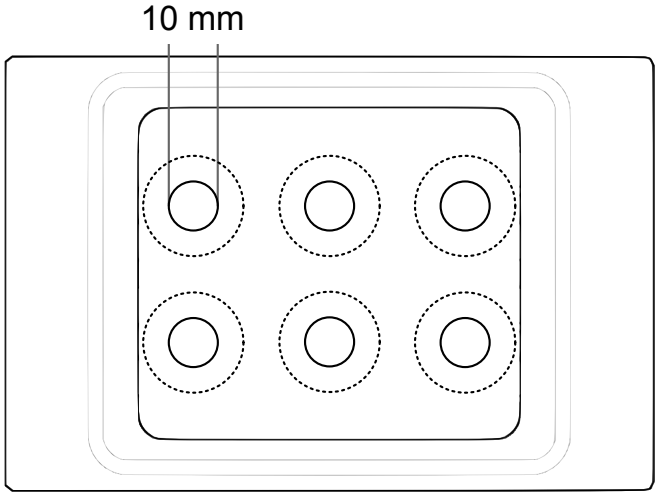

Figure 3.2: An illustration of the exposure zones and imaging areas. The Opticells were cut along the a 20 mm diameter region (dotted lines) to be treated for mounting on slides. Imaging occurred within the center 10 mm diameter region (approx. -6 dB intensity) of the cut-outs on slides (solid line).

The cells and medium in the Opticell chamber were given 1 minute to equalize with the temperature of the surrounding bath before starting the ultrasound exposure. This value was determined experimentally by measuring the time that water in an Opticell chamber took to rise from the temperature of the incubator (37°C) to the maximum bath temperature tested (42°C). Due to the large ratio between the surface area and the volume of the Opticell, the average time for this rise to occur was approximately 40 seconds, which was rounded up to 1 minute to ensure the temperature had stabilized.

Considering the initial temperature equalization time and subsequent treatment time, each Opticell was submerged in the bath for a total of 7 minutes.

3.2.6 Quantification of Permeabilization and Viability

Permeabilization and viability were quantified using microscopy and image processing (Fig. 3.2). Cell imaging was performed using a Zeiss Axiovert 200 inverted microscope (Carl Zeiss Canada Ltd., North York, ON, Canada) and an LD A-Plan 10×/0.25 Ph1 objective for a total magnification of 100×. A 12-bit CCD camera (Q Imaging, Surrey, BC, Canada) was used to capture the microscope images to digital format for processing. Each image taken measured 1376 ×1024 pixels, translating to an area of 2.752 ×2.048 mm at 50 pixels per μm.

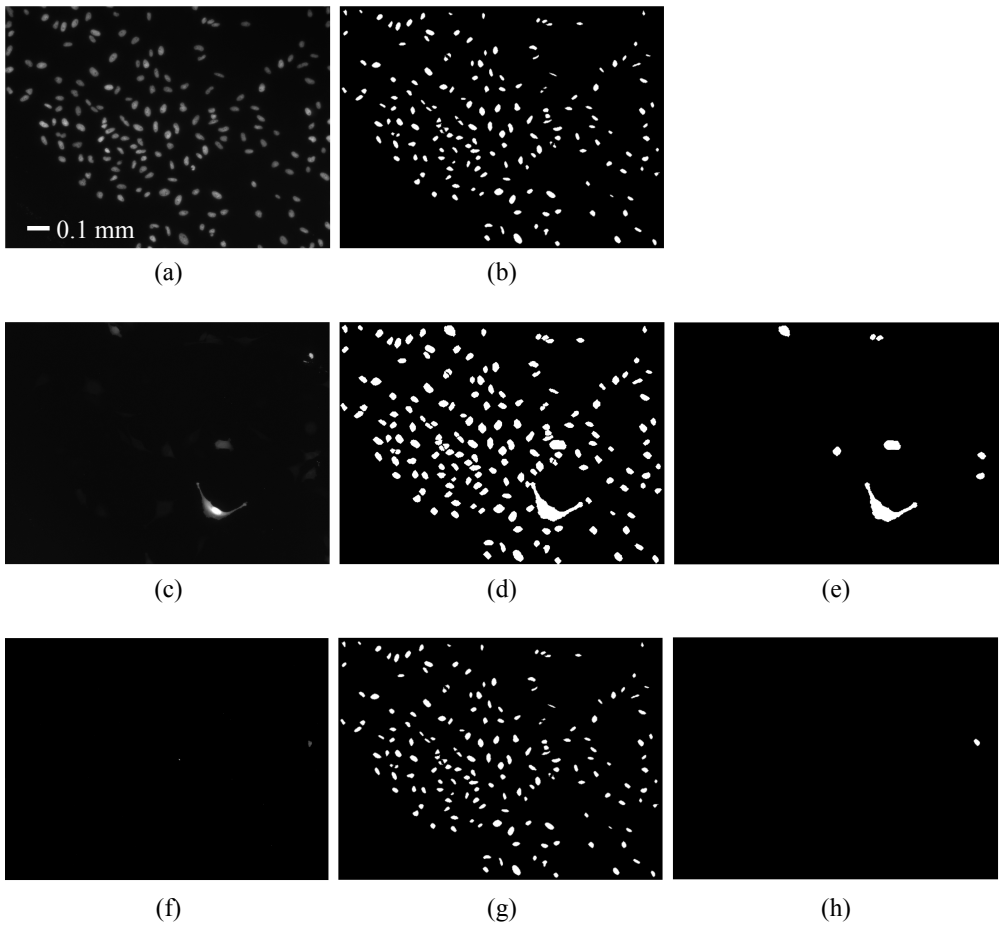

Figure 3.3: Various images used in transfection and apoptosis quantification. Images (a) and (b) are a blue DAPI intensity image and the associated segmented nuclei objects (white) respectively. Image (c) is a green GFP secondary antibody intensity image, (d) are the associated segmented cell objects (white), and (e) are the positive objects detected using (c) and (d). Image (f) is the red cleaved PARP secondary antibody image, (g) are the associated nuclei objects (from (b)), and (h) are the positive objects detected using (f) and (g).

Cell loss (detachment) was evaluated by imaging the cell cultures in three random spots per exposure area (18 total per replicate) 15 minutes before and 2 hours after treatment with phase contrast imaging. Each cell was manually identified by applying an identifying marker (a dot) over the digital phase contrast images and subsequently creating a new image containing only the dots on a blank background. These marked images were then used to automatically obtain cell counts per field of view using CellProfiler software (2.0.0) [60]. The cell counts per field of view were averaged per replicate for analysis. The cell loss for each replicate was evaluated as the relative change in the average cell count 15 minutes before and 2 hours after treatment where a negative relative change represented a drop in cell count. It was assumed that any cells that detached were non-viable. The viability of the remaining cells was determined by visualizing cleaved Poly (ADP-ribose) polymerase (PARP), an early apoptotic indicator, 24 hours after treatment.

Twenty-four hours following treatment, the Opticell membrane with the adhered cells was removed and the cells were fixed with a 4% solution of paraformaldehyde (PFA) in phosphate buffered saline (PBS). The fixed cells were permeabilized with 0.1% solution of Triton-X in PBS for 5 minutes and rinsed with PBS. The cells were then blocked with 1% solution of bovine serum albumin (BSA) in PBS for 10 minutes at room temperature. Since the fluorescent signal produced by the GFP was quenched by the PFA fixing, a goat polyclonal anti-GFP antibody (ab5450; Abcam Inc., Toronto, ON, Canada) was applied at 1:1000 in 1% BSA/PBS to bind to the GFP protein produced by transfected plasmid. A green fluorescent AlexaFluor 488 donkey anti-goat secondary antibody (LifeTechnologies Inc., Burlington, ON, Canada) was applied at 1:400 in 1% BSA/PBS to visualize the antibodies bound to the GFP. A monoclonal mouse anti-cleaved PARP antibody (ab1103315; Abcam Inc., Toronto, ON, Canada) was applied at 1:760 in 1% BSA/PBS and visualized with a secondary red fluorescent Alexa Fluor 594 donkey anti-mouse antibody (LifeTechnologies Inc., Burlington, ON, Canada) applied at 1:800 in 1% BSA/PBS. The cells were counter-stained with 4',6-diamidino-2-phenylindole (DAPI) to identify the nuclei of the cells before being mounted onto slides for imaging.

The stained cells were imaged in five random spots per treatment area using green, blue, and red fluorescence filters. One of the six treatment areas was used as a staining control, limiting the total available fields of view for analysis to 25 per replicate. Each field of view was captured for each of the three stains.

Object segmentation was performed on the fluorescent microscopy images (Fig. 3.3) using CellProfiler (2.0.0) [60]. Two types of "objects" (independent areas of the image)

were extracted in each field of view: 1) the nuclei objects, extracted from the blue DAPI images; and 2) cell boundary objects, extracted using a combination of the blue DAPI and green GFP secondary antibody images. These objects were extracted using an Ostu-global segmentation method with minimization of weighted variance. The extracted objects represented areas of the image occupied by individual nuclei (nuclei objects) or cells (cell boundary objects). Consequently, the background of the image was identifiable, based on the area not occupied by any object.

For an object to be considered positive for either transfection (green) or apoptosis (red), the image intensity inside the object should be significantly higher than the image intensity of the background. Thus, the following criterion was used to detect positive objects:

$$\bar{\mathcal{I}}_{obj} \geq \bar{\mathcal{I}}_{bg} + n\sigma_{bg} \tag{3.1}$$

where $\bar{\mathcal{I}}_{obj}$ is the mean image intensity within an object, $\bar{\mathcal{I}}_{bg}$ is the mean intensity of the background, σ_{bg} is the standard deviation of the background intensity, and n is the number of standard deviations that the mean object intensity must be from the mean background intensity for the object to be considered positive. In [21], a value of $n = 2$ was used with this method. This threshold was increased to $n = 3$ in this work. A cell was considered transfected if it met this criterion using the green GFP secondary antibody images. Cell boundary objects were used in transfection detection since the GFP secondary antibody signal would be observed in both the cytoplasm and nucleus of each positive cell (Fig. 3.3c-e). This same criterion was used for detecting cells positive for apoptosis using the intensity of the red cleaved PARP secondary antibody images. Since the cleaved PARP secondary antibody signal would be observed in the nucleus of each positive cell, the nuclei objects were used (Fig. 3.3f-h). The number of objects positive for transfection and apoptosis were counted relative to the number of cells in the image. The fraction of positive objects within each field of view was averaged per replicate for statistical analysis.

3.2.7 Statistical Analysis

Statistical analysis was performed using R (2.15.2) [61]. Observations were tested for normality using the Shapiro-Wilk test and homogeneity of variance using Bartletts test. A two-way ANOVA was used to test the effects on parametric data. A *post-hoc* Tukeys HSD (honestly significant differences) test was performed on significant effects. For non-

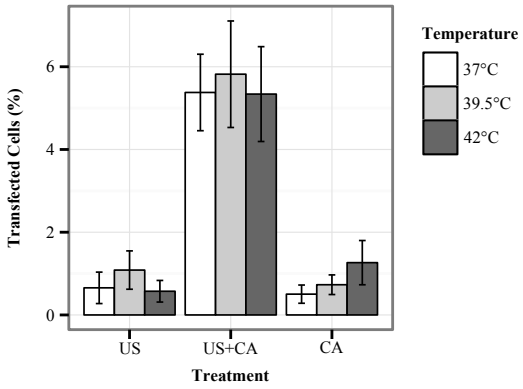

Figure 3.4: Transfection rates for each treatment and temperature tested. *Post-hoc* analysis showed that the US+UCA treatment group had significantly higher percentage of transfected cells over the other two treatment groups independent of temperature ($p<0.001$ for both). There was no significant effects observed in transfection rates with temperature or treatment-temperature mixed effects. *Error bars represent ±s.d. (n=3 per group)*

parametric data, the Kruskal-Wallis rank sum test was used to test effects and a *post-hoc* pair-wise Wilcoxon rank sum test was performed for significant effects. The significance level (α) was made 0.05 *a priori*.

3.3 Results

3.3.1 Transfection Efficiency

Treatment was observed to have a significant effect on transfection efficiency ($p<0.001$). *Post-hoc* analysis showed that the cells that received the sonoporation treatment (US+UCA) had a significantly higher expression of GFP over the control treatments ($p<0.001$ for both). Transfection efficiency was not observed to be significantly affected by bath temperature ($p=0.564$) or treatment-temperature interaction effects ($p=0.684$). Transfection rates for each experimental group are shown in Fig. 3.4. For temperatures of 37°C, 39.5°C, and 42°C the average(±s.d.) percentages of transfected cells for the sonoporation treatment (US+UCA) were 5.4(±0.92)%, 5.8(±1.3)%, and 5.3(±1.1)% respectively; the percentages of transfected cells for the ultrasound treatment (US) were 0.66(±0.38)%, 1.1(±0.46)%, and 0.57(±0.26)% respectively; and the percentages of transfected cells for the sham treatment (UCA) were 0.50(±0.22)%, 0.73(±0.24)%, and 1.3(±0.53)% respectively.

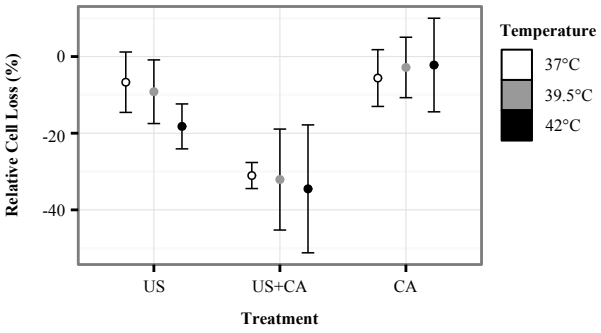

Figure 3.5: Relative change in cell count following treatment (+2h) for each treatment and temperature. *Post-hoc* analysis showed US+UCA treatment has significantly higher cell loss over the other two treatments ($p<0.001$ for both). There was no significant effects observed in transfection rates with temperature or treatment-temperature mixed effects. *Error bars represent ±s.d. (n=3 per group)*

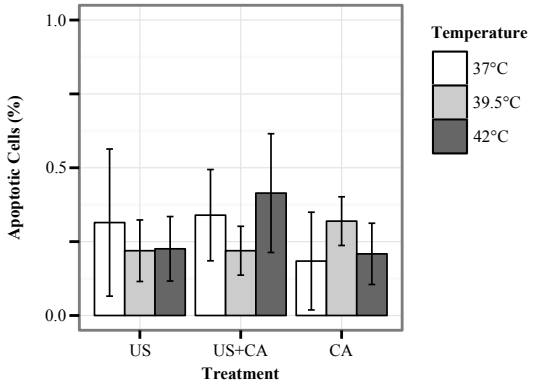

Figure 3.6: The ratio of apoptotic cells for each treatment and temperature. Apoptosis rates were low (<0.75%) across all treatments and temperatures. No significant effects on apoptosis rates were observed with treatment, temperature, or mixed-effects. *Error bars represent ±s.d. (n=3 per group)*

3.3.2 Cell Viability

Cell loss was not significantly affected by temperature (p=0.661) or treatment-temperature mixed effects (p=0.778). However, cell loss was found to be significantly affected by treatment (p<0.001). *Post-hoc* analysis showed that US+UCA treatment had significantly higher levels of cell loss over the US and UCA treatment groups (p=0.0076 and p=0.0002 respectively). Rates of cell loss following treatment for each experimental group are shown in Fig. 3.5. For temperatures of 37°C, 39.5°C, and 42°C, the cell losses for the US+UCA treatment group were -31(±3.4)%, -32(±13)%, and -34(±17)% respectively; cell losses for the US treatment group were -6.7(±7.9)%, -9.1(±8.3)%, and -18(±5.9)% respectively; and cell losses for the UCA treatment group were -5.6(±7.4)%, -2.8(±7.9)%, and -2.2(±12.2)% respectively.

The percentage of remaining cells indicating apoptosis 24 hours following treatment was low (<0.75%) and was not significantly affected by treatment (p=0.437), temperature (p=0.896), or treatment-temperature interaction effects (p=0.371). Rates of apoptosis for each experimental group are shown in Fig. 3.6. For temperatures of 37°C, 39.5°C, and 42°C, the ratios of apoptotic cells for the US+UCA group were 0.34(±0.15)%, 0.22(±0.08)%, and 0.41(±0.2)% respectively; the ratios of apoptotic cells for the US group were 0.31(±0.25)%, 0.22(±0.10)%, and 0.23(±0.11)% respectively; and the ratios of apoptotic cells for the UCA group were 0.18(±0.17)%, 0.32(±0.08)%, and 0.21(±0.10)% respectively.

3.4 Discussion

3.4.1 Validation

The design of the sonoporation device presented here was able to induce significantly higher expression of GFP over the control groups 24 hours following treatment. This device was chosen to operate under the similar excitation parameters as our previous system in order to compare its relative performance. In [22], our previous system produced a transfection efficiency of 6(±2)% with a cell detachment rate of -47(±32)% using similar excitation parameters, plasmid, and cell line. At 37°C, the system presented here was able to achieve a transfection rate of 5.4(±0.92)% with a cell detachment rate of -31(±3.4)%. The rates seen here are slightly lower than those seen with our previous system. As permeabilization has been noted to be dependent on the acoustic pressure [12,18], a lower

rate of permeabilization may be due to the use of 0.7 MPa here which is lower than the 1 MPa used in [22].

To the best of our knowledge, there are no other groups performing sonoporation on SiHa cells in particular. Furthermore, the acoustic excitation parameters, acoustic conditions, and impermeable agent used vary across the literature, making comparisons between different studies difficult. There are a number of studies on adherent cell cultures which exhibit similar rates of transfection albeit under different acoustic and experimental conditions. For example, in [15], sonoporation using 1 MHz pulsed ultrasound was examined under a number of different excitation parameters using a near-field set-up. The authors found that sonoporation at their optimal parameters (1 MHz, 0.25 MPa peak-negative pressure, 4% duty cycle, 1 kHz PRF, 10 s exposure, 4% SonoVue UCA concentration) was able to deliver plasmid DNA at a rate of ∼4% to Chinese hamster ovary (CHO) cells with ∼90% cell viability.

3.4.2 Cell detachment

The presence of UCA during ultrasound exposure not only had a significant effect on permeability but it also appeared to have a significant effect on cell detachment. There have been a number of reports of high levels of cell detachment among the same order as seen here [15, 25, 62]. The level of cell detachment due to ultrasound exposure alone (US group) was on the same order as the sham treatment (UCA group) at 37°C. Since the US+UCA group had significantly higher cell detachment over US alone and UCA alone, microbubble cavitation may be facilitating cell detachment. In [63], high-pressure shock waves were used to induce cavitation in an adherent cell culture. Using high-speed imaging, the authors found that cell detachment only occurred when cavitation activity was present. The reason for this, they suggested, was that the flow due to the cavitating bubble near the rigid substrate generated a shear force large enough to remove the cells from the substrate. Though the rarefactional pressure of the shock waves in [63] was large enough to induce cavitation without UCA present, a similar effect may have occurred at a lower pressure amplitude here due to the presence of the UCA.

3.4.3 Effects of temperature

The preliminary study of temperature on sonoporation efficacy resulted in no observable, significant, net-positive effect under our experimental conditions with increased bath

temperature. There are many actors involved in the sonoporation process which have temperature-dependent qualities which, together, may affect its efficacy. For instance, the cavitation of microbubbles is an important factor. Microbubble properties such as size distribution and stability have been shown to be affected by temperature [56, 57]. In [57], the mean microbubble diameter for SonoVue UCA (phospholipid-shell) was seen to increase with temperature and, after a few minutes, dropped abruptly. The growth of the microbubbles was thought to be occurring due to the gas expansion of the bubbles as well as the reduced surface tension of the shell. The phase transition temperature of the shell of SonoVue UCA has been noted to be around 40°C [56]. The decreasing stability with time was attributed to the possibility of a phase change of the shell since a similar drop was not observed at 37°C. Though the UCA used here (Definity) is not identical, there may be similarities in its temperature-dependent behaviour. That is, the higher temperatures may have affected both the microbubble size and stability of the Definity UCA during treatment. Here, the total treatment time was 7 minutes whereas the abrupt drop in SonoVue population observed in [57] occurred around 6 minutes. It may be the case that during the sequential insonations that the properties of the microbubbles changed between the exposures, affecting the average per-replicate transfection efficiency and cell detachment at the elevated temperatures.

Temperature-dependent qualities of the cell membrane such as membrane fluidity have been seen to affect sonoporation efficacy as well. In [44], prostate cancer-derived PC-3 cells treated with a heat treatment (44°C, 1-minute equalization) showed a 15-fold increase in the rate of permeability from sonoporation treatment over 37°C. This is in contrast to the effect observed here. The authors attributed the increase in permeability to an increase in membrane fluidity as the effect was similar to lidocaine treatment, a substance known to increase membrane fluidity. The effect of temporal microbubble size and stability in [44] was likely minimal due to the short per-replicate insonations (1 minute).

Lastly, the magnitude and homogeneity of the acoustic field may have been affected at the fixed treatment distance due to a change in the speed of sound of the water bath at higher temperatures. Due to the device's operation in the near-field region, this effect would likely be more pronounced than if the treatment distances were closer to the near-far field transition distance. However, the change in speed of sound due to temperature from 37°C to 42°C is a relatively small change, approximately 0.53% (1524 m/s v. 1532 m/s [64]).

In order to come to a conclusion on the effect of temperature on sonoporation efficacy

on SiHa cells, these many factors must be subject of future study.

3.5 Conclusion

The sonoporation platform was observed to be effective at inducing permeability of SiHa cells at a similar rate to the previous system. The previous system took roughly a half-day to set-up for experiments (3 to 4 hours). During this study, this new system took on the order of a half-hour to 1 hour, dominated mainly on the bath treatment time (heating and degassing). While the operator was not required to manage the acoustic conditions at the start of each experiment day, the management of the general-purpose electrical equipment was still required.

Chapter 4

Power Drivers

4.1 Rationale

The proposed sonoporation device was designed to have six transducers which were to be operated automatically. However, standard lab equipment (waveform generators and amplifiers) typically have a single output. This limits the device to being operated in a sequential manner. In this case, both the operating transducer and the excitation parameters need to be manually switched between insonations by the operator. It would be ideal to have an ultrasound excitation device which could support up to six independently-controlled concurrent excitations. This chapter explores the possibilities for power output stages for such an electrical driver and the design and simulation of this power output stage.

4.2 Design Requirements

The electrical output power required to produce the desired acoustic pressure was previously determined for each transducer at its optimal treatment distance. The maximum observed output power (123 W) served as a basis for designing power drivers for the transducer array. The required output power was taken to be 150 W to provide additional margins for safety, reliability, and flexibility.

A summary of the electrical and acoustic requirements are listed in Table 4.1.

Center operating frequency	1 MHz
Bandwidth	(unspecified)
Output load	50 Ω ($f = 1$ MHz)
Maximum output power	150 W (C.W.)

Table 4.1: Power output stage requirements for ultrasound excitation device.

4.3 Amplifier Topologies

There are many varieties of power amplifiers (also referred to as power inverters) [65–67]. The two types discussed here are current-mode and switch-mode amplifiers. Both of these types of amplifier use transistors to convert a low-power signal into a high-power signal. They differ, however, in their use of transistor(s).

Current-mode amplifier topologies use transistors as controlled current sources [65,67]. These amplifiers are classified based on the portion of the waveform cycle during which the transistor conducts, referred to in general terms as the conduction angle, θ. Class A refer to those amplifiers whose transistors conduct during the entire waveform cycle (*i.e.*, $\theta = 2\pi$), Class B refer to those which conduct during a half the cycle ($\theta = \pi$), and Class C refer to those which conduct during less than half the cycle ($\theta < \pi$). Class AB refers to those amplifiers whose transistors conduct between a half (Class B) and a full (Class A) waveform cycle ($\pi < \theta < 2\pi$) [65, 67].

Switch-mode amplifiers topologies use transistors as switches, either non-conducting (off) or fully conducting (on) [65, 67]. As a consequence, switch-mode amplifiers are classified based on topology and operating principle rather than conduction angle [65]. Class D, for example, refers to an amplifier with transistors which are switched on and off in alternating intervals in order to convert a DC voltage (or current) into a square AC voltage (or current) waveform [65,67]. The harmonic content of this waveform can be filtered by a resonant network at the amplifier output in order to produce a sinusoidal output. Class E is another type of switching amplifier which employs zero-voltage switching (ZVS) and zero-derivative switching (ZDS) conditions [65, 67]. These conditions ensure that the switch voltage and switch current waveforms are non-overlapping, yielding zero power dissipation and zero switching loss in the transistors for a theoretical efficiency of 100% [65,67]. Class DE amplifiers refer to those which combine typical Class D topologies (*e.g.* half-bridge) with Class E ZVS and ZDS conditions to reduce switching and drain power losses [65, 67].

Class A amplifiers can be highly linear, similar to a small signal amplifier, amplifying

Class	Mode	Max. Efficiency	Notes
A	Current-mode	50%	Low distortion $\theta = 2\pi$
B	Current-mode	78.5%	Cross-over distortion $\theta = \pi$
AB	Current-mode	78.5%	$\pi < \theta < 2\pi$
C	Current-mode	50-100%	Non-linear $\theta < \pi$ $\eta_{max} = 100\%, \theta = 0$ $\eta_{max} = 50\%, \theta = \pi$
D	Switch-mode	100%	Inductive load preferred High-side switching
E	Switch-mode	100%	ZVS and ZDS conditions Single switch (low-side)
DE	Switch-mode	100%	ZVS and ZDS conditions High-side switching
F	Switch-mode	100%	Multiple resonators Complex circuit/analysis

Table 4.2: A summary of power output stage (amplifier) classes [65, 67].

an input signal with little distortion [65]. However, Class A suffer from very low practical efficiencies (*e.g.* 40-45% [65]). The input signal of switch-mode amplifiers, on the other hand, are treated as a timing signal rather than a small signal needing to be amplified undistorted [67]. As a result, switch-mode amplifiers have higher practical efficiencies but suffer from non-linearity [65, 67]. A summary of different classes of amplifiers is provided in Table 4.2.

4.4 Candidate Amplifier Topology

Class DE half-bridge topology was considered for this application (Fig. 4.1) [67]. The ultrasound driver to be designed is required to provide a high-power sinusoidal signal of a single frequency. Switch-mode amplifiers are an efficient way to fulfill these requirements. Class DE amplifiers provide lower voltage stresses on the transistors than Class E while providing the same ZVS and ZDS switching conditions. The benefits of Class DE over

the Class E come at the expense of added switching complexity and a high-side N-channel MOSFET which is more difficult to drive [67]. An efficient amplifier reduces the size and cooling requirements, potentially allowing for multiple drivers to be in a smaller device.

While current-mode amplifiers provide better linearity over switch-mode amplifiers, linearity is important for applications such as ultrasound imaging, where a signal needs to be amplified with minimal distortion. Linearity is less important in this application as long as the output power can effectively be controlled.

4.5 Amplifier Design

4.5.1 Design Equations

The design for the Class DE amplifier was adopted from [65] and [67]. The amplifier topology is shown in Fig. 4.1 and the design equations for a 25% duty cycle are summarized in Tables 4.3 and 4.4. A detailed derivation of these equations is available in Appendix A.

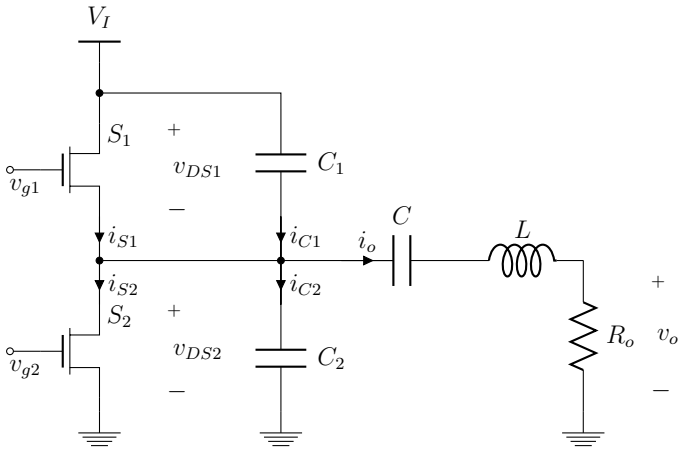

Figure 4.1: Class DE half-bridge power amplifier topology [67].

4.5.2 Output Quality Factor

The quality factor of the output network, Q_L, must be chosen during design to yield practical component values. One of the design requirements was to support pulsed operation, hence, a relatively low Q_L should be chosen to reduce oscillation and additional power

Load resistance	$R_o = \frac{V_I^2}{2\pi^2 P_o}$	(4.1)
Shunt capacitors	$C_m = \frac{1}{2\pi\omega R_o}$	(4.2)
Output inductance	$L = \frac{Q_L R_o}{\omega}$	(4.3)
Output capacitance	$C = \frac{1}{\omega R_o (Q_L - \frac{\pi}{2})}$	(4.4)

Table 4.3: Component value equations for a Class DE half-bridge amplifier, $k = 0.25$ [67].

Maximum drain current	$I_{DM(max)} = I_{m(max)} = \frac{V_m}{R} = \frac{V_I}{\pi R_o}$	(4.5)
Maximum drain-source voltage	$V_{DS(max)} = V_I$	(4.6)
Maximum voltage across series capacitor	$V_{C(max)} = \frac{I_{m(max)}}{\omega C}$	(4.7)
Maximum voltage across series inductor	$V_{L(max)} = \omega L I_{m(max)}$	(4.8)

Table 4.4: Device stress equations for a Class DE half-bridge amplifier, $k = 0.25$ [67].

being transferred to the load after each pulse. However, the ability for the output network to filter higher harmonics decreases (*i.e.* the bandwidth increases) with decreasing quality factor as given by

$$Q_L = \frac{f_c}{\Delta f} \tag{4.9}$$

where Δf is the bandwidth of the output network and f_c is its resonant frequency [52]. As Q_L decreases, the shape of the output current waveform becomes less sinusoidal and more exponential, increasing the total harmonic distortion (THD) [67]. Therefore, the choice of Q_L was made qualitatively and iteratively during simulation as a trade-off between damping oscillations and the resulting harmonic power, with transient damping taking precedence.

4.5.3 Output Impedance Transformation

The switching frequency, output power, and output load resistance have been given to be 1 MHz, 150 W, and 50 Ω respectively. However, using these values with the design equations in Table 4.3 may not necessarily yield a practical solution. For example, the

DC supply voltage becomes 384.7 VDC using (4.1) and the requirements above. Instead, the DC supply voltage was made a design parameter, yielding an output load resistance different from that of 50 Ω. From this, an impedance transformation can be applied to the output RLC network such that a 50 Ω load appears as the calculated design load, R_o [52, 65, 67].

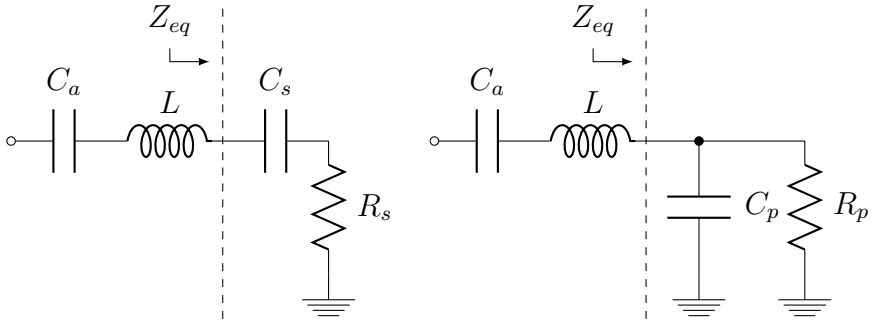

Figure 4.2: Downward split-capacitor impedance transformation. The impedance (Z_{eq}) for the sections containing C_s-R_s and C_p-R_p can be made equal for a given frequency ($R_p > R_s$).

For example, a split-capacitor downward impedance transformation can be applied [67]. Here, one can take the series capacitor C and split it in two series capacitances C_a and C_s (Fig. 4.2). Equating the impedances of the resulting series C_s-R_s section to a parallel C_p-R_p combination yields expressions which can be used to transform the desired load resistance $R_p = 50\ \Omega$ into the resultant design load resistance $R_o = R_s$ at the center operating frequency:

$$Z_s = Z_p \tag{4.10}$$

$$R_s + jX_{Cs} = \frac{R_p(jX_{Cp})}{R_p + jX_{Cp}} \tag{4.11}$$

$$R_s + jX_{Cs} = \frac{R_p(jX_{Cp})}{R_p + jX_{Cp}} \left(\frac{R_p - jX_{Cp}}{R_p - jX_{Cp}}\right) \tag{4.12}$$

$$R_s + jX_{Cs} = \frac{R_p X_{Cp}^2}{R_p^2 + X_{Cp}^2} + j\frac{R_p^2 X_{Cp}}{R_p^2 + X_{Cp}^2}\ . \tag{4.13}$$

If the "quality" of the series and parallel RC combinations is defined as

$$q = \frac{X_{Cs}}{R_s} = \frac{R_p}{X_{Cp}} \tag{4.14}$$

then the real and imaginary parts of (4.13) simplify to

$$R_s = \frac{R_p}{1 + \left(\frac{R_p}{X_{Cp}}\right)^2} = \frac{R_p}{1 + q^2} \tag{4.15}$$

and

$$X_{Cs} = \frac{X_{Cp}}{1 + \left(\frac{X_{Cp}}{R_p}\right)^2} = \frac{X_{Cp}}{1 + q^{-2}} \ . \tag{4.16}$$

The value of q can also described in terms of R_s and R_p by rearranging (4.15):

$$q = \sqrt{\frac{R_p}{R_s} - 1} \ . \tag{4.17}$$

Note that for q to be a real, $R_p > R_s$. Additionally, given a desired R_p and a design value of R_s, the ratio ${}^{R_p}/_{R_s}$ is defined and, hence, q is defined.

The series capacitance C_a can be determined from (4.14):

$$\frac{1}{C_a} = \frac{1}{C} - \frac{1}{C_s} \tag{4.18}$$

$$\frac{1}{C_a} = \omega R_s \left(Q_L - \frac{\pi}{2}\right) - q\omega R_s \tag{4.19}$$

$$\frac{1}{C_a} = \omega R_s \left(Q_L - q - \frac{\pi}{2}\right) \tag{4.20}$$

$$C_a = \frac{1}{\omega R_s \left(Q_L - q - \frac{\pi}{2}\right)} \tag{4.21}$$

Note that the defined value for q raises the minimum design value of Q_L.

Since the impedance of the parallel C_p-R_p combination is equal to that of the series C_s-R_s combination, the voltage across both are equal for the same output current i_o:

$$v_{Rp} = i_o Z_s \tag{4.22}$$

The voltage and current stresses in the parallel network can be found using the output peak current $I_{m(max)}$:

$$V_{Rp(max)} = I_{m(max)} |Z_s| \tag{4.23}$$

$$I_{Rp(max)} = \frac{V_{Rp(max)}}{R_p} \tag{4.24}$$

$$I_{Cp(max)} = \frac{V_{Rp(max)}}{|X_{Cp}|} \tag{4.25}$$

4.5.4 Analysis

Let $P_o = 150$ W, $V_I = 96$ V, $f = 1$ MHz, $R_p = 50\ \Omega$, and $Q_L = 8$.

Component Values

$$R_s = \frac{V_I^2}{2\pi^2 P_o} = \frac{(96\text{ V})^2}{2\pi^2(150\text{ W})} = 3.11\ \Omega \tag{4.26}$$

$$C_m = \frac{1}{2\pi\omega R_s} = \frac{1}{2\pi(2\pi(1\text{ MHz}))(3.11\ \Omega)} = 8.14\text{ nF} \tag{4.27}$$

$$L = \frac{Q_L R_s}{\omega} = \frac{8(3.11\ \Omega)}{2\pi(1\text{ MHz})} = 3.96\ \mu\text{H} \tag{4.28}$$

$$q = \sqrt{\frac{R_p}{R_s} - 1} = \sqrt{\frac{50\ \Omega}{3.11\ \Omega} - 1} = 3.88 \tag{4.29}$$

$$C_p = \frac{q}{\omega R_p} = \frac{3.88}{2\pi(1\text{ MHz})(50\ \Omega)} = 12.4\text{ nF} \tag{4.30}$$

$$\begin{aligned} C_a &= \frac{1}{\omega R_s(Q_L - q - \frac{\pi}{2})} \\ &= \frac{1}{(2\pi(1\text{ MHz}))(3.11\ \Omega)(8 - 3.88 - \frac{\pi}{2})} = 20.1\text{ nF} \end{aligned} \tag{4.31}$$

$$C_s = \frac{1}{q\omega R_s} = \frac{1}{3.88(2\pi(1\text{ MHz}))(3.11\ \Omega)} = 13.2\text{ nF} \tag{4.32}$$

Device Stresses

$$I_{DM(max)} = I_{m(max)} = \frac{V_I}{\pi R_s} = \frac{96\text{ V}}{\pi(3.11\ \Omega)} = 9.82\text{ A} \tag{4.33}$$

$$V_{DS(max)} = V_I = 96 \text{ V} \tag{4.34}$$

$$V_{Ca(max)} = \frac{I_{m(max)}}{\omega C_a} = \frac{9.82 \text{ A}}{2\pi(1 \text{ MHz})(20.1 \text{ nF})} = 77.8 \text{ V} \tag{4.35}$$

$$V_{L(max)} = \omega L I_{m(max)} = 2\pi(1 \text{ MHz})(3.96 \ \mu\text{H})(9.82 \text{ A}) = 244 \text{ V} \tag{4.36}$$

$$\begin{aligned} V_{Rp(max)} &= I_{m(max)} \sqrt{{R_s}^2 + \left(\frac{1}{\omega C_s}\right)^2} \\ &= (9.82 \text{ A}) \sqrt{(3.11 \ \Omega)^2 + \left[\frac{1}{2\pi(1 \text{ MHz})(13.2 \text{ nF})}\right]^2} \\ &= 122 \text{ V} \end{aligned} \tag{4.37}$$

$$I_{Rp(max)} = \frac{V_{Rp(max)}}{R_p} = \frac{122 \text{ V}}{50 \ \Omega} = 2.44 \text{ A} \tag{4.38}$$

$$\begin{aligned} I_{Cp(max)} &= \frac{V_{Rp(max)}}{X_{Cp}} \\ &= V_{Rp(max)}(\omega C_p) \\ &= (122 \text{ V})\,(2\pi(1 \text{ MHz})(12.4 \text{ nF})) \\ &= 9.51 \text{ A} \end{aligned} \tag{4.39}$$

4.6 Simulation

4.6.1 Components and SPICE Models

The amplifier was simulated using `LTSpice` (v4.20h; Linear Technology Corporation). Some component models were chosen for the simulation at this stage based on the re-

quirements and analytically determined maximum stresses above.

Switching Components

IRFB5620 (International Rectifier) N-channel MOSFETs were chosen for the switching components. These MOSFETs are rated for a maximum drain-source voltage of 200 V, much higher than the maximum computed stress $V_{DS(max)} = V_I = 96$ V. The output capacitance of the MOSFETs (C_o) limit the maximum switching frequency of the amplifier [67]. The output capacitance is determined by

$$C_o = C_{DS} = C_{OSS} - C_{RSS} \tag{4.40}$$

where C_{DS} is the drain-source (output) capacitance, and C_{OSS} and C_{RSS} are values provided by the manufacturer [66]. For the IRFB5620, $C_o = C_{DS} \approx 108$ pF, thus, the maximum switching frequency is

$$f_{max} = \frac{1}{4\pi^2 R_s C_o} = \frac{1}{4\pi^2 (3.11\Omega)(108 \text{ pF})} = 75.4 \text{ MHz} . \tag{4.41}$$

This frequency is well above the operating frequency, $f = 1$ MHz.

The rated continuous drain current is 25 A at 25 °C and 18 A at 100 °C, well above $I_{DM(max)} = 9.8$ A. The reverse-diode current rating is 25 A, or 100 A for short pulses (the width depending on the junction temperature).

This MOSFET appears to be within the specifications for the amplifier. The SPICE model for this MOSFET was provided by the manufacturer and used for simulation.

Gate Drivers

SPICE voltage sources were used to simulate gate drivers. These voltage sources were set-up to deliver a "square" waveform at 1 MHz with 20 ns rise and fall times. These drivers were given output resistances of 100 mΩ.

Passive Components

Passive components were simulated using the default SPICE models. The reactive components were given equivalent series resistances of 100 mΩ, an estimate for ceramic capacitors and hand-wound inductors.

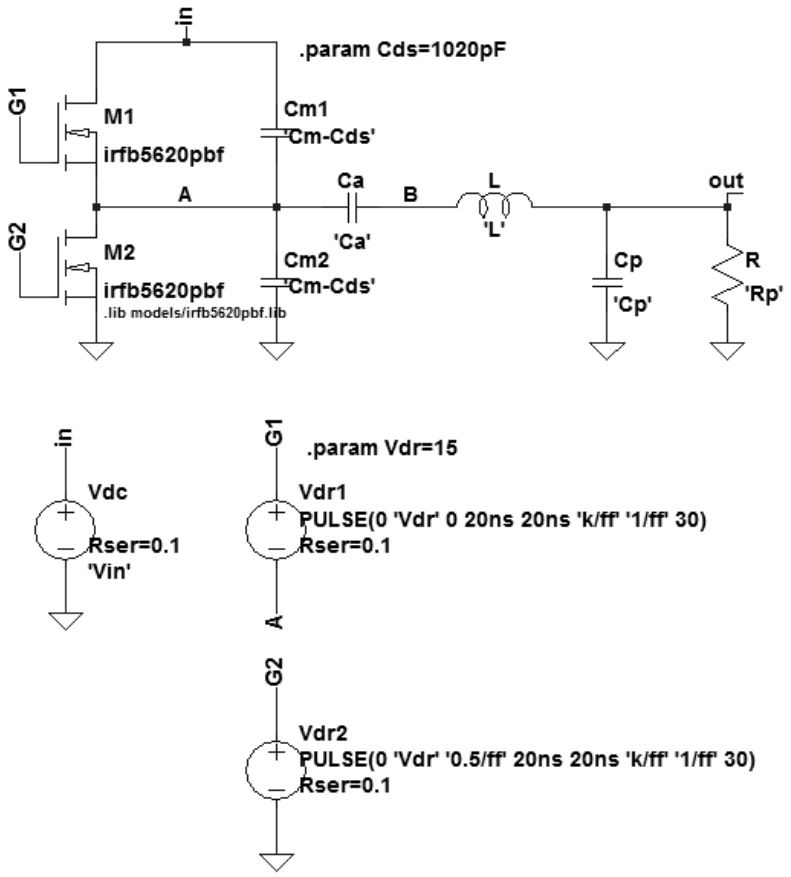

Figure 4.3: `LTSpice` schematic for the Class DE amplifier with a 50 Ω resistive load: $f = 1$ MHz, $P_o = 150$ W, and $Q_L = 8$.

DC Supply

The DC supply voltage was simulated using a SPICE constant voltage source. The output resistance of the source was 100 mΩ, lower than the input resistance of the amplifier, in order to produce a relatively constant supply voltage $V_I = 96$ V during the simulation.

4.6.2 Measurements

Initial simulations were performed using a resistive 50 Ω load (Fig. 4.3). The pulsed operation of the device (30 cycles at 1 MHz) was used to evaluate the transient behaviour at the beginning and end of the pulse. The average input power, output power, drain power, and gate (drive) power, drain efficiency, efficiency, power-added efficiency, gate drive gain, and total harmonic distortion were each determined over 10 cycles in the

centre of the pulse as an estimate of their steady-state values. The maximum time step was set to 10 ns and the operation was simulated for 100 μs.

4.6.3 Adjustments

The MOSFET output capacitance was subtracted from the ideal switch shunt capacitors C_m. While the datasheet provided a value for this capacitance, an alternative value of $C_o = 1.02$ nF was found by trail and error. The value of this capacitance was adjusted in order to minimize the drain-source voltage and resultant spike in drain current at the moment of switch-on (Fig. 4.4b). (That is to say, equivalently, that the design value C_m was reduced to produce the desired effect.) As a result, the drain-source shunt capacitances values became $C_m = 8.14$ nF $- 1.02$ nF $= 7.12$ nF. The large spikes in current (of nearly 100 A) still remain at the beginning of the pulse due to the non-zero DC voltage across the transistors during the transient start-up from rest. Taking $C_o = 1.02$ nF reduces the maximum switching frequency of the amplifier to 7.99 MHz, still well above the 1 MHz design switching frequency.

4.6.4 Results

The results of the transient simulation of the circuit in Fig. 4.3 are summarized in Table 4.5. The average output power was 139 W, lower than the anticipated design value of 150 W. The average input DC power was 149 W. The average drain powers were 800 mW for both MOSFETs. Thus, the drain efficiency, given by

$$\eta_D = \left(1 - \frac{P_{D1} + P_{D2}}{P_o}\right) \tag{4.42}$$

was 98.9% for the measured interval. The average gate drive power was 371 mW and 372 mW for M_1 and M_2 respectively. The power gain, given by

$$G_{dB} = 10\ \log_{10}\left(\frac{P_o}{P_{G1} + P_{G2}}\right) \tag{4.43}$$

was 22.7 dB. The amplifier efficiency given by

$$\eta = \frac{P_o}{P_I} \tag{4.44}$$

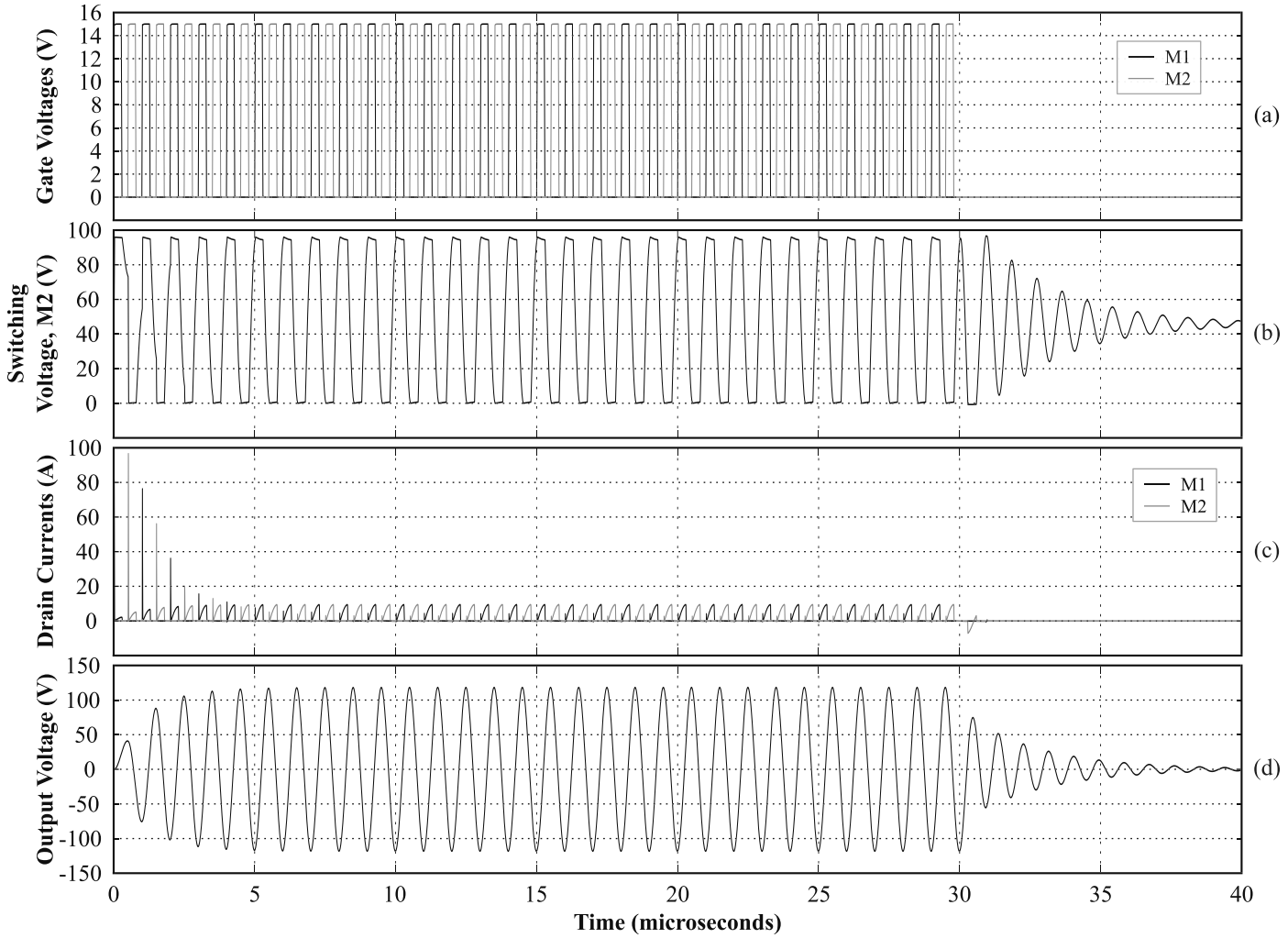

Figure 4.4: Resulting waveforms for the first 40 μs of `LTSpice` simulation using a resistive 50 Ω load: (a) gate drive timing waveform ($V_{GS(1,2)} = 15$ V, $k = 0.25$); (b) drain-source voltage of M_2; (c) drain currents for M_1 (black) and M_2 (grey); (d) the resulting output voltage waveform.

was 89.8% and the power added efficiency, which accounts for the input gate drive power, given by

$$\mathrm{PAE} = \frac{\mathrm{P_o} - (\mathrm{P_{G1}} + \mathrm{P_{G2}})}{\mathrm{P_I}} \tag{4.45}$$

was 89.3%.

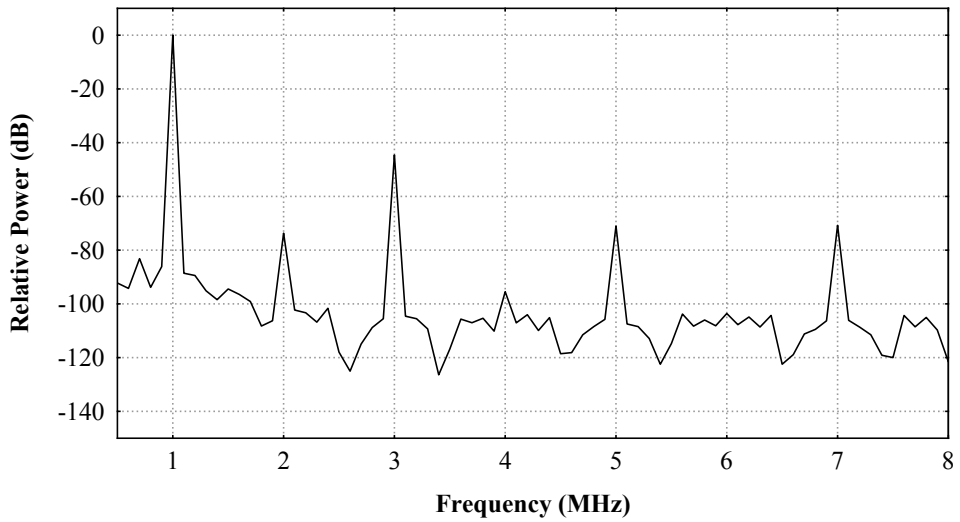

Figure 4.5: The relative power (dB) of the frequency components of the output voltage waveform with a resistive 50 Ω load (f_c = 1 MHz). The power of the 3rd and 5th harmonics are -43.2 dB and -71.0 dB respectively.

The total harmonic distortion (THD) of the output voltage over this interval was 33.7%. The 3rd and 5th harmonic powers were -43.2 dB and -71.0 dB respectively (Fig 4.5). A DC component of 3.10 μV was present as well. The THD of the output voltage could be improved by increasing the quality factor of the output RLC network (Q_L) at the expense of slower transients at the start and end of the pulse.

Transients

Ideally, transients at the start and end of the pulse would not exist for a pulsed application. This would allow the device to deliver a exact number of cycles per pulse. However, due to the use of reactive components and the high quality factor of the output filter (under-damped), transients will be present. The resulting output voltage waveform for a single pulse is plotted in Fig. 4.4d. At the start of the pulse, the envelope of the output voltage takes less than one cycle to reach 63.2% of the maximum of 118.8 V (*i.e.,* the rise time)

and about 6-7 cycles to reach the maximum. At the end of the pulse, the envelope of the output voltage takes about 3-4 cycles to fall below 37.8% of the maximum (*i.e.,* the fall time) and about 18 cycles to fall below 0.1%.

These transient periods are relatively small with respect to the duty cycle. The rise time is less than 3.33% of the pulse length (30 μs) and the fall time is less than 0.68% of the dead time (595 μs).

4.7 Transducer Electrical Model

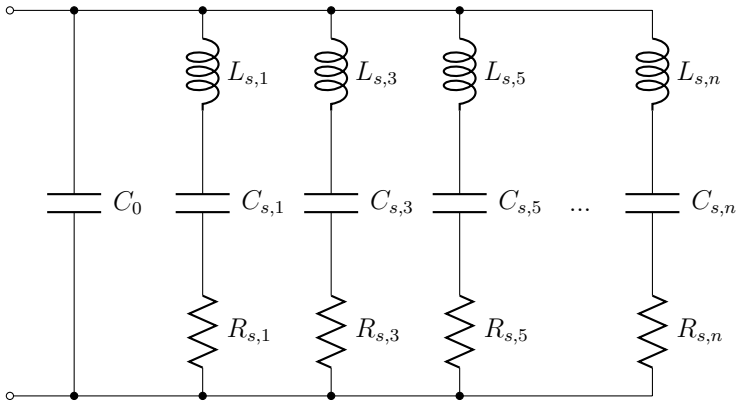

Figure 4.6: Butterworth-Van Dyke electrical model of a piezoelectric transducer.

The simulations in the previous section were repeated, replacing the resistive 50 Ω load with a model of the transducer. The model used here was the Butterworth-Van Dyke (BvD) model (Fig. 4.6) [47, 68, 69]. This model is comprised of an electrical capacitance (C_0) in parallel with multiple series resonant branches. Each series resonant branch models the mechanical oscillation of the piezoelectric element at each odd harmonic. A series resonant frequency ($\omega_{s,n} = 2\pi f_{s,n}$) and a parallel (anti-)resonant frequency ($\omega_{p,n} = 2\pi f_{p,n}$) exists for each branch, n. At $f_{s,n}$, the series branch inductance and capacitance cancel out, leaving the series branch resistance ($R_{s,n}$) in parallel with the static capacitance (C_0). The frequency, $f_{s,n}$ can be found when the real part of the measured admittance is at local maximum (Fig. 4.7) [47]. Similarly, at $f_{p,n}$, the real part of the impedance is at local maximum [47]. The model values can be determined using the following equations

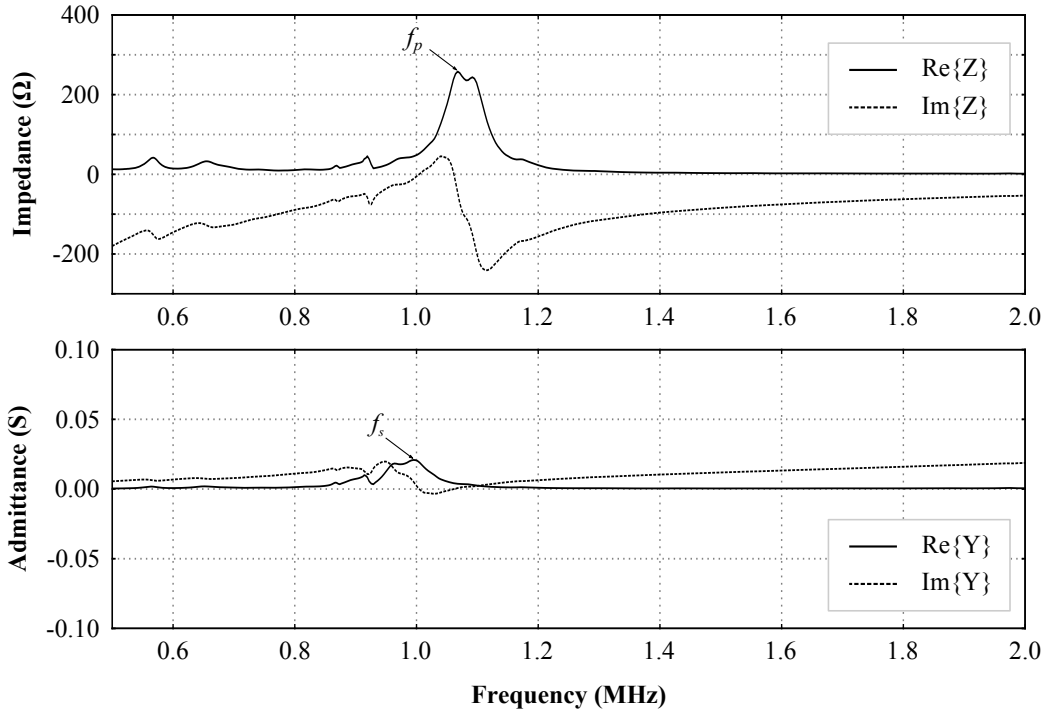

Figure 4.7: The measured impedance (top) and admittance (bottom) for a transducer from 0.5 MHz to 2 MHz. The series resonant frequency f_s occurs on this range where the real part of the admittance is at a maximum. The parallel (anti-)resonant frequency f_p where the real part of the impedance is at a maximum. Here, $f_s \approx 0.995$ MHz and $f_p \approx 1.09$ MHz.

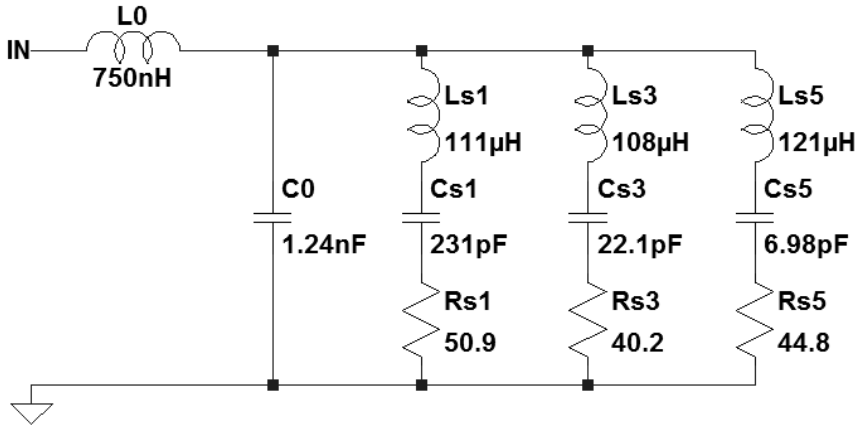

Figure 4.8: The resultant Butterworth-Van Dyke model with input inductance and component values determined up to the 5$^{\text{th}}$ harmonic.

[47, 68, 69]:

$$C_0 = \frac{\mathbb{I}\text{m}\{\text{Y}_{\text{s,n}}\}}{\omega_{s,n}} \tag{4.46}$$

$$R_{s,n} = \frac{1}{\mathbb{R}\text{e}\{\text{Y}_{\text{s,n}}\}} \tag{4.47}$$

$$C_{s,n} = C_0 \left[\left(\frac{f_{p,n}}{f_{s,n}} \right) - 1 \right] \tag{4.48}$$

$$L_{s,n} = \frac{1}{\omega_{s,n}^2 C_{s,n}} \tag{4.49}$$

where $R_{s,n}$, $C_{s,n}$ and $L_{s,n}$ are the series resonant branch resistance, capacitance, and inductance respectively, and $Y_{s,n}$ is the total admittance of the model at the series resonant frequency of the n^{th} branch ($\omega_{s,n} = 2\pi f_{s,n}$). Upon identifying $f_{s,1}$, $f_{p,1}$ and $Y_{s,1}$, C_0 can be calculated from (4.46). The values $R_{s,1}$, $C_{s,1}$, and $L_{s,1}$ can be determined once C_0 is found using (4.47), (4.48), and (4.49). For additional branches, the same value for C_0 can be used, however, $f_{s,n}$, $f_{p,n}$ and their corresponding impedances will differ.

4.7.1 Measurements and Computations

Model Modifications

Values for the electrical model were computed from impedance measurements made for one of the six transducers in a water bath at a temperature of 37°C. The measurements were

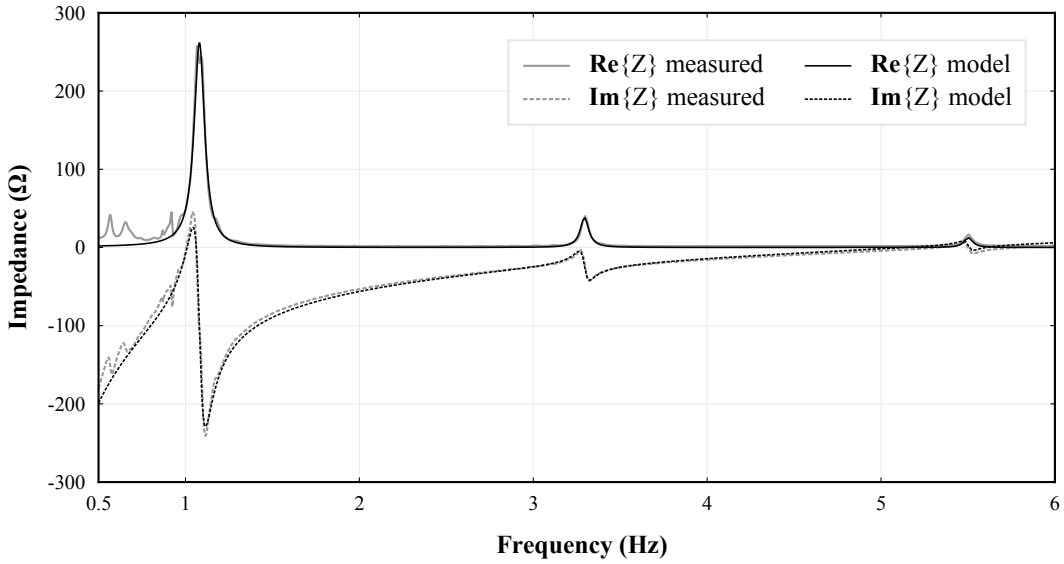

Figure 4.9: The impedance of the model (thin, black) against the measured impedance (thick, grey) showing good agreement over 0.5 MHz to 6 MHz.

made using an Agilent E5071C network analyser (Agilent Technologies Canada Inc., Mississauga, ON, Canada). The measured impedance included that of the cable in addition to the piezoelectric element. In order to fit the BvD model to the measured impedance, the cable was modelled as an inductive impedance in series with the BvD model and was subtracted from the measured values prior to computing the model.

The value of the input inductance was iteratively adjusted to achieve the best fit to the measured data at high frequencies. The optimal input inductance was found to be 750 nH. The modified model and its values are shown in Fig. 4.8. The impedance of the model is plotted against the measured impedance in Fig. 4.9.

Matching Circuit

In practice, the transducers are electrically matched to 50 Ω at 1 MHz using an L-type (2-element) matching network. The impedance of the transducer model at 1 MHz was $Z = 48.2 - j8.57\ \Omega$. A low-pass L-type matching network was computed and added to the simulation.

From Section 2.5, the condition for matching is

$$Z_A^* = Z_1 + Z_2 \| Z_B \tag{4.50}$$

$$R_A - jX_A = jX_1 + \left(jB_2 + \frac{1}{R_B + jX_B} \right)^{-1} \tag{4.51}$$

and, by letting $X = X_1 + X_A$, the solution for X and B_2 is

$$B_2 = \frac{X_B}{|Z_B|^2} \pm \sqrt{\frac{R_B}{R_A}} \frac{\sqrt{|Z_B|^2 - R_A R_B}}{|Z_B|^2} \tag{4.52}$$

$$X = X_1 + X_A = \frac{1}{B_2} + \frac{R_A}{R_B} \left(X_B - \frac{1}{B_2} \right) \ . \tag{4.53}$$

For the transducer model impedance $Z_A = 48.2 - j8.57\ \Omega$ and a source impedance $Z_B = 50\ \Omega$,

$$\begin{aligned} B_2 &= \frac{0\ \Omega}{(50\ \Omega)^2} \pm \sqrt{\frac{50\ \Omega}{48.2\ \Omega}} \frac{\sqrt{(50\ \Omega)^2 - (50\ \Omega)(48.2\ \Omega)}}{(50\ \Omega)^2} \\ &= \{-0.00386, +0.00386\}\ \text{S} \end{aligned} \tag{4.54}$$

and

$$\begin{aligned} X_1 = X - X_A &= \pm \frac{1}{0.00386}\ \Omega + \frac{48.2\ \Omega}{50\ \Omega} \left(0\ \Omega \mp \frac{1}{0.00386}\ \Omega \right) - (-8.57\ \Omega) \\ &= \{-0.756, 17.9\}\ \Omega \ . \end{aligned} \tag{4.55}$$

Choosing $B_2 = +0.00386$ S (and correspondingly $X_1 = 17.9\ \Omega$), the component values for the matching circuit become

$$L = \frac{X_1}{\omega} = \frac{17.9\ \Omega}{2\pi(1\ \text{MHz})} = 2.85\ \mu\text{H} \tag{4.56}$$

and

$$C = \frac{B_2}{\omega} = \frac{0.00386\ \text{S}}{2\pi(1\ \text{MHz})} = 615\ \text{pF} \ . \tag{4.57}$$

4.7.2 Simulation

The modified `LTSpice` circuit is shown in Fig. 4.10. This circuit differs from the resistive case (Fig. 4.3) only in that the 50 Ω resistive load is replaced with a two-element matching circuit and a BvD model subcircuit component. The simulation parameters were otherwise

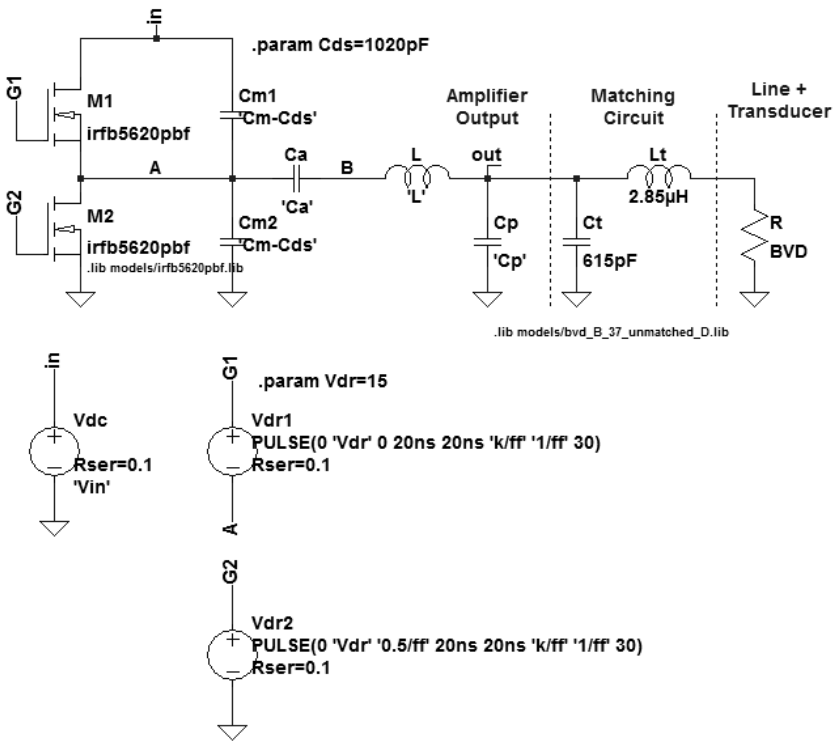

Figure 4.10: `LTSpice` schematic for Class DE amplifier with transducer model and L-type, low-pass matching circuit.

identical to the resistive case described above.

4.7.3 Results

The results of the transient simulations using the BvD model are summarized in Table 4.5. The average output power was 134 W, about 5 W lower than the resistive case. The average input DC power remained 149 W. Hence, the overall efficiency was 89.5%, a drop of 0.3% over the resistive case. The average drain powers were 805 mW and 810 mW for M_1 and M_2 respectively, a 5-10 mW increase over the resistive case. Nevertheless, the drain efficiency remained at 98.8%. The average gate drive powers were 363 mW and 364 mW for M_1 and M_2 respectively. The resultant gain was 22.6 dB, a drop of 0.1 dB over the resistive case. The power added efficiency was 89.0%, a drop in 0.3%.

The THD due to the transducer model was slightly better at 27.9%, a decrease of 5.8% over the resistive case. The third and fifth harmonic powers were -43.2 dB (an increase of 1.4 dB) and -71.7 dB (a decrease of 0.9 dB) respectively (Fig. 4.11). A DC component of -160 mV was present as well.

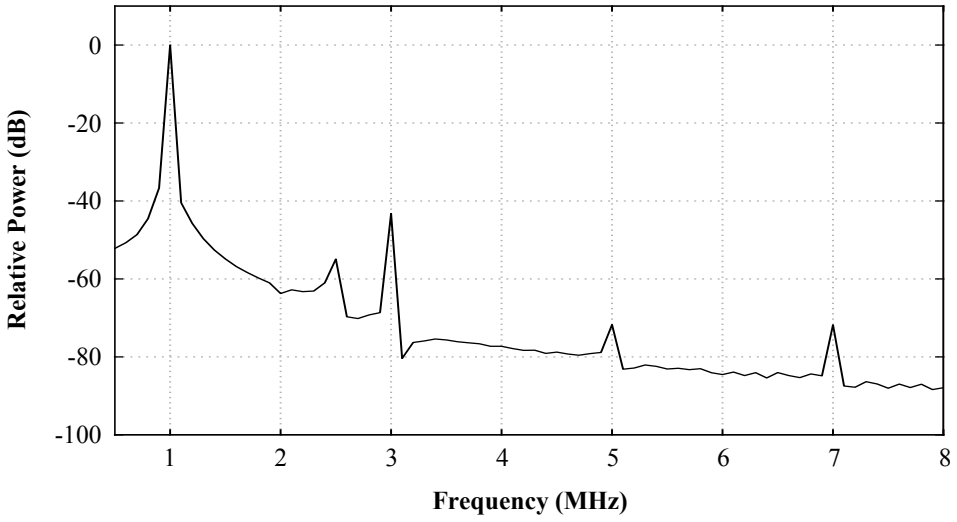

Figure 4.11: The relative power (dB) of the frequency components of the output voltage waveform using the transducer model (f_c = 1 MHz). The power of the 3rd and 5th harmonics are -43.2 dB and -71.7 dB respectively.

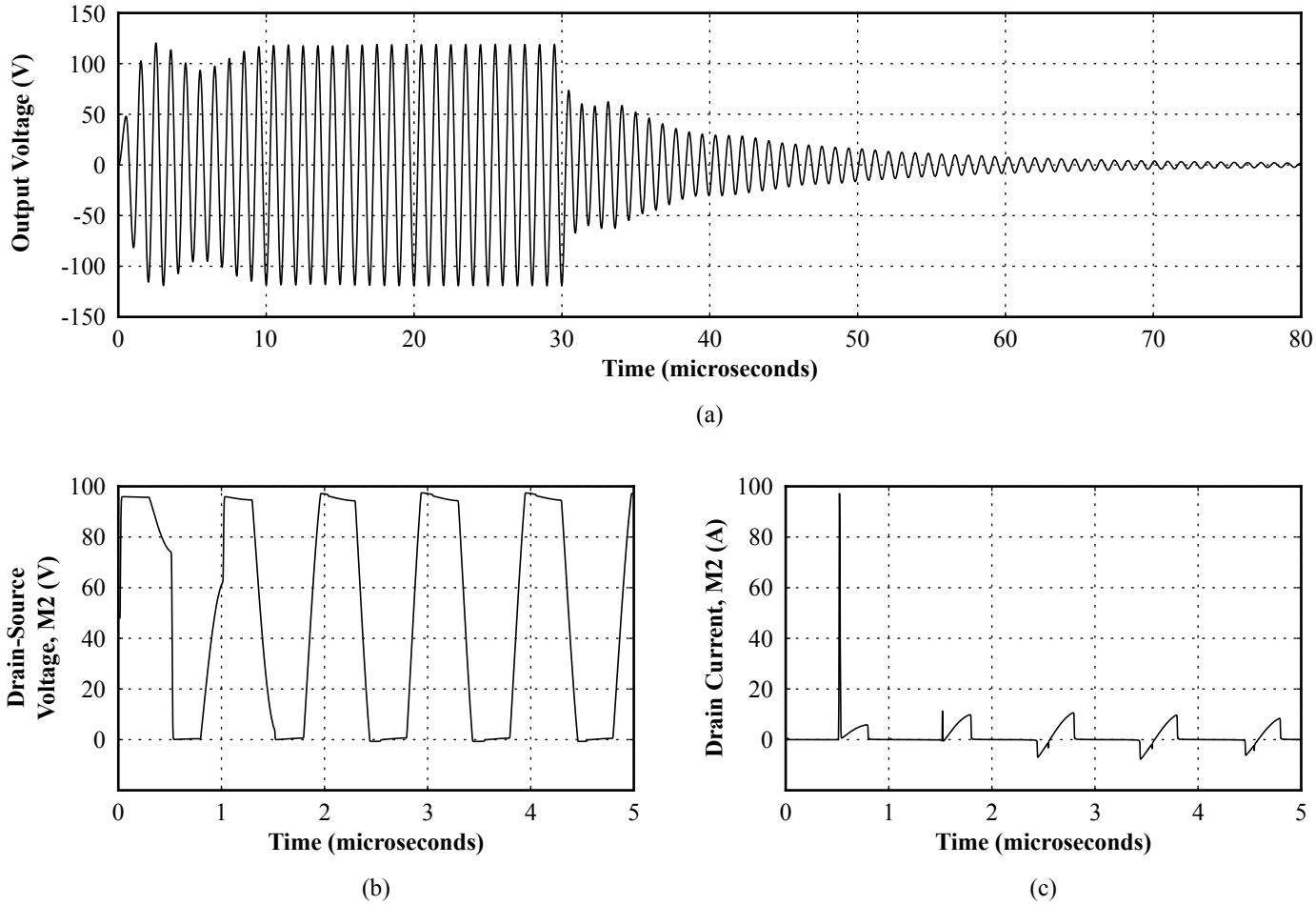

Figure 4.12: (a) The first 80 μs of the resulting output voltage waveform showing ringing lasting for more than 20 cycles after excitation halted (at 30 μs). (b) The drain-source voltage for the lower switching device (M_2) showing the switching conditions for the first 5 μs of the simulation. (c) The drain current for the lower switching device (M_2) showing large, short current spikes for the first 2 cycles and reverse current corresponding to negative drain-source voltages in (b).

Quantity		50 Ω	BvD	Δ_{abs}	Δ_{rel}
Input power (P_I)	-	149 W	149 W	0 W	±0%
Output power (P_o)	-	139 W	134 W	-5 W	-3.60%
Gate drive power (P_G)	M_1	371 mW	363 mW	-8 mW	-2.15%
	M_2	372 mW	364 mW	-8 mW	-2.15%
Drain power (P_D)	M_1	800 mW	805 mW	+5 mW	+0.625%
	M_2	800 mW	810 mW	+10 mW	+1.25%
Gate power gain (G_{dB})	-	22.7 dB	22.6 dB	-0.1 dB	-1.43%
Drain efficiency (η_D)	-	98.9%	98.8%	-0.1%	-0.101%
Efficiency (η)	-	89.8%	89.5%	-0.3%	-0.334%
Power-added efficiency (PAE)	-	89.3%	89.0%	-0.3%	-0.336 %
Total harmonic distortion	-	33.7%	27.9%	-5.8%	-17.2%
	DC	3.10 μV	-0.16 V	$\sim$ -0.16 V	5.16×10^6%
	3^{rd} harmonic	-44.6 dB	-43.2 dB	+1.4 dB	+3.14%
	5^{th} harmonic	-70.8 dB	-71.7 dB	-0.9 dB	-1.27%
Pulse rise-time	63.2%	1 cycles	2 cycles	+1 cycle	+100%
Pulse fall-time	37.8%	4 cycles	8 cycles	+4 cycles	+100%
	0.1%	19 cycles	86 cycles	+67 cycles	+352%

Table 4.5: `LTSpice` simulation results showing measured quantities for the 50 Ω case, the transducer model (BvD) case, and the absolute and relative changes when using the transducer model.

The transients at the output at the start and end of the pulse differed greatly from those in the resistive case (Fig. 4.12). The start-up transient was much less damped. The first peak of the output voltage occurs after 2 cycles but swings back down below 100 V on the 5^{th} cycle before rising again (Fig. 4.12a). The fall time after the pulse extends well beyond that of the resistive case. The envelope of the waveform falls below 37.7% after approximately 7-8 cycles, compared to 3-4 in the resistive case.

4.7.4 Discussion

Transducer Damping

The quality factor of the transducer model is fairly high. For example, the quality factor of the fundamental branch is

$$Q_{s,1} = \frac{X_{Ls,1}}{R_{s,1}} = \frac{\omega_{s,1} L_{s,1}}{R_{s,1}} = \frac{2\pi(0.995 \text{ MHz})(111\mu\text{H})}{50.9\ \Omega} = 13.6\ . \tag{4.58}$$

The Q of this branch is much higher than that of the output network of the amplifier ($Q = 8$). Thus, between the two, the one with the larger Q (*i.e.,* the transducer) will dictate how long the voltage will oscillate after each pulse [52]. If the amount of ringing is satisfactory, then it is possible to redesign the amplifier with an output network with a quality factor closer to that of the transducer without it affecting too much the output waveform, possibly improving the THD. If not, it may be necessary to provide damping to the piezoelectric crystal. This can be done either by adding a backing or matching layer into the transducer design, which will dampen the mechanical oscillation, or by electrically loading the piezoelectric element [47, 48]. Both may be worth exploring as an option in the future.

Switching Conditions

The voltages across the switching components were affected by the use of the BvD model over the 50 Ω resistive load. Like the resistive case, the drain-source voltage across the lower switching component was high at the beginning of the pulse due to the rest state of the amplifier at the start of the pulse, but nears zero after only a few cycles (Fig. 4.10b). However, unlike the resistive case, a negative drain current develops for the low-side MOSFET after only a few cycles, just prior to the turn-on of the device (Fig. 4.10c). This negative current may be due to the body diode of the MOSFET is turning on as the voltage at the input of the RLC resonant network (*i.e.,* the drain-source voltage) may be

dropping below 0 V (Fig. 4.12b). While this diode clamps the voltage at one diode drop below 0 V, the large reverse current may shorten the life of the switching component. In the resistive case, the values for the shunt capacitors were adjusted to minimize the spike in current at turn-on of the MOSFETs. It may be possible to reduce the negative drain current at turn-on in the same manner. Other tuning strategies are available for Class DE amplifiers as well, one of which controls the phase of the output voltage and current waveforms by adjusting the output RLC network and duty cycle [65, 69].

Chapter 5

Future Work

The goal of this project was to build a system to reduce the time and expertise required to perform sonoporation on adherent cells in monolayer. In addition to platform (Chapter 2) and the power driver (Chapter 4), the vision for this system included driving circuitry, output power control, water treatment, and experimental control. Hence, there remain a number of components of the system that can be considered for future work.

5.1 Power Control

The next stages of work for the power driver are the design of the input DC power and power control circuitry (Fig. 5.1). In order to expose cells at a given pressure, the electrical power delivered to each transducer needs to be controlled. The electrical output power of the Class DE drivers can be controlled directly by controlling the DC supply

Name	Typ. Power	Notes
Buck	<100 W	Regulator
Boost	<100 W	Regulator
Buck-boost	<100 W	Regulator
Flyback	100-200 W	Converter; transformer
Forward	100-200 W	Converter; transformer
Half-bridge	200-400 W	Converter; complex switching
Full-bridge	>400 W	Converter; complex switching

Table 5.1: A summary of DC-DC converter topologies [70].

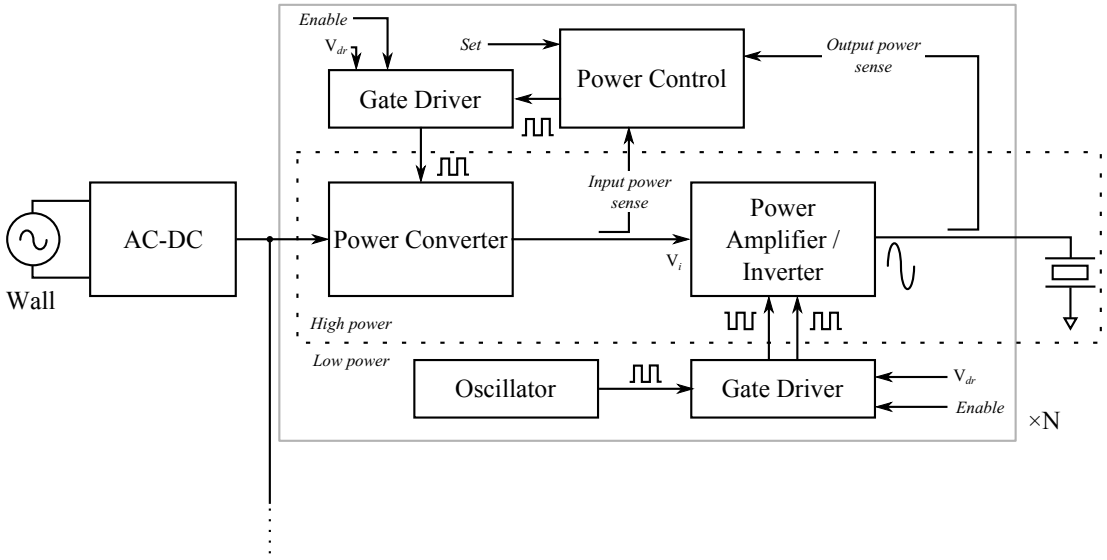

Figure 5.1: A block diagram illustrating an ultrasound power driver, including the power supply and power control configuration.

voltage [67] as given by:

$$P_o = \frac{V_I^2}{2\pi^2 R_o} \ . \tag{5.1}$$

To control the DC supply voltage, it will be necessary to design and build a power regulator, such as a DC-DC power converter [71–73]. It may be sufficient to monitor and control the DC supply voltage, thereby affecting the output power, rather than monitoring and controlling the output power directly. However, the required DC supply voltage to get a desired output power needs to be calibrated at some time before experiments, requiring a sense of the output power. A brief summary of possible DC-DC regulators and converters was compiled from [70] and is available in Table 5.1.

5.2 Experimental Control

An experimental controller can be made to provide an easy-to-use user interface to the system for setting up experimental parameters, automate as much of the experiment and set-up as possible by communicating with the different system components, log experimental parameters and error messages, and display information, warnings, or errors to the user.

The experimental parameters that are not strictly fixed (but may have hardware limits) are bath temperature, pulse duration, pulse repetition frequency, and output electrical power. These parameters could potentially be configured by the user in a well-integrated system. Additionally, acoustic parameters can potentially be specified on a per-transducer basis if, for example, the user wanted to expose different sections of the cell culture to different acoustic parameters. This operation would have the benefit of allowing one to produce multiple biological replicates under a variety of acoustic conditions rather than multiple "pseudo-replicates" exposed under a single set of conditions, while maintaining the same material requirements.

The most hardware-dependent parameter of the system is the ultrasound operating frequency. The piezoelectric elements of the transducers were cut for a specific operating frequency. To change the operating frequency, the transducers may need to be redesigned with different piezoelectric elements or may be driven at their odd harmonics. The amplifier and matching circuits were designed to both operate at a single switching frequency and the output of the amplifier is designed to minimize much of the harmonic content of the output. Thus, to change the operating frequency of the system would require repeating much of the work presented here, for the new frequency, or designing broadband electrical components.

5.3 Water Treatment

Water treatment, such as degassing and heating, could be integrated into the experimental control or left as separate systems. Commercial degassing options include Liqui-Cel (Membrana-Charlotte, Charlotte, NC, USA) and PermSelect (PermSelect, Ann Arbor, MI, USA). Commercial bath-heating options are available as well, including those available from PolyScience (PolyScience, Niles, IL, USA).

5.4 Transducer Damping for Pulsed Operation

The quality factor of the transducer model at 1 MHz was fairly high (13.6). This poses a problem when operating pulsed mode [48] since the transducer will continue to oscillate after excitation, affecting both the operation of the power driver as well as the acoustic exposure during sonoporation treatments. Taking a more detailed approach to the transducer design may be part of some future work. Broadening the frequency response

of piezoelectric elements (*i.e.,* improving pulsed operation) has been performed both mechanically, by adding quarter-wave-length matching layers to the front-side of air-backed transducers [74], and electrically, using lumped broad-band equalizer circuits [75,76]. Additional information on broadband transducers for imaging and their design are available from [47] and [77].

5.5 Near-focus Operation

The acoustic near-field was chosen as the operating region for the sonoporation platform in order to reduce the height of the device. However, this need was based on the choice of a 20 mm diameter piezoelectric element – a choice which resulted from consultation with the manufacturer based on the acoustic requirements. It may be possible to achieve a similar treatment distance (*i.e.,* device height) with elements of half the size (10 mm in diameter). The near-far field transition distance for such an ideal device would be approximately 16.6 mm. The benefits of pursuing this design change include wider, more homogeneous exposure zones and the possibility of more devices (*i.e.,* an overall greater exposure area).

Appendix A

Modes of Operation of a Half-Bridge Class DE Switch-Mode Amplifier

A.1 Circuit Description

The Class DE amplifier described in [67] is a half-bridge topology (Fig. A.1). The two switching components are driven to saturation in an alternating fashion where the top device is switched on at $\omega t = 0$, the bottom device is switched on at $\omega t = \pi$, and each device is on no longer than half the period ($k = \frac{\Delta\omega t}{2\pi} < 0.5$). Hence, there exists a dead-time between each device switching off and the next switching on where two switch-shunt capacitors charge or discharge, both supplying the output current and shaping the voltages across the switching components. The design of the amplifier is such that the zero-voltage switching (ZVS) and zero-derivative switching (ZDS) conditions are satisfied at the time of turn-on of each switching device. The output consists of a tuned RLC network of sufficiently high quality-factor, such that the output current waveform is assumed sinusoidal. Here, the design equations are derived for the case of $k = 0.25$ (equal switching and dead-times) [67].

A.2 Assumptions

1. All switches are assumed ideal, having zero switching times, zero on-state resistance, and infinite off-state resistance.

2. The quality factor of the output RLC network Q_L is sufficiently high, such that the

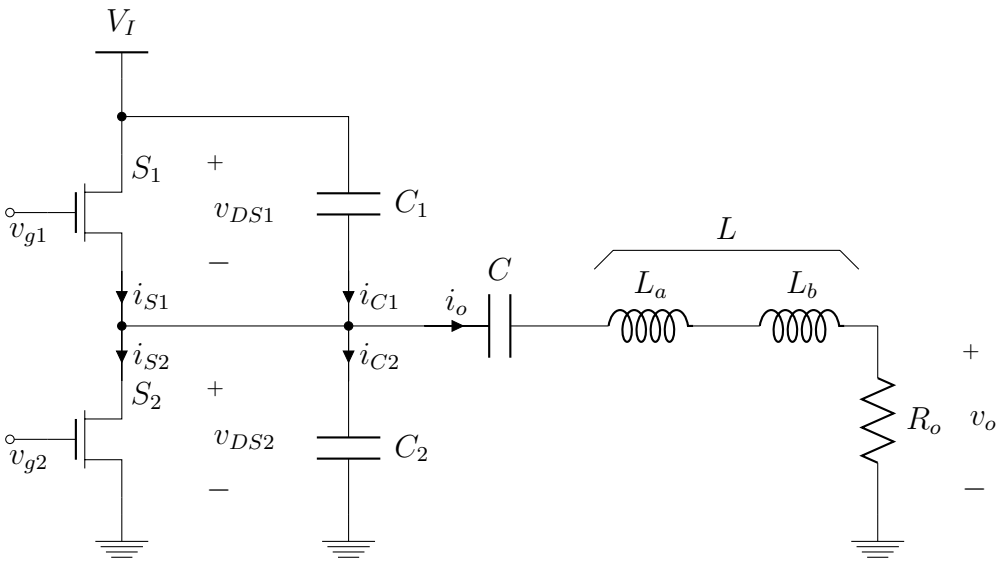

Figure A.1: Class DE power amplifier topology [67].

output current is considered sinusoidal, *i.e.*, $i_o = I_m sin(\omega t + \phi)$.

3. Each switch is on for one-quarter of the period ($k = 0.25$) with the top switching component switching on at $\omega t = 0$ and the bottom switching component switching on at $\omega t = \pi$.

A.3 Modes of Operation

The DE topology shown in Figure A.1 has four modes of operation.

Mode 1: S_1 on/S_2 off

This mode begins with S_1 switching on.

$$v_{DS1} = 0 \tag{A.1}$$

$$v_{DS2} = V_I \tag{A.2}$$

$$\frac{dv_{DS1}}{d(\omega t)} = \frac{dv_{C1}}{d(\omega t)} = 0 \tag{A.3}$$

$$\frac{dv_{DS2}}{d(\omega t)} = \frac{dv_{C2}}{d(\omega t)} = 0 \tag{A.4}$$

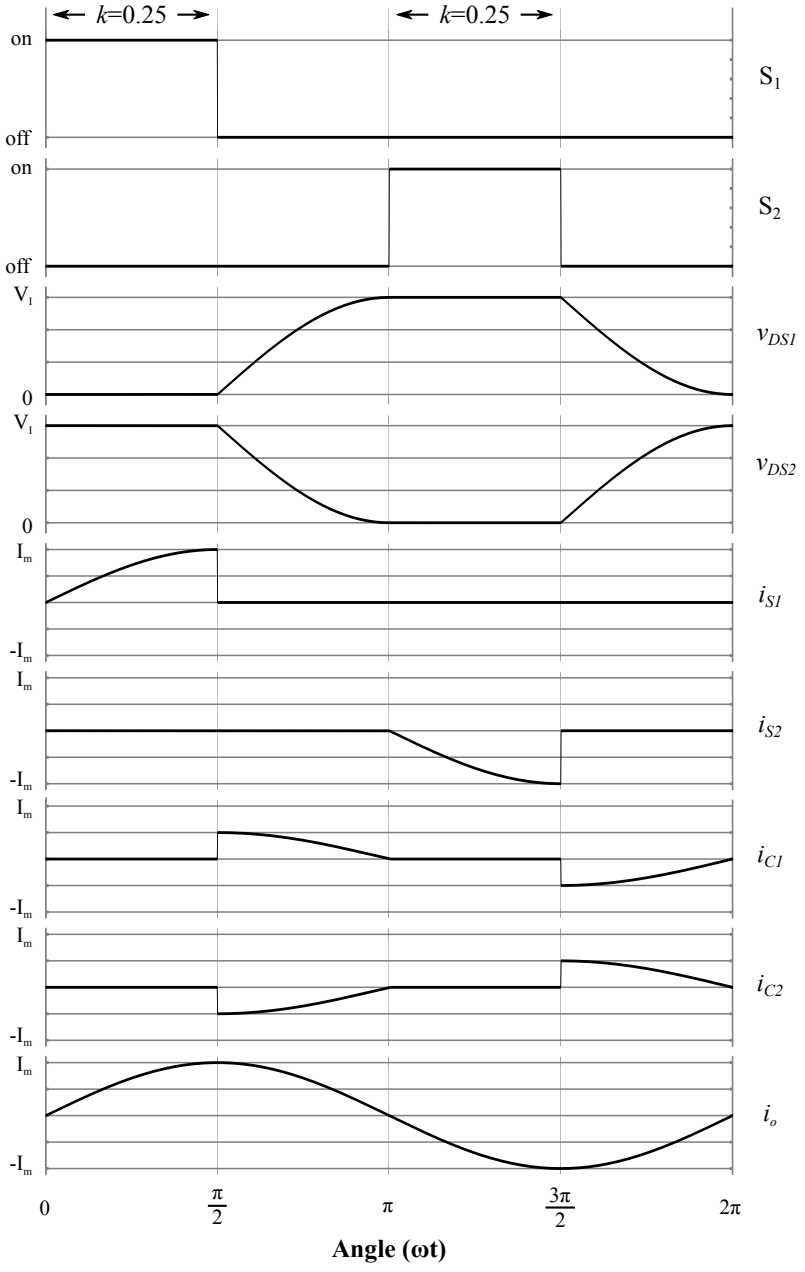

Figure A.2: The waveforms for Class DE power amplifier with duty cycle of $k = 0.25$, corresponding to voltages and currents in Fig. A.1.

The current through the capacitors becomes

$$i_{C1} = \omega C_1 \frac{dv_{C1}}{d(\omega t)} = 0 \tag{A.5}$$

$$i_{C2} = \omega C_2 \frac{dv_{C2}}{d(\omega t)} = 0 \tag{A.6}$$

Thus, the output current, $i_o = I_m \sin(\omega t + \phi)$, is carried by S_1

$$i_o = i_{C1} - i_{C2} + i_{S1} - i_{S2} \tag{A.7}$$

$$i_o = 0 - 0 + i_{S1} - 0 \tag{A.8}$$

$$i_o = i_{S1} \tag{A.9}$$

$$i_{S1} = I_m \sin(\omega t + \phi) \tag{A.10}$$

Mode 2: S_1 off/S_2 off

This mode begins with S_1 switching off:

$$v_{C1} = V_I - v_{C2} \tag{A.11}$$

$$\frac{dv_{C1}}{d(\omega t)} = -\frac{dv_{C2}}{d(\omega t)} \tag{A.12}$$

$$\frac{dv_{DS1}}{d(\omega t)} = -\frac{dv_{DS2}}{d(\omega t)} \tag{A.13}$$

Since both switching devices are off, the output current is carried by the capcitors C_1 and C_2:

$$i_o = i_{C1} - i_{C2} + i_{S1} - i_{S2} \tag{A.14}$$

$$i_o = i_{C1} - i_{C2} + 0 + 0 \tag{A.15}$$

$$i_o = i_{C1} - i_{C2} \tag{A.16}$$

$$i_o = \omega C_1 \frac{dv_{C1}}{d(\omega t)} - \omega C_2 \frac{dv_{C2}}{d(\omega t)} \tag{A.17}$$

$$i_o = \omega C_1 \left(-\frac{dv_{C2}}{d(\omega t)} \right) - \omega C_2 \frac{dv_{C2}}{d(\omega t)} \tag{A.18}$$

$$I_m \sin(\omega t + \phi) = -\omega (C_1 + C_2) \frac{dv_{C2}}{d(\omega t)} \tag{A.19}$$

$$\frac{dv_{C2}}{d(\omega t)} = \frac{dv_{DS2}}{d(\omega t)} = \frac{-I_m}{\omega (C_1 + C_2)} \sin(\omega t + \phi) \tag{A.20}$$

At the start of mode 3, S_2 will switch on. The design requires the voltage across the switch (ZVS) and its derivative (ZDS) to be zero at the moment the switch turns on ($\omega t = \pi$):

$$v_{DS2}\Big|_{\omega t=\pi} = 0 \tag{A.21}$$

and

$$\frac{dv_{DS2}}{d(\omega t)}\Big|_{\omega t=\pi} = 0 \tag{A.22}$$

Applying (A.22) (the ZDS condition) to (A.20) yields

$$\frac{-I_m}{\omega(C_1+C_2)}\sin(\omega t+\phi)\Big|_{\omega t=\pi} = 0 \tag{A.23}$$

$$\frac{-I_m}{\omega(C_1+C_2)}\sin(\pi+\phi) = 0 \tag{A.24}$$

$$\sin(\pi+\phi) = 0\ . \tag{A.25}$$

Two solutions exist: $\phi = 0$ and $\phi = \pi$. Since C_1 is charging and C_2 is discharging during this interval, the only physical result is

$$\phi = 0\ . \tag{A.26}$$

In order to apply the ZVS condition, v_{DS2} must be deterimined by integration of (A.20):

$$v_{DS2} = v_{DS2}\Big|_{\omega t=\frac{\pi}{2}} + \int_{\frac{\pi}{2}}^{\omega t}\frac{dv_{DS2}}{d(\omega t)}d(\omega t) \tag{A.27}$$

$$v_{DS2} = V_I + \int_{\frac{\pi}{2}}^{\omega t}\frac{-I_m}{\omega(C_1+C_2)}\sin(\omega t+\phi)d(\omega t) \tag{A.28}$$

$$v_{DS2} = V_I - \frac{I_m}{\omega(C_1+C_2)}\int_{\frac{\pi}{2}}^{\omega t}\sin(\omega t)d(\omega t) \tag{A.29}$$

$$v_{DS2} = V_I - \frac{I_m}{\omega(C_1+C_2)}\left[-cos(\omega t) + cos\left(\frac{\pi}{2}\right)\right] \tag{A.30}$$

$$v_{DS2} = V_I + \frac{I_m}{\omega(C_1+C_2)}\cos(\omega t) \tag{A.31}$$

Applying (A.21) (the ZVS condition) to (A.31) yields

$$V_I + \frac{I_m}{\omega(C_1 + C_2)} \cos(\pi) = 0 \tag{A.32}$$

$$V_I = \frac{I_m}{\omega(C_1 + C_2)} \ . \tag{A.33}$$

As a result, v_{DS2} simplies to

$$v_{DS2} = V_I + \frac{I_m}{\omega(C_1 + C_2)} \cos(\omega t) \tag{A.34}$$

$$v_{DS2} = V_I + V_I \cos(\omega t) \tag{A.35}$$

$$v_{DS2} = V_I[1 + \cos(\omega t)] \ . \tag{A.36}$$

Mode 3: S_1 off/S_2 on

This mode begins with S_2 switching on:

$$v_{DS1} = V_I \tag{A.37}$$

$$v_{DS2} = 0 \tag{A.38}$$

$$\frac{dv_{DS1}}{d(\omega t)} = \frac{dv_{C1}}{d(\omega t)} = 0 \tag{A.39}$$

$$\frac{dv_{DS2}}{d(\omega t)} = \frac{dv_{C2}}{d(\omega t)} = 0 \tag{A.40}$$

The output current is carried by S_2:

$$i_o = i_{C1} - i_{C2} + i_{S1} - i_{S2} \tag{A.41}$$

$$i_o = 0 - 0 + 0 - i_{S2} \tag{A.42}$$

$$i_{S2} = -i_o \tag{A.43}$$

$$i_{S2} = -I_m \sin(\omega t) \tag{A.44}$$

Mode 4: S_1 off/S_2 off

This mode begins with S_2 switching off.

$$v_{C1} = V_I - v_{C2} \tag{A.45}$$

$$\frac{dv_{C1}}{d(\omega t)} = -\frac{dv_{C2}}{d(\omega t)} \tag{A.46}$$

The output current is carried by capacitors C_1 and C_2:

$$i_o = i_{C1} - i_{C2} + i_{S1} - i_{S2} \tag{A.47}$$

$$i_o = i_{C1} - i_{C2} + 0 - 0 \tag{A.48}$$

$$i_o = i_{C1} - i_{C2} \tag{A.49}$$

$$i_o = \omega C_1 \frac{dv_{C1}}{d(\omega t)} - \omega C_2 \frac{dv_{C2}}{d(\omega t)} \tag{A.50}$$

$$i_o = \omega C_1 \frac{dv_{C1}}{d(\omega t)} - \omega C_2 \left(-\frac{dv_{C1}}{d(\omega t)} \right) \tag{A.51}$$

$$i_o = \omega C_1 \frac{dv_{C1}}{d(\omega t)} - \omega C_2 \left(-\frac{dv_{C1}}{d(\omega t)} \right) \tag{A.52}$$

$$I_m \sin(\omega t) = \omega (C_1 + C_2) \frac{dv_{C1}}{d(\omega t)} \tag{A.53}$$

$$\frac{dv_{C1}}{d(\omega t)} = \frac{I_m}{\omega (C_1 + C_2)} \sin(\omega t) \tag{A.54}$$

$$\frac{dv_{DS1}}{d(\omega t)} = \frac{I_m}{\omega (C_1 + C_2)} \sin(\omega t) \tag{A.55}$$

At the end of this interval ($\omega t = 2\pi$) the switch S_1 should turn on with the ZVS and ZDS conditions satisfied:

$$v_{DS1}\Big|_{\omega t = 2\pi} = 0 \tag{A.56}$$

and

$$\frac{dv_{DS1}}{d(\omega t)}\Big|_{\omega t = 2\pi} = 0 \tag{A.57}$$

Integrating (A.55) to get v_{DS1},

$$v_{DS1} = v_{DS1}\Big|_{\omega t=\frac{3\pi}{2}} + \int_{\frac{3\pi}{2}}^{\omega t} \frac{dv_{DS1}}{d(\omega t)} d(\omega t) \tag{A.58}$$

$$v_{DS1} = V_I + \int_{\frac{3\pi}{2}}^{\omega t} \frac{I_m}{\omega(C_1 + C_2)} \sin(\omega t) d(\omega t) \tag{A.59}$$

$$v_{DS1} = V_I + \frac{I_m}{\omega(C_1 + C_2)} \int_{\frac{\pi}{2}}^{\omega t} \sin(\omega t) d(\omega t) \tag{A.60}$$

$$v_{DS1} = V_I + \frac{I_m}{\omega(C_1 + C_2)} \left[-cos(\omega t) + \cos\left(\frac{3\pi}{2}\right) \right] \tag{A.61}$$

$$v_{DS1} = V_I - \frac{I_m}{\omega(C_1 + C_2)} \cos(\omega t) \tag{A.62}$$

and applying the ZVS condition in (A.56) to ,

$$V_I - \frac{I_m}{\omega(C_1 + C_2)} \cos(2\pi) = 0 \tag{A.63}$$

$$V_I = \frac{I_m}{\omega(C_1 + C_2)} \tag{A.64}$$

gives

$$v_{DS1} = V_I - \frac{I_m}{\omega(C_1 + C_2)} \cos(\omega t) \tag{A.65}$$

$$v_{DS1} = V_I - V_I \cos(\omega t) \tag{A.66}$$

$$v_{DS1} = V_I[1 - \cos(\omega t)] \tag{A.67}$$

and

$$v_{DS2} = V_I - v_{DS1} \tag{A.68}$$

$$v_{DS2} = V_I \cos(\omega t) \ . \tag{A.69}$$

Since the DC current through the switch shunt capacitor is zero at steady state operation, the DC supply current develops as a result of the switching components. Thus, the average (DC) input current is

$$I_I = \frac{1}{2\pi}\int_0^{2\pi} i_{S1}d(\omega t) \tag{A.70}$$

$$I_I = \frac{1}{2\pi}\int_0^{\frac{\pi}{2}} I_m \sin(\omega t) \tag{A.71}$$

$$I_I = \frac{I_m}{2\pi} \tag{A.72}$$

$$I_I = \frac{\omega(C_1 + C_2)}{2\pi} V_I \tag{A.73}$$

and the input resistance at steady state is

$$R_{I(DC)} = \frac{V_I}{I_I} \tag{A.74}$$

$$R_{I(DC)} = \frac{V_I}{\left(\frac{\omega(C_1+C_2)}{2\pi}\right) V_I} \tag{A.75}$$

$$R_{I(DC)} = \frac{2\pi}{\omega(C_1 + C_2)}\ . \tag{A.76}$$

A.4 Component Values and Stresses

Here, the amplifier will be operating above resonance (*i.e.,* inductive) at its operating frequency ω. That is, $L = L_a + L_b$ where C resonantes with L_a at ω (Fig. A.1). Additionally, it is assumed that the output network filters the harmonic components of v_{DS2}, hence, the fundamental component of v_{DS2} is

$$v_{Lb} + v_{Ro} = V_{Lbm}\cos(\omega t) + V_m \sin(\omega t) \tag{A.77}$$

for operating frequency ω. Therefore, from Fourier anaylsis,

$$V_m = \frac{1}{\pi}\int_0^{2\pi} v_{DS2}\sin(\omega t)d(\omega t) \tag{A.78}$$

$$V_m = \frac{1}{\pi}\left(\int_0^{\frac{\pi}{2}} V_I\sin(\omega t)d(\omega t) + \int_{\frac{\pi}{2}}^{\pi} V_I[cos(\omega t)+1]\sin(\omega t)d(\omega t) + \int_{\frac{3\pi}{2}}^{2\pi} V_I\cos(\omega t)\sin(\omega t)d(\omega t)\right) \tag{A.79}$$

$$V_m = \frac{V_I}{\pi}\left(-cos(\omega t)\Big|_0^{\frac{\pi}{2}} + \sin(\omega t)\Big|_{\frac{\pi}{2}}^{\pi} - \cos(\omega t)\Big|_{\frac{\pi}{2}}^{\pi} - \frac{1}{2}\cos^2(\omega t)\Big|_{\frac{3\pi}{2}}^{2\pi}\right) \tag{A.80}$$

$$V_m = \frac{V_I}{\pi} \tag{A.81}$$

and

$$V_{Lbm} = \frac{1}{\pi}\int_0^{2\pi} v_{DS2}\cos(\omega t)d(\omega t) \tag{A.82}$$

$$V_{Lbm} = \frac{1}{\pi}\left(\int_0^{\frac{\pi}{2}} V_I\cos(\omega t)d(\omega t) + \int_{\frac{\pi}{2}}^{\pi} V_I[cos(\omega t)+1]\cos(\omega t)d(\omega t) + \int_{\frac{3\pi}{2}}^{2\pi} V_I\cos^2(\omega t)d(\omega t)\right) \tag{A.83}$$

$$V_{Lbm} = \frac{V_I}{\pi}\left(\sin(\omega t)\Big|_0^{\frac{\pi}{2}} + \frac{1}{2}\left(\omega t + \sin(\omega t)cos(\omega t)\right)\Big|_{\frac{\pi}{2}}^{\pi} + \sin(\omega t)\Big|_{\frac{\pi}{2}}^{\pi} + \frac{1}{2}\left(\omega t + \sin(\omega t)cos(\omega t)\right)\Big|_{\frac{3\pi}{2}}^{2\pi}\right) \tag{A.84}$$

$$V_{Lbm} = \frac{V_I}{2} \tag{A.85}$$

The values for the resonant network can now be determined, beginning with L_b,

$$\frac{V_{Lbm}}{V_m} = \frac{\omega L_b}{R_o} = \frac{\pi}{2}\ . \tag{A.86}$$

Hence,

$$L_b = \frac{\pi}{2}\frac{R_o}{\omega}\ . \tag{A.87}$$

Consequently, the resonanting components become

$$L_a = L - L_b \tag{A.88}$$

$$L_a = \frac{Q_L R_o}{\omega} - \frac{\pi}{2}\frac{R_o}{\omega} \tag{A.89}$$

$$L_a = \left(Q_L - \frac{\pi}{2}\right)\frac{R_o}{\omega} \tag{A.90}$$

and

$$C = \frac{1}{\omega^2 L_a} \tag{A.91}$$

$$C = \frac{1}{\omega R_o (Q_L - \frac{\pi}{2})} \ . \tag{A.92}$$

From (A.81), the output power becomes

$$P_o = \frac{\left(V_m/\sqrt{2}\right)^2}{R_o} \tag{A.93}$$

$$P_o = \frac{V_I^2}{2\pi^2 R_o} \ . \tag{A.94}$$

Assuming an efficiency of $\eta = \dfrac{P_o}{P_I} = 100\%$,

$$P_o = P_I \tag{A.95}$$

$$P_o = V_I I_I \tag{A.96}$$

$$\frac{V_I^2}{2\pi^2 R_o} = \frac{\omega(C_1 + C_2)}{2\pi} V_I^2 \tag{A.97}$$

$$C_1 + C_2 = \frac{1}{\pi\omega R_o} \ . \ . \tag{A.98}$$

Letting $C_1 = C_2 = C_m$, (A.98) yields

$$C_m = \frac{1}{2\pi\omega R_o} \ . \tag{A.99}$$

A.5 Summary

The design equations for the Class DE amplifier for $k = 0.25$ are summarized in Tables A.1 (component values) and A.2 (device stresses).

Load resistance	$R_o = \frac{V_I^2}{2\pi^2 P_o}$	$(A.100)$
Shunt capacitors	$C_m = \frac{1}{2\pi\omega R_o}$	$(A.101)$
Output inductance	$L = \frac{Q_L R_o}{\omega}$	$(A.102)$
Output capacitance	$C = \frac{1}{\omega R_o (Q_L - \frac{\pi}{2})}$	$(A.103)$

Table A.1: Component value equations for a Class DE half-bridge amplifier, $k = 0.25$ [67].

Maximum drain current	$I_{DM(max)} = I_{m(max)} = \frac{V_m}{R} = \frac{V_I}{\pi R}$	$(A.104)$
Maximum drain-source voltage	$V_{DS(max)} = V_I$	$(A.105)$
Maximum voltage across series capacitor	$V_{C(max)} = \frac{I_{m(max)}}{\omega C}$	$(A.106)$
Maximum voltage across series inductor	$V_{L(max)} = \omega L I_{m(max)}$	$(A.107)$

Table A.2: Device stress equations for a Class DE half-bridge amplifier, $k = 0.25$ [67].

Bibliography

[1] J. G. Lynn, R. L. Zwemer, A. J. Chick, and A. E. Miller, "A new method for the generation and use of focused ultrasound in experimental biology," *J Gen Physiol*, vol. 26, no. 2, pp. 179–193, 1942.

[2] W. J. Fry, W. H. Mosberg, Jr., J. W. Barnard, and F. J. Fry, "Production of focal destructive lesions in the central nervous system with ultrasound.," *J. Neurosurg*, vol. 5, no. 11, pp. 471–478, 1954.

[3] K. Hynynen, W. R. Freund, H. E. Cline, A. H. Chung, R. D. Watkins, J. P. Vetro, and F. A. Jolesz, "A clinical, noninvasive, MR imaging-monitored ultrasound surgery method," *RadioGraphics*, vol. 16, no. 1, pp. 185–195, 1996.

[4] N. B. Smith, M. T. Buchanan, and K. Hynynen, "Transrectal ultrasound applicator for prostate heating monitored using MRI thermometry," *Int J Radiation Oncology Biol Phys*, vol. 43, no. 1, pp. 217–225, 1999.

[5] M. O. Köhler, C. Mougenot, B. Quesson, J. Enholm, B. Le Bail, C. Laurent, C. T. W. Moonen, and G. J. Ehnholm, "Volumetric HIFU ablation under 3D guidance of rapid MRI thermometry," *Medical Physics*, vol. 36, no. 8, pp. 3521–3535, 2009.

[6] B. E. O'Neill, H. Vo, M. Angstadt, K. P. C. Li, T. Quinn, and V. Frenkel, "Pulsed high intensity focused ultrasound mediated nanoparticle delivery: mechanisms and efficacy in murine muscle," *Ultrasound Med Biol*, vol. 35, pp. 416–24, Mar. 2009.

[7] A. Yudina and C. Moonen, "Ultrasound-induced cell permeabilisation and hyperthermia: strategies for local delivery of compounds with intracellular mode of action," *Int J Hyperther*, vol. 28, no. 4, pp. 311–9, 2012.

[8] A. Yudina, M. Lepetit-Coiffé, M. D. Smet, S. Langereis, H. Grüll, and C. Moonen, "In vivo temperature controlled ultrasound-mediated intracellular delivery of cell-impermeable compounds," *J Control Release*, vol. 161, no. 1, pp. 90–97, 2012.

[9] M. B. Yatvin, J. N. Weinstein, D. W. H., and B. R., "Design of liposomes for enhanced local release of drugs by hyperthermia," *Science*, vol. 202, no. 4374, pp. 1290–1293, 1978.

[10] M. Bikram and J. L. West, "Thermo-responsive systems for controlled drug delivery," *Expert Opin Drug Deliv*, vol. 5, no. 10, pp. 1077–1091, 2008.

[11] S. Bao, B. D. Thrall, and D. L. Miller, "Transfection of a reporter plasmid into cultured cells by sonoporation in vitro," *Ultrasound Med Biol*, vol. 23, no. 6, pp. 953–959, 1997.

[12] D. L. Miller and J. Quddus, "Sonoporation of monolayer cells by diagnostic ultrasound activation of contrast-agent gas bodies," *Ultrasound Med Biol*, vol. 26, no. 4, pp. 661–667, 2000.

[13] K. Hynynen, N. McDannold, N. Vykhodtseva, and F. A. Jolesz, "Noninvasive MR imaging-guided focal opening of the blood-brain barrier in rabbits," *Radiology*, vol. 220, no. 3, pp. 640–646, 2001.

[14] M. Kinoshita and K. Hynynen, "A novel method for the intracellular delivery of siRNA using microbubble-enhanced focused ultrasound," *Biochem Bioph Res Co*, vol. 335, no. 2, pp. 393–399, 2005.

[15] A. Rahim, S. L. Taylor, N. L. Bush, G. R. ter Haar, J. C. Bamber, and C. D. Porter, "Physical parameters affecting ultrasound/microbubble-mediated gene delivery efficiency in vitro," *Ultrasound Med Biol*, vol. 32, no. 8, pp. 1269–1279, 2006.

[16] M. Kinoshita and K. Hynynen, "Key factors that affect sonoporation efficiency in in vitro settings: The importance of standing wave in sonoporation," *Biochem Bioph Res Co*, vol. 359, no. 4, pp. 860–865, 2007.

[17] F. Yang, N. Gu, D. Chen, X. Xi, D. Zhang, Y. Li, and J. Wu, "Experimental study on cell self-sealing during sonoporation," *J Control Release*, vol. 131, no. 3, pp. 205–210, 2008.

[18] R. Karshafian, P. D. Bevan, R. Williams, S. Samac, and P. N. Burns, "Sonoporation by ultrasound-activated microbubble contrast agents: Effect of acoustic exposure parameters on cell membrane permeability and cell viability," *Ultrasound Med Biol*, vol. 35, no. 5, pp. 847–860, 2009.

[19] A. Yudina, M. Lepetit-Coiffé, and C. T. W. Moonen, "Evaluation of the temporal window for drug delivery following ultrasound-mediated membrane permeability enhancement," *Mol Imaging Biol*, vol. 13, no. 2, pp. 239–249, 2011.

[20] L. Curiel, K. Lee, S. Pichardo, and I. Zehbe, "Sonoporation of cervical carcinoma cells affected with e6-oncoprotein for the treatment of uterine cancer," *AIP Conf Proc*, vol. 1215, no. 1, pp. 119–122, 2010.

[21] M. Togtema, S. Pichardo, R. Jackson, P. F. Lambert, C. Laura, and I. Zehbe, "Sonoporation Delivery of Monoclonal Antibodies against Human Papillomavirus 16 E6

Restores p53 Expression in Transformed Cervical Keratinocytes," *PLoS ONE*, vol. 7, p. e50730, 11 2012.

[22] S. Pichardo, M. Togtema, R. Jackson, I. Zehbe, and L. Curiel, "Influence of cell line and cell cycle phase on sonoporation transfection efficiency in cervical carcinoma cells under the same physical conditions," *IEEE Trans Ultrason, Ferroelectr, Freq Control*, vol. 60, pp. 432–435, February 2013.

[23] L. Kowalczuk, M. Boudinet, M. E. Sanharawi, E. Touchard, M.-C. Naud, A. Saed, J.-C. Jeanny, F. Behar-Cohen, and P. Laugier, "In vivo gene transfer into the ocular ciliary muscle mediated by ultrasound and microbubbles," *Ultrasound Med Biol*, vol. 37, no. 11, pp. 1814–1827, 2011.

[24] S. Mehier-Humbert, T. Bettinger, F. Yan, and R. H. Guy, "Plasma membrane poration induced by ultrasound exposure: Implication for drug delivery," *J Control Release*, vol. 104, no. 1, pp. 213–222, 2005.

[25] J. L. Tlaxca, C. R. Anderson, A. L. Klibanov, B. Lowrey, J. A. Hossack, J. S. Alexander, M. B. Lawrence, and J. J. Rychak, "Analysis of in vitro transfection by sonoporation using cationic and neutral microbubbles," *Ultrasound Med Biol*, vol. 36, pp. 1907–1918, 2010.

[26] A. Delalande, S. Kotopoulis, M. Postema, P. Midoux, and C. Pichon, "Sonoporation: Mechanistic insights and ongoing challenges for gene transfer," *Gene*, vol. 525, no. 2, pp. 191–199, 2013.

[27] A. van Wamel, K. Kooiman, M. Harteveld, M. Emmer, F. J. ten Cate, M. Versluis, and N. de Jong, "Vibrating microbubbles poking individual cells: Drug transfer into cells via sonoporation," *J Control Release*, vol. 112, no. 2, pp. 149–155, 2006.

[28] A. A. Doinikov and A. Bouakaz, "Acoustic microstreaming around an encapsulated particle," *J Acoust Soc Am*, vol. 127, no. 3, pp. 1218–1227, 2010.

[29] Y. Qiu, C. Zhang, J. Tu, and D. Zhang, "Microbubble-induced sonoporation involved in ultrasound-mediated DNA transfection in vitro at low acoustic pressures," *J Biomech*, vol. 45, no. 8, pp. 1339–1345, 2012.

[30] M. Postema, A. van Wamel, C. T. Lance, and N. de Jong, "Elucidating the mechanisms behind sonoporation with adeno-associated virus-loaded microbubbles," *Ultrasound Med Biol*, vol. 30, no. 6, pp. 827–840, 2004.

[31] C. D. Ohl, M. Arora, R. Ikink, N. de Jong, M. Versluis, M. Delius, and D. Lohse, "Sonoporation from jetting cavitation bubbles," *Biophys J*, vol. 91, no. 11, pp. 4285–4295, 2006.

[32] B. D. Meijering, L. J. Juffermans, A. van Wamel, R. H. Henning, I. S. Zuhorn, M. Emmer, A. M. Versteilen, W. J. Paulus, W. H. van Gilst, K. Kooiman, N. de Jong, R. J. Musters, L. E. Deelman, and O. Kamp, "Ultrasound and microbubble-targeted delivery of macromolecules is regulated by induction of endocytosis and pore formation," *Circ Res*, vol. 104, no. 5, pp. 679–687, 2009.

[33] B. Geers, I. Lentacker, A. Alonso, N. N. Sanders, J. Demeester, S. Meairs, and S. C. De Smedt, "Elucidating the mechanisms behind sonoporation with adeno-associated virus-loaded microbubbles," *Mol Pharm*, vol. 8, no. 6, pp. 2244–2251, 2011.

[34] A. Delalande, S. Kotopoulis, T. Rovers, C. Pichon, and M. Postema, "Sonoporation at a low mechanical index," *Bubble Sci Eng Technol*, vol. 3, no. 1, pp. 3–12, 2011.

[35] D. L. Miller, S. Bao, and J. E. Morris, "Sonoporation of cultured cells in the rotating tube exposure system," *Ultrasound Med Biol*, vol. 25, pp. 143–149, 1999.

[36] D. L. Miller and C. Dou, "Induction of apoptosis in sonoporation and ultrasonic gene transfer," *Ultrasound Med Biol*, vol. 35, no. 1, pp. 144–154, 2008.

[37] H.-D. Liang, Q. L. Lu, S.-A. Xue, M. Halliwell, T. Kodama, D. O. Cosgrove, H. J. Stauss, T. A. Partridge, and M. J. Blomley, "Optimisation of ultrasound-mediated gene transfer (sonoporation) in skeletal muscle cells," *Ultrasound Med Biol*, vol. 30, no. 11, pp. 1523–1529, 2004.

[38] M. Derieppe, A. Yudina, M. Lepetit-Coiffé, B. D. de Senneville, C. Bos, and C. Moonen, "Real-time assessment of ultrasound-mediated drug delivery using fibered confocal fluorescence microscopy," *Mol Imaging Biol*, vol. 15, no. 1, pp. 3–11, 2013.

[39] M. Lepetit-Coiffé, A. Yudina, C. Poujol, P. L. Oliveira, F. Couillaud, and C. T. Moonen, "Quantitative evaluation of ultrasound-mediated cellular uptake of a fluorescent model drug," *Mol Imaging Biol*, vol. 15, no. 5, pp. 523–533, 2013.

[40] L. Van Ruijssevelt, P. Smirnov, A. Yudina, V. Bouchaud, P. Voisin, and C. Moonen, "Observations on the viability of C6-glioma cells after sonoporation with low-intensity ultrasound and microbubbles," *IEEE Trans Ultrason, Ferroelectr, Freq Control*, vol. 60, pp. –, January 2013.

[41] Y. Z. Zhao, Y. K. Luo, C. T. Lu, J. F. Xu, J. Tang, M. Zhang, Y. Zhang, and H. D. Liang, "Phospholipids-based microbubbles sonoporation pore size and reseal of cell membrane cultured in vitro," *J Drug Target*, vol. 16, no. 1, pp. 18–25, 2008.

[42] I. V. LARINA, B. M. EVERS, and R. O. ESENALIEV, "Optimal drug and gene delivery in cancer cells by ultrasound-induced cavitation," *Anticancer Research*, vol. 25, no. 1A, pp. 149–156, 2005.

[43] R. Karshafian, P. Bevan, G. Czarnota, and P. Bums, "The dependence of sonoporation on cell cycle phase: Enhanced effect during G2 and S-phase," in *IEEE Ultrasonics Symposium, 2007*, pp. 2005–2008, 2007.

[44] T. Nozaki, R. Ogawa, L. B. Feril, G. Kagiya, H. Fuse, and T. Kondo, "Enhancement of ultrasound-mediated gene transfection by membrane modification," *J Gene Med*, vol. 5, no. 12, pp. 1046–1055, 2003.

[45] M. W. Miller, D. L. Miller, and A. A. Brayman, "A review of in vitro bioeffects of inertial ultrasonic cavitation from a mechanistic perspective," *Ultrasound Med Biol*, vol. 22, no. 9, pp. 1131–1154, 1996.

[46] A. Forbrich, R. Paproski, M. Hitt, and R. Zemp, "Microbubble-enhanced ultrasound liberation of mrna biomarkers in vitro," *Ultrasound Med Biol*, vol. 39, no. 6, pp. 1087–1093, 2013.

[47] J. W. Hunt, M. Arditi, and F. S. Foster, "Ultrasound transducers for pulse-echo medical imaging," *IEEE Trans. Biomed. Eng.*, vol. BME-30, pp. 453–481, Aug 1983.

[48] H. Azhari, *Basics of Biomedical Ultrasound for Engineers*. John Wiley & Sons, Inc., 2010.

[49] "OpenSCAD (2013.02.28)." http://www.openscad.org.

[50] "ReplicatorG (0037)." http://replicat.org/.

[51] "skeinforge (50)." http://fabmetheus.crsndoo.com.

[52] P. C. L. Yip, *High-Frequency Circuit Design and Measurements*. Chapman and Hall, 1990.

[53] Precision Acoustics, *Needle Hydrophone System User Guide*, 2011.

[54] R. Ogawa, G. O. Kagiya, L. B. Feril, Jr., N. Nakaya, T. Nozaki, H. Fuse, and T. Kondo, "Ultrasound mediated intravesical transfection enhanced by treatment with lidocaine or heat," *J Urology*, vol. 172, no. 4, Part 1, pp. 1469–1473, 2004. Part 1 of 2.

[55] C. Guiot, R. Cavalli, P. Gaglioti, D. Danelon, C. Musacchio, M. Trotta, and T. Todros, "Temperature monitoring using ultrasound contrast agents: in vitro investigation on thermal stability," *Ultrasonics*, vol. 42, no. 1-9, pp. 927–930, 2004.

[56] C. Guiot, G. Pastore, M. Napoleone, P. Gabriele, M. Trotta, and R. Cavalli, "Thermal response of contrast agent microbubbles: Preliminary results from physico-chemical and US-imaging characterization," *Ultrasonics*, vol. 44, Supplement, no. 0, pp. e127–e130, 2006.

[57] H. Mulvana, E. Stride, J. V. Hajnal, and R. J. Eckersley, "Temperature dependent behavior of ultrasound contrast agents," *Ultrasound Med Biol*, vol. 36, no. 6, pp. 925–934, 2010.

[58] M. Stanley, "Pathology and epidemiology of HPV infection in females," *Gynecol Oncol*, vol. 117, no. 2, Supplement, pp. S5–S10, 2010.

[59] F. Friedl, I. Kimura, T. Osato, and Y. Ito, "Studies on a new human cell line (SiHa) derived from carcinoma of uterus. i. its establishment and morphology," *Exp Biol Med*, vol. 135, no. 2, pp. 543–545, 1970.

[60] A. Carpenter, T. Jones, M. Lamprecht, C. Clarke, I. Kang, O. Friman, D. Guertin, J. Chang, R. Lindquist, J. Moffat, P. Golland, and D. Sabatini, "CellProfiler: image analysis software for identifying and quantifying cell phenotypes," *Genome Biol*, vol. 7, no. 10, p. R100, 2006.

[61] R Core Team, *R: A Language and Environment for Statistical Computing*. R Foundation for Statistical Computing, Vienna, Austria, 2013.

[62] B. D. M. Meijering, R. H. Henning, W. H. Van Gilst, I. Gavrilovi'c, A. Van Wamel, and L. E. Deelman, "Optimization of ultrasound and microbubbles targeted gene delivery to cultured primary endothelial cells," *J Drug Target*, vol. 15, no. 10, pp. 664–671, 2007.

[63] C.-D. Ohl and B. Wolfrum, "Detachment and sonoporation of adherent HeLa-cells by shock wave-induced cavitation," *Biochim Biophys Acta*, vol. 1624, no. 1-3, pp. 131–138, 2003.

[64] W. Marczak, "Water as a standard in the measurements of speed of sound in liquids," *J Acoust Soc Am*, vol. 102, no. 5, pp. 2776–2779, 1997.

[65] M. Albulet, *RF Power Amplifiers*. Noble Publishing Corporation, 2001.

[66] L. Balogh, "Design and application guide for high speed MOSFET gate drive circuits," Proc. Power Supply Design Seminar (SEM 1400), Texas Instruments, 2001.

[67] M. K. Kazimierczuk, *RF Power Amplifiers*. John Wiley & Sons, Ltd., 2008.

[68] "IEEE standard definitions and methods of measurement for piezoelectric vibrators," *IEEE Std No.177*, pp. 1–, 1966.

[69] W. Wong, "An integrated ultrasound transducer driver for HIFU applications," Master's thesis, Lakehead University, 2013.

[70] M. S. Rachid, *Power Electronics: Circuits, Devices, and Applications*. Pearson Prentice Hall, third ed., 2003.

[71] S. Hintea and I. P. Mihu, "Class DE amplifiers and their medical applications," in *Optimization of Electrical and Electronic Equipments, 1998. OPTIM '98. Proceedings of the 6th International Conference on*, vol. 3, pp. 697–702, 1998.

[72] G. Hanington, P.-F. Chen, P. M. Asbeck, and L. E. Larson, "High-efficiency power amplifier using dynamic power-supply voltage for CDMA applications," *IEEE Trans Microw Theory Tech*, vol. 47, no. 8, pp. 1471–1476, 1999.

[73] V. Yousefzadeh, N. Wang, Z. Popovic, and D. Maksimovic, "A digitally controlled DC/DC converter for an RF power amplifier," *Power Electronics, IEEE Transactions on*, vol. 21, pp. 164–172, Jan 2006.

[74] C. Desilets, J. Fraser, and G. S. Kino, "The design of efficient broad-band piezoelectric transducers," *Sonics and Ultrasonics, IEEE Transactions on*, vol. 25, no. 3, pp. 115–125, 1978.

[75] J. Andersen and L. Wilkins, "The design of optimum lumped broadband equalizers for ultrasonic transducers," in *Ultrasonics Symposium, 1977*, pp. 422–427, 1977.

[76] L. J. Augustine and J. Andersen, "An algorithm for the design of transformerless broadband equalizers of ultrasonic transducers," *The Journal of the Acoustical Society of America*, vol. 66, no. 3, pp. 629–635, 1979.

[77] J. L. San Emeterio and A. Ramos, "Models for piezoelectric transducers used in broadband ultrasonic applications," in *Piezoelectric Transducers and Applications* (A. Vives, ed.), pp. 97–116, Springer Berlin Heidelberg, 2008.